Stony Brook University

Polymorphism, Preferred Orientation and Morphology of Propylene-Based Random Copolymer Subjected to External Force Fields

A Dissertation Presented

by

Yimin Mao

to

The Graduate School

in Partial Fulfillment of the

Requirements

for the Degree of

Doctor of Philosophy

in

Chemistry

Stony Brook University

August 2011

Stony Brook University

The Graduate School

Yimin Mao

We, the dissertation committee for the above candidate for the

Doctor of Philosophy degree, hereby recommend

acceptance of this dissertation.

Benjamin S. Hsiao—Dissertation Advisor
Professor, Chemistry Department

Stanislaus S. Wong—Chairperson of Defense
Professor, Chemistry Department

Joseph W. Lauher—Third Committee Member of Defense
Professor, Chemistry Department

Andy H. Tsou—Outside Committee Member of Defense
Section Head, "Structure and Performance of Organic Materials", Chemical Sciences, Corporate Strategic Research, ExxonMobil Research and Engineering Company, Clinton, New Jersey.

This dissertation is accepted by the Graduate School

Lawrence Martin
Dean of the Graduate School

Abstract of the Dissertation

Polymorphism, Preferred Orientation and Morphology of Propylene-Based Random Copolymer Subjected to External Force Fields

by

Yimin Mao

Doctor of Philosophy

in

Chemistry

Stony Brook University

2011

Crystallization of propylene-based random copolymers was investigated by using time-resolved wide- and small-angle X-ray scattering (WAXS/SAXS) techniques. With low content of 1-butylene as comonomer, both α- and γ-phase of polypropylene crystals co-existed in the system with the γ-phase being the dominant modification. When a step shear was applied, the *c*-axis of the α-phase oriented horizontally, while that of the γ-phase pointed to the vertical direction (i.e., the shear direction). Crystallization was greatly enhanced by the shear.

Uniaxial stretching experiments were also performed on the same sample at different temperatures. At high temperature (100 ^{o}C), the α-phase adopted a distinctive tilted 'cross-β' configuration. During stretching, the γ-phase was gradually transformed into the α-phase with parallel chain packing. Lamellar branching was also observed at this temperature, but was not

observed at lower temperatures. The stress associated with the mid-temperature (60 ^{o}C) deformation was found to be much higher than those at other temperatures, where this observation could be explained by the fragmentation of lamellar crystals as evident from the profile analysis of the WAXS data. At low temperate (e.g. 25 ^{o}C), the WAXS pattern was featured with prominent equatorial diffuse scattering due to the mesomorphic phase. The nature of the mesomorphic phase could be modeled with tiny β-phase crystals with about 50% oriented amorphous phase.

The thermal stability and reversibility of the γ-to-α phase transition were investigated by heating of the stretched sample to a temperature close to the nominal melting temperature and subsequent cooling to crystallization temperature of 100 ^{o}C, where the *in-situ* re-crystallization process was monitored. The heating process was found to remove residues of the γ-phase with tilted 'cross-β' configuration, whereby the newly grown γ-phase adopted a parallel orientation mode.

Contents

LIST OF FIGURES ..... **IX**

LIST OF TABLES ..... **XVIII**

1 BACKGROUND: POLYMER CRYSTALLIZATION **1**

1.1 Hierarchical structures **1**

1.1.1 Local structure: chain folding 1

1.1.2 Spherulite 2

1.1.3 Shish-kebab 3

1.1.4 Cylindrite/transcrystalline 4

1.2 Nucleation and growth **5**

1.3 Crystallization of random copolymer **6**

1.4 Model systems **8**

1.4.1 Propylene-based random copolymer 8

1.4.2 Material used in this thesis 10

2 2D WAXS/SAXS PATTERN SIMULATION **12**

2.1 General theory: the notations **12**

2.2 Calculating fiber diffraction pattern **15**

2.3 WAXS condition: the sharp peak approximation **17**

2.4 A more general condition: an example for SAXS data analysis **19**

2.5 Parallel orientation, perpendicular orientation and oblique orientation **22**

2.6 Examination of transformation kernel (ODF) **23**

2.6.1 Onsager distribution 23

2.6.2 Poisson kernel 24

2.6.3 Maier-Saupe orientation distribution 25

2.6.4 $|\cos\beta|^p$ and $|\sin\beta|^p$ orientation distribution 26

2.7 Treating the oblique orientation 26

2.8 Experimental considerations 28

2.8.1 Experimental set-up 28

2.8.2 Testing the fiber symmetry approximation 29

2.9 Summary 31

3 QUIESCENT CRYSTALLIZATION 32

3.1 Introduction 32

3.2 Materials and experimental protocols 34

3.3 Results and Discussion 35

3.3.1 A general description of crystallization process 35

3.3.2 Comparative study of crystallization at high- and low-temperature 37

3.4 Summary 47

4 SHEAR-INDUCED CRYSTALLIZATION 49

4.1 Introduction 49

4.2 Practical considerations for 2D WAXS whole-pattern analysis 51

4.2.1 Calculation details 51

4.2.2 Goodness-of-fit 52

4.3 Experimental 53

4.3.1 Materials and sample preparation 53

4.3.2 Shear-induced crystallization experiment 53

4.4 Polymorphism and orientation modes 55

4.5 Structure development during crystallization 61

4.6 Summary 66

5 CRYSTALLIZATION DURING UNIAXIAL STRETCHING 68

5.1 Introduction 68

5.2 Experimental 70

5.2.1 The stretching instrument 70

5.2.2 Materials and experimental procedure 71

5.3 Polymorphism and preferred orientation 72

5.3.1 A preliminary analysis 72

5.3.2 Considering the orientation mode 73

5.4 γ-to-α transition 81

5.5 Morphology 85

5.6 The structure-property relationship 92

5.7 Summary 94

6 MELTING AND RECRYSTALLIZATION 96

6.1 Experimental procedure 96

6.1.1 Melting experiment 96

6.1.2 Melting and recrystallization 96

6.2 Structure development during melting 97

6.3 Testing the memory effect 105

6.4 Summary 115

7 STRETCHING-INDUCED CRYSTALLIZATION: INFLUENCE OF TEMPERATURE 117

7.1 Stretching at the mid-temperature (60 ^{o}C) 117

7.2 Stretching at room temperature 125

7.3 The structure-property relationship 129

7.4 Summary 131

8 FINAL REMARKS 133

8.1 Polymorphism and preferred orientation 133

8.2 Transitions between different phases 136

8.3 Morphology 138

REFERENCE 141

List of Figures

Figure 1-1. A carton illustration of the shish-kebab structure consisting of a central shish and laterally grown kebab.

Figure 1-2. Free energy change during crystallization process.

Figure 1-3. Chemical structure of isotactic polypropylene **(a)**; syndiotactic polypropylene **(b)**; and atactic polypropylene **(c)**.

Figure 2-1. Demonstration of Bragg's law using 2D lattice **(a)**; and Ewald construction **(b)**. Detailed explanation can be found in the context.

Figure2-2. Spherical trigonometric relationship between original coordinate system (without considering orientation) and the new coordinate system for fiber-averaged intensity calculation.

Figure 2-3. Cartoon illustration of a two-phase stack **(a)**; its density profile in the direction perpendicular to the layers **(b)**; and the corresponding intensity distribution in the reciprocal space**(c)**.

Figure 2-4. Illustration of three orientation modes, defined by a fiber axis (FA) and a principle axis of rotation (PA). **(a)** Parallel orientation; **(b)** perpendicular orientation; and **(c)** oblique orientation.

Figure 2-5. Onsager distribution at different p values (distribution width).

Figure 2-6. Poisson Kernel at different p values. Both profiles with positive **(a)** and negative p **(b)** are shown.

Figure 2-7. Four-point SAXS pattern simulated using ODF defined in **Eq.(2.25) (a)**; and corresponding real space structure showing oblique orientation **(b)**.

Figure 2-8. Demonstration of testing fiber symmetry by shooting X-ray from three perpendicular directions. In practice, X-ray beam direction is fixed, and sample can be oriented.

Figure 2-9. 1D scattering profiles obtained from two perpendicular directions around the fiber axis. Intensities are scaled with consideration of sample thickness difference.

Figure 3-1. Cartoon illustration of a unit cell of α -form crystal of iPP homopolymer.

Figure 3-2. Cartoon illustration of a unit cell of γ -form crystal of iPP homopolymer.

Figure 3-3. Cartoon illustration of a unit cell of β -form crystal of iPP homopolymer.

Figure 3-4. Final integrated WAXS profiles of P-H copolymer fully melt crystallized at 100 ^{o}C, 80 ^{o}C, 60 ^{o}C and 40 ^{o}C.

Figure 3-5. (a) Crystallinity versus time plots of samples crystallized at 100 ^{o}C, 80 ^{o}C, 60 ^{o}C and 40 ^{o}C. **(b)** Induction time and crystallization half time obtained from each curve in **(a)** at different temperatures.

Figure 3-6. Evolutions of SAXS profiles for samples crystallized at **(a)** 100 ^{o}C and **(b)** 40 ^{o}C

Figure 3-7. Scattering invariant (left) and relative crystallinity index (right) versus time plot when sample was met crystallized at 100 ^{o}C. The two insets exhibit SAXS and WAXS profiles at 240s, which is in the end of the induction period.

Figure 3-8. Time-resolved SAXS profiles during crystallization at 100 ^{o}C **(a)** during the induction period; **(b)** after the induction period.

Figure 3-9. Change of peak intensity as a function of time during the early stage of crystallization at 100 ^{o}C.

Figure 3-10. Scattering invariant (left) and relative crystallinity index (right) versus time plot when sample was crystallized at 40 ^{o}C. The two insets exhibit SAXS and WAXS profiles at the very beginning of the crystallization process.

Figure 3-11. Guinier plots obtained from SAXS profiles of sample crystallized at 40 ^{o}C.

Figure 3-12. Radius of gyration (obtained from Guinier's plot) change as a function of time (crystallization temperature was 40 ^{o}C).

Figure 3-13. The crystallinity change during heating (at a heating rate of 4 ^{o}C/min) of fully crystallized samples at 100 ^{o}C (□) and at 40 ^{o}C (○).

Figure 4-1. Powder diffraction pattern of P-B random copolymer crystallizaed at 100 ^{o}C **(a)**; Fiber diffraction pattern of the sample sample crystallized at 100 ^{o}C after a step-shear with the shear rate being 100 s^{-1}, for 3 s **(b)**; and calculated powder diffraction scattering profiles of α-and γ-form crystals.

Figure 4-2. Examples of experimental (dot) and simulated intensity (mesh) of the diffraction arcs peaked at s=0.156 Å^{-1}**(a)** and at s=0.184 Å^{-1} **(b)** of P-B random copolymer. The two arcs are corresponding to $(111)_{\gamma}$ **(a)** and a superposition of $(040)_{\alpha}$ and $(008)_{\gamma}$ **(b)**. The detail of polymorphism is discussed in the context. Residual was defined as $(X_{\exp} - X_{\sin})/\sigma$, with $X_{\exp}$ and $X_{\sin}$ being the intensities from the experimental data and simulation, respectively, and σ being the standard deviation obtained from the Poisson distribution according to photon counting statistics.

Figure 4.3. Schematic of parallel plate shear mechanism **(a)**; and pictorial illustration of the definition of shear flow **(b)**.

Figure 4-4. Schematic of the experimental protocol.

Figure 4-5. Orientation modes and their corresponding fiber diffraction patterns of γ-phase iPP. **(a)-(c)** represent diagonal orientation, perpendicular orientation and cross-β configuration, respectively. Detailed description can be found in the context.

Figure 4-6. 2D WAXS patterns of experimental data (upper-left and lower-right corners), simulated γ-form (upper-right corner) and simulated α-form (lower-left corner) crystals. The experimental pattern was gathered 960 s after the step-shear when the crystallization process was complete. The flow direction was vertical; the fiber directions of γ-phase and α-phase were set to be horizontal and vertical, respectively. Cartoon illustrations of orientation of γ- and α-phase are shown on the right.

Figure 4-7. 1D integrated intensity profile from experimental data (cross point) and simulation (dashed line), where 20% of α-phase was added in the simulation. Calculated reflection peaks from the γ-phase iPP is shown below the overall profile.

Figure 4-8. Polar intensity scan of reflections from (111) plane of γ-phase (close to vertical direction) and (110) plane of α-phase (in horizontal direction).

Figure 4-9. Crystallinity change as a function of time. Contributions from both oriented and unoriented crystals are shown. Result from quiescent crystallization is also shown for comparison purpose.

Figure 4-10. Change of deviation of atomic group from their ideal crystallographic positions, ΔX, as a function of crystallization time. In-set shows the deviations in the *ab*-plane (ΔX_{12}) and that along the *c*-axis (ΔX_3).

Figure 4-11. Ratio of crystallinity contributed by defect and overall crystallinity change as a function of time. In-set shows crystallization curves using crystallinity calculated with and without considering influence of disorder.

Figure 4-12. Change of crystal dimension of γ-phase along *c*-axis, derived from reciprocal integral peak width of the (008) peak.

Figure 4-13. Change of $\langle P_2 \rangle$ as a function of time. In-set shows polar scans of intensity peaked at s = 0.184 Å^{-1} (i.e., the (008) plane for γ-phase and (040) plane for α-phase) from experimental data gathered at 90 s and 420 *s*, respectively.

Figure 5-1. Stress-strain curve of P-B co-polymer stretched at 100 ^{o}C.

Figure 5-2. Schematic of the stretching machine and the geometry of the time-resolved scattering experiment.

Figure 5-3. Schematic of the experimental protocol.

Figure 5-4. Fiber diffraction pattern of P-B copolymer stretched under 100 ^{o}C at strain = 0.5. All possible (*hkl*)s of α - and γ -phase are indexed for main diffraction arcs.

Figure 5-5. Simulated fiber diffraction patterns of the α -phase with the *c*-axis orientation **(a)**; daughter lamellae of the α -phase **(b)**; γ -phase diagonal orientation **(c)** and γ -phase with cross-β configuration **(d).** Model of unit cells are shown beside patterns. The fiber axis is vertical.

Figure 5-6. Two possible schemes of tilting of γ -phase unit cell. **(a)** parallel orientation; **(b)** oblique orientation. Details can be found in chapter 2.

Figure 5-7. Illustration of two crystal modifications of iPP and their possible orientation modes occurred during stretching experiment at 100 ^{o}C.

Figure 5-8. Typical WAXS patterns at low strain (0.5) and high strain (2.2). The upper-left and lower-right quarters are experimental data; upper-right and lower-left quarters are computed ones. The polymorphs used for diffraction pattern computation are annotated; their orientation modes are discussed in the context.

Figure 5-9. Selected profiles of intensity distribution over polar angle ϕ (**a, b**). Profiles on the left are corresponding to intensity within regions between dashed lines in diffraction patterns. A comparison of 1D scattering profile is shown in (**c**). P-B copolymer was stretched under 100 ^{o}C at strain = 0.5. The content of α -phase equals 60%.

Figure 5-10. A typical four-point SAXS pattern at strain = 0.5 **(a)**; Change of tilting angle as obtained from both SAXS and WAXS data as a function of strain **(b)**; A schematic of arrangement of γ -phase unit cell within a lamellar crystal **(c)**.

Figure 5-11. Crystallinity change during stretching process. In-set shows change of the portion due to disorder effect.

Figure 5-12. Change of crystallinity contributed by γ - and α -phase, respectively. In-set shows the relative fraction of α -phase in crystalline part. It equals 1 if crystalline is completely composed of α -phase.

Figure 5-13. Change of Hermans' orientation function $\langle P_2 \rangle$ **(a)** and unoriented portion P_0 **(b)** of γ - and α -phase during stretching. In-set in **(a)** is the same plot of apparent degree of orientation $\langle P_2 \rangle_a$ which is defined in the context.

Figure 5-14. WAXS (top row) and SAXS (bottom row) patterns of P-B co-polymer stretched at different strain. Each WAXS pattern shown in the top row is composed of four quarter sections of experimental and simulated patterns, marked with '**E**' and '**S**', respectively in corners.

Figure 5-15. 1D SAXS profiles of P-B copolymer being stretched at 100 ^{o}C, at different strain **(a)** and the change of long period derived from **(a)** as a function of strain **(b)**. The 1D profiles are integrated from -20 ^{o} to 20 ^{o}, close to the meridian.

Figure 5-16. 1D SAXS profiles of P-B copolymer being stretched at 100 ^{o}C, at different strain **(a)** and the change of long period derived from **(a)** as a function of strain **(b)**. The 1D profiles are integrated from -20 ^{o} to 20 ^{o}, close to the meridian.

Figure 5-17. An example of polar distributions of intensity at three different *s* positions and corresponding fitting curves obtained using Legendre expansion approach. The strain is equal to 1.0.

Figure 5-18. Lamellar lateral width change as a function of strain. Hollow circles represent values derived from polar angle distribution of SAXS intensity, as described in the context. The dashed line indicates the estimated value obtained through WAXS line profile analysis.

Figure 5-19. The change of Hermans' orientation function as a function of strain. Both values obtained from SAXS and WAXS methods are exhibited.

Figure 5-20. An illustration of stretching-induced SAXS pattern **(a)** and possible structures corresponding to it **(b, c)**. Meridian intensity is possible to be a superposition of split points in **(a)**. Each lamella is composed of several small block crystals, as shown in **(b)** and **(c)**. Intra-lamellar slip is also demonstrated in **(c)**.

Figure 5-21. Change of dimension of *c*-axis of γ -phase crystal unit cell during stretching.

Figure 6-1. A schematic of procedures of relaxation-recrystallization experiment.

Figure 6-2. Selected WAXS and SAXS patterns at different temperatures during heating.

Figure 6-3. Change of crystallinity (calculated from WAXS data) **(a)** and scattering invariant **(b)** as a function of temperature during heating. Plot **(b)** shows invariant integrated within regions of the meridian point (Q_b) and the streak that is slightly tilted from the equator (Q_s).

Figure 6-4. An example of fitting the tilted equatorial streak profile using 2D hard-disk model.

Figure 6-5. Hermans' orientation function (derived from WAXS data) change as a function of temperature during heating. The in-set shows orientation distributions function in real space at three typical temperatures.

Figure 6-6. Change of lamellar lateral width and Hermans' orientation as a function of time during heating. Lateral width and Hermans' orientation function shown are derived from polar distribution of intensity in SAXS data.

Figure 6-7. WAXS patterns of pre-oriented P-B copolymer melted at different temperatures (the first row) and crystallized at 100 ^{o}C for 20 *min* after cooled down from higher temperatures (the second row). Patterns in the second rows are a recombination of experimental and simulated data (see similar figures in previous chapters for detail).

Figure 6-8. Polar scan of (117) arc in the WAXS pattern crystallized from the sample melted at 128 ^{o}C.

Figure 6-9. Crystallinity change as a function of time during the crystallization of P-B at 100 ^{o}C, after being melted at different temperatures (128 ^{o}C, 130 ^{o}C and 132 ^{o}C). Data from quiescent crystallization is also shown for comparison purpose.

Figure 6-10. Relative fraction of the α-phase in P-B copolymer crystalline after melting at different temperatures and then crystallized at 100 oC **(a)**; Corresponding 1D diffraction profiles are shown in **(b)**.

Figure 6-11. 1D SAXS profiles of P-B copolymer melted at different temperatures and then crystallized 100 ^{o}C for 20 *min*. The in-set shows the 132 ^{o}C curve, in a logarithmic scale. Corresponding SAXS patterns are shown on the top.

Figure 6-12. SAXS(top) and WAXS(bottom) patterns of P-B copolymer melted at 122 ^{o}C and 130 ^{o}C and then crystallized at 100 ^{o}C for 20 *min*.

Figure 6-13. ϕ-dependence of SAXS **(a)** and WAXS **(b)** intensity obtained from patterns shown in **Figure 16-12**. Detailed description can be found in the context.

Figure 6-14. Final scattering patterns of P-B copolymer stretched at 60 ^{o}C with strain =3.71 **(a)** and **(d)**; Scattering patterns of the pre-oriented sample (after being stretched to strain =3.71 at 60 ^{o}C) after melted at 122 ^{o}C and then crystallized at 100 ^{o}C for 20 min **(b)** and **(e)**; and the patterns of the same sample after melted at 130 ^{o}C **(c)** and **(f)**.

Figure 7-1. Simulated and experimental diffraction patterns at low and high strains (strain=0.5 and 2.5, respectively), at 60 ^{o}C and 100 ^{o}C. In each image, upper left and lower right quarters are experimental results, denoted as E; upper right and lower left quarters are simulated patterns, denoted as S. Main Miller indices are annotated.

Figure 7-2. Change of crystallinity during stretching at 60 ^{o}C and 100 ^{o}C.

Figure 7-3. Change of α-phase content as a function of strain during stretching at 60 ^{o}C and 100 ^{o}C.

Figure 7-4. Change of Hermans' orientation function during stretching at 60 ^{o}C and 100 ^{o}C.

Figure 7-5. Selected SAXS patterns in the stretching process at 60 ^{o}C and 100 ^{o}C.

Figure 7-6. Change of long period as obtained from 1D SAXS curve as a function of strain at 60 ^{o}C and 100 ^{o}C.

Figure 7-7. Illustration of size and orientation effects on the intensity distribution in SAXS pattern **(a)**, half of SAXS pattern at 60 ^{o}C (strain = 2.2) showing meridian intensity is restricted

between two horizontal dashed lines **(b)**, and a fitting of s_{12}-dependence of intensity (dots) with Lorentzian function (solid line) **(c)**.

Figure 7-8. Change of lateral size of lamellae as obtained from WAXS and SAXS data as a function of strain at 60 ^{o}C **(a)** and 100 ^{o}C **(b)**.

Figure 7-9. Selected WAXS patterns in the early stage of stretching at room temperature. The arrows are pointed to the position where s = 0.167 Å^{-1}.

Figure 7-10. Calculated powder diffraction profiles of α - and β -phases.

Figure 7-11. Simulated and experimental diffraction pattern of P-B copolymer stretched room temperature, at strain=0.5 and 2.4. In each image, upper left and lower right quarters represent experimental results; upper right and lower left quarters are from simulation result.

Figure 7-12. 1D SAXS profiles of P-B copolymer stretched at room temperature, at low (strain=0.3) and high (strain=3.0) strains. The curves are integrated from meridian region, corresponding 2D SAXS patterns are shown in the in-set.

Figure 7-13. A carton illustration of mesomorphic phase which is composed of oriented amorphous phase and small β -phase crystal blocks.

Figure 7-14. Engineering stress-strain curves of P-B copolymer stretched at three temperatures: 25 ^{o}C, 60 ^{o}C and 100 ^{o}C.

List of Tables

Table 1-1. Formulas of triads characterizing random copolymer sequence.

Table 1-2. Triads of P-H and P-B random copolymer used in this thesis.

Table 2-1. Comparison of two systems of normalization in fiber pattern simulation.

Table 8-1. A summary of polymorphism and preferred orientation of samples tested in this thesis.

1 Background: Polymer Crystallization

From the viewpoint based on crystallography, there is no difference between crystal grown from small molecules and that from polymers, as the crystal is essentially defined by two elements: motif and lattice. Therefore, in principle, common techniques for crystal structure determination, such as diffraction, cannot distinguish whether a crystal is composed of atoms, small molecules or polymers, because diffraction technique can only probe the repeating 'atomic groups', according to given symmetry rule, in 3D space. However, since polymers are chain-like large molecules made up of monomers connected by covalent bonds, they do possess substantial characters in crystalline structure and in the crystallization process. For example, polymers rarely fully crystallize because of polydispersity, chain defect and crystallization kinetics and so on; and hence the term 'semi-crystalline' is used to refer the state of crystalline blocks embedded in an amorphous matrix. Also, disorder effect plays an important role in polymer crystallization, which will be discussed in detail in relevant parts of the context.

Due to the long-chain nature, two questions are of fundamental importance in this subject, i.e., **1)** how do polymer chains first arrange themselves into a unit cell and then form supramolecular structure in a large length scale; and **2)** how can chain orientation and relaxation influence the crystallization process when a polymer system is subjected to external force fields, be it weak shear flow or strong tensile force.

1.1 Hierarchical structures

1.1.1 Local structure: chain folding

The concept of chain folding forms the corner stone of polymer crystalline structure. This idea can be dated back to the 1930s[1], but was unambiguously determined in 1957 by A. Keller[2]. Single crystals of polyethylene (PE) were grown from dilute xylene solution. Based on the thickness of the crystal as obtained from transmission electron microscopy (TEM) technique, folded chain arrangement in which polymer chains fold back and forth to fit into thin layer was verified.[3] The thickness of a polymer single crystal ranges from 50 *nm* to 100 *nm*, which is

typically a length that is 1/10 of a polymer chain. Indirect evidence can also be found from small-angle X-ray scattering (SAXS) measurement from which integer and non-integer chain folding can even be derived.[4, 5]

The above adjacent folded chain picture describes chain arrangement in a single crystal grown from dilute solution where polymer chains are less entangled and have more degree of freedom. Switchboard model renders a more realistic description for morphology of crystalline grown from polymer melt. The high viscosity and large degree of entanglement determine the slow dynamics of polymer chains. Thus, instead of adjacent entry to a crystalline layer immediate to its neighbor stem, a polymer chain may reenter the layer after a big loop, or, it may span more than one layer. This model is supported by results from neutron scattering experiments and theoretical calculations.[6] Regardless of details of chain configuration, lamellar structure is an important building block for large-scale crystalline textures such as spherulite, which will be discussed below.

1.1.2 Spherulite

Spherulite is a prevalent morphology of polycrystalline grown from polymer melt.[7, 8] It is an aggregate of radially grown lamellar crystals with chain direction being in perpendicular to the radial axis.[9] Several fine details about inner arrangement of lamellae are outlined as follows. First, a spherulite can be categorized mainly into two classes based on its birefringence which is defined by the refractive index difference between radial and tangential directions, i.e., $\Delta n = n_r - n_t$, with n_r and n_t being the refractive index in the radial and tangential direction, respectively. Negative spherulites ($n_r < n_t$) are more common since polymer chains are in perpendicular to the radial axis.[10] Positive spherulites have also been observed, which is attributed to the lamellar branching effect.[10-13] Under certain circumstances spherulites with mixed optical properties can also be formed.[12, 14] Optical sign of a spherulite can be judged by polarized optical microscopy (POM)[7, 10] or small-angle light scattering (SALS) techniques.[15] Second, lamellae are able to twist in a cooperative way so that ring-banded spherulite can be formed. Ring-banded spherulites can be directly visualized through TEM[7] or indirectly through fiber diffraction pattern[16] following perpendicular orientation mode which will be discussed in

detail in the latter context. The periodicity of ring-banding can be derived from the interference maxima in SALS experiment.[17, 18]

1.1.3 Shish-kebab

Shish-kebab is a unique kind of crystalline structure composed of a central thread-like fibril (shish) and sets of folded-chain lamellae (kebab) periodically grown along shishes. It was first observed in polyethylene-xylene solution under Couette flow by Pennings et.al.[19, 20] Although the formalism of this structure is still under controversy, it can be generally depicted as follows (see **Figure 1-1**). Part of chains get stretched and aligned along the flow direction, forming central fibrous bundles that serve as nuclei; segments in the surrounding chains absorb on bundles' surface to form crystals that grow epitaxially and develop into lamellae periodically distributed along shishes. This idea was further extended to polymer melts from which interlocked shish-kebab texture conferring high modulus to materials was produced.[21] Hsiao et.al. [22] systematically investigated shear-induced structures by combining various techniques such as SAXS, WAXS and TEM, their experiments provided detail information of multi-shish and diffusion-controlled growth mode of kebabs. Shish-kebab is of great importance in shear- or stretching-induced crystalline morphology, although spatial arrangement detail of molecules may vary with the experimental condition. We will frequently use this concept in relevant places in the following chapters.

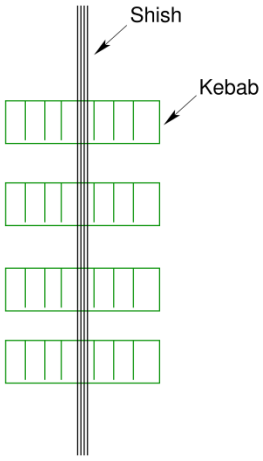

Figure 1-1. A carton illustration of the shish-kebab structure consisting of a central shish and laterally grown kebab.

1.1.4 Cylindrite/transcrystalline

In weak flow, a different kind of crystalline structure called cylindrite, first discovered by Binsbergen, often forms.[23] A small deformation of system can cause the formation of row-nuclei along the flow direction. The preexisting row-nuclei will induce secondary nucleation on its surface. Polymer crystalline structures can then further grow in a style similar to the growth of spherulite under quiescent crystallization condition. Because these structures grow spontaneously from different nucleation sites along a row-nucleus, geometry restriction will play a very important role in the morphology development. This confinement restricts the orientation of lamellae, resulting in a lateral growth of the crystal with respect to the row-like nuclei. The final morphology hence has a cylindrical shape[24, 25] (spherulite-like round shape can hardly be achieved under this condition).

A common conceptual confusion of shish-kebab and cylindrite structure must be clarified here. Shish-kebab is different from cylindrite in two aspects. First of all, shish-kebab is basically a micro-scale crystalline structure; only size in one dimension (along shish direction) may be in micrometer scale, the diameter of a kebab is usually of tens of nanometer. While cylindrite is a macro-scale crystalline structure whose size is in the order of micrometers in all dimensions, it can be easily observed with an optical microscope. The formation mechanism indicates that cylindrite is analogous to transcrystalline[26-32] (formed by epitaxial growth of polymer crystals on foreign fiber-like nucleation sites). The growth mode of 'transcrystalline' resembles that of spherulite, as shown by both morphological details of lamellae (lamellae were branched and twisted)[30, 33] and crystallization kinetics[34]. In this sense, the character which makes cylindrites differ from spherulites lies mainly in that lamellae in cylindrites only grow roughly normal to row-nuclei, not in all directions. If this spatial restriction does not exist, one may expect to see crystallites of round shape. It can be evidenced that spherulites dominate in locations far away from row-like nuclei.[24, 25] By contrast, for shish-kebab, kebabs are sets of thin lamellae located periodically along a shish; it cannot grow into large size or micrometer scale. One has sufficient reason to conjecture that shish-kebab and cylindrite have profoundly different origin. The former is a unique structure evolving from initial state far from equilibrium melt state, while the later shows notable signature of quiescent crystallization.

1.2 Nucleation and growth

When a system is quenched to a crystallization temperature, crystallization which is an entropy decrease process can take place spontaneously in compensation of more enthalpy decrease.[35] The free energy profile during the crystal growth is shown in **Figure 1-2**. The bulk free energy decreases in proportion to the volume, namely, $G_0 \propto -r^3$, with r being the dimension of a crystal (assume to be spherical), which favors crystallization. However, crystallization means the establishment of new interface, and the surface energy increases with the area, namely, $\gamma \propto r^2$ where γ represents the surface free energy. The net outcome of these two opposite factors results in a free energy maximum in the real free energy profile. In order to form stable crystals, system must experience a free energy increase process to surpass G^*, the critical free energy. The size r^* corresponding to this energy maximum is called critical size. Once nuclei exceed the critical size, crystallization can proceed with a much faster speed.[35-37]

The free energy increase process in the very initial stage of crystallization can be accomplished via nucleation whose speed is determined by temperature and purity of the system. By introducing foreign surfaces, the energy barrier can be greatly lowered, which will cause an acceleration of crystallization. This formalism is general for crystallization of both small molecules and polymers.

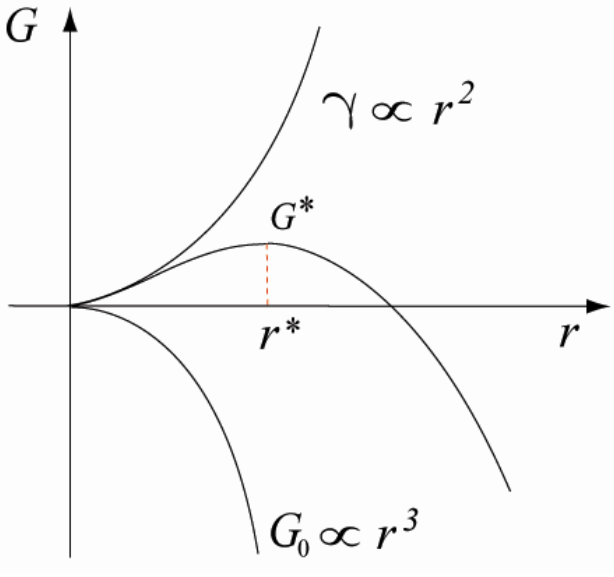

Figure 1-2. Free energy change during crystallization process.[36]

So far the Lauritzen–Hoffman (LH) kinetic theory confers the most successful description on the crystallization growth.[9, 36, 38] LH theory considers both nucleation and growth of crystal as controlled by local chain diffusion. The crystallization rate has a general form of

$$G = G_0 \exp\left[-\frac{U^*}{k(T-T_0)}\right]\exp\left(-\frac{K_g}{T\Delta T}\right) \quad \textbf{(1.1)}$$

where G is the crystallization growth rate; G_0 is a prefactor; U^* describes the local activation energy for chain diffusion and; K_g is the nucleation constant. k is the Boltzman constant and T_0 is the temperature that defines the lowest temperature where chain diffusion becomes inactive. U^* and K_g are both positive. Parameters G_0 and K_g vary with crystallization regimes of which the details can be found elsewhere.[9] **Eq.(1.1)** nicely predicts the nonmonotonic change of crystallization with temperature by introducing two exponential terms, corresponding to chain diffusion and nucleation, respectively, showing opposite trends when changing with temperature. Low temperature crystallization is more diffusion/crystal growth controlled, while high temperature one is nucleation-limited. Consequently, a maximum crystallization rate can be found between two extreme temperatures, when the supercooling is appropriate. An example of temperature dependence of crystallization rate (of isotactic polystyrene) can be found in the reference.[36] The same phenomenon can also be found in many other materials.[39]

LH theory describes crystallization under quiescent condition. However, it gives insights as to how external force fields can influence the crystallization process, as well as the morphology. From the molecular perspective, **Eq.(1.1)** is closely related to local dynamics of polymer chains, namely, extraction from surrounding melt, diffusion to crystal facet and attachment of stems onto the surface. External force is able to enhance crystallization, since it can facilitate all these three process. We will tackle on this topic in relevant places in the following chapters.[9, 36, 40-42]

1.3 Crystallization of random copolymer

Random copolymer is synthesized via copolymerization of two or more monomers of different chemical compositions, where a statistically distributed structure along the chain

backbone is obtained. If there are repulsive interactions among different species of the segments (this can be quantified using Flory's interaction parameter, χ), hierarchical textures can be formed through liquid-liquid (L-L) phase separation taking place at different length scale.[43-46] Thus, one can control the morphology of the random copolymer by adjusting the composition parameters such as the comonomer ratio and sequence distribution.[44, 47, 48] Random copolymer is able to crystallize if it contains considerable amount of crystallizable comonomer, but the crystalline's morphology, thermodynamic property, and crystallographic polymorphism differ from those of the homopolymer counterpart, and the differences are dependent on the type of comonomer, its topological property, and its statistical distribution along the chain backbone.

According to Flory,[49] the thermodynamic property of random copolymer crystalline is essentially controlled by a single parameter, the fraction of crystallizable component, as shown in **Eq.(1.2)**

$$T_m^c = T_m^0 + \frac{R}{\Delta H_u} \ln p \qquad \textbf{(1.2)}$$

where T_m^c and T_m^0 are equilibrium melting temperature of random copolymer and homopolymer, respectively. R is the gas constant; ΔH_u is the heat of fusion per mole of repeat units (crystallographic motif, e.g., C_2H_4 for polyethylene); p is the fraction of crystallizable component. As p goes from 0 to 1, with the value 1 representing homopolymer, the second term in **Eq(1.2)** is negative, thereby T_m^c is always smaller than T_m^0. Also, Flory's theory predicts that the size distribution of random copolymer crystals is broader as compared with that of homopolymer. These facts can be demonstrated by the examining the differential calorimetry scanning (DSC) curve in heating measurement.[50-53] In this case, a small amount of noncrystallizable comonomer is sufficient to broaden the curve (corresponding to a broader crystal size distribution), and the peak position shifts toward lower temperature (corresponding to thinner lamellae).[50-53] It should be pointed out that T_m^c which is the copolymer counterpart of T_m^0 for homopolymer, is not experimentally observable. In practice, what can be measured is T_m^f which is the final observable melting temperature.

The thermodynamic characters of random copolymer crystalline are determined by the nature of crystal structure. When noncrystallizable comonomer content is low, it serves mainly as chain defect. In this case, noncrystallizable segments are intended to be excluded from lamellar crystals. Consequently, lamellae become thinner, which explains the fact that random copolymer crystals have lower melting temperature described above. Another factor that causes the suppression of melting temperature lies in the crystal imperfection, since noncrystallizable component is possible to be partially involved into lamellae, especially when the content is high. This effect is also accounted for the fact that unit cell dimensions of random copolymer crystals are often expanded, as compared with that of homopolymer counterpart.[54-57]

If the concentration of noncrystallizable component further increases, and exceeds a critical value (which varies with type of comonomer and its topological nature), crystal form may also be modified, as in this case, noncrystallizable segments can also be included.[58, 59] Usually these new crystal forms possess trigonal/hexagonal unit cell due to the nature of loose chain packing. For example, de Rosa et. al. performed powder and fiber diffraction analysis on a series of propylene-1-hexene (P-H) random copolymer with different 1-hexene concentrations. It was found that when the weight concentration of 1-hexene was below 10%, α -phase of polypropylene homopolymer which has a monoclinic unit cell was the only modification that can form. Once 1-hexene concentration exceeds 10%, new modification with trigonal unit cell and $R3c$ or $R\bar{3}c$ space group was identified. In both cases, 3_1 helix remains as the building block of the crystals. [58]

1.4 Model systems

1.4.1 Propylene-based random copolymer

Polypropylene, as one of the most widely used thermoplastic polymers, is valued by industrial community because of its cheap source, easy processing ability and pronouncing performance in many applications. It is obtained through polymerization reaction of propylene monomer which is a byproduct of petroleum refining. Due to the presence of methyl group, polypropylene exhibits steric order along the polymer chain, which is designated as tacticity. Three kinds of tacticities are possible for polypropylene. The homopolymer with all repeating unit possessing the identical tetrahedral bonding is called isotactic (iPP, see **Figure 1-3a**). If the

methyl groups are located randomly along the chain backbone, the polymer is atactic (aPP, see **Figure 1-3c**). The alternating copolymer is named syndiotactic (sPP, see **Figure 1-3b**). Due to the high degree of order, iPP is easy to crystallize and has the highest degree of crystallinity as compared with the other two.

Recently, iPP research has been undergoing a revival stemmed from attempts to further broaden its potential applications by using copolymerization technique. In this way, new species of propylene-based random copolymers can be synthesized, varied in properties due to comonomer type, its content and sequence distribution. Random copolymer consisting of one or more crystallizable species confers a promising material that combines advantages of both plastic and elastic polymers, making it possible to generate elastomers with acceptable mechanical strength, as well as sound elasticity. Regardless of its industrial importance, propylene-based random copolymer renders rich experimental phenomena such as polymorphism, morphology, preferred orientation under external field, etc., in polymer crystallization; and is therefore frequently chosen by researchers as a model system to study structure-property relationship of semi-crystalline polymers. In this thesis, isotactic propylene-1-hexene (P-H) and propylene-1-butene (P-B) random copolymers with low content of comonomer (1-henene and 1-butene) were selected as model polymers. Crystallization behaviors under quiescent condition or induced by step-shear and stretching were tested by using time-resolved WAXS/SAXS techniques.

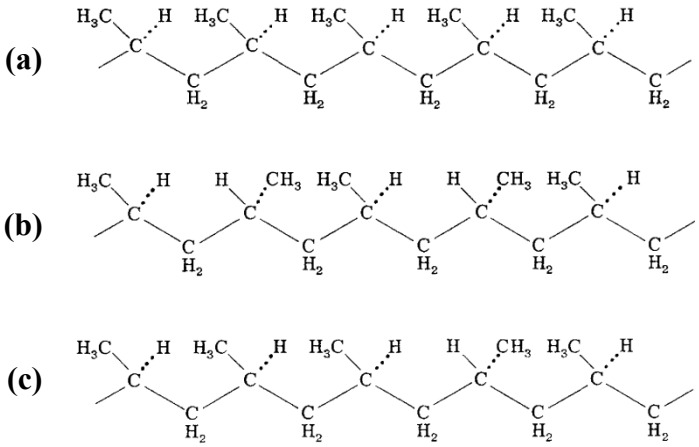

Figure 1-3. Chemical structure of isotactic polypropylene **(a)**; syndiotactic polypropylene **(b)**; and atactic polypropylene **(c)**.

1.4.2 Material used in this thesis

Both P-H and P-B random copolymer were synthesized in solution polymerization reactors using metallocene catalysts activated with dimethyl-aniliniumtetrakis-(pentafluorophenyl) borate. The content of comonomer is 5 mol%. The chain microstructures are characterized by nuclear magnetic resonance spectroscopy (NMR). The notations of characterization of random copolymer sequence needs to be introduced first.

Table 1-1. Formulas of triads characterizing random copolymer sequence.

$(AAA) = \frac{P_{BA}(1-P_{AB})^2}{P_{BA}+P_{AB}}$	$(BAB) = \frac{P_{AB}^2 P_{BA}}{P_{BA}+P_{AB}}$	$(ABB) = \frac{2P_{AB}P_{BA}(1-P_{BA})}{P_{BA}+P_{AB}}$
$(AAB) = \frac{2P_{AB}P_{BA}(1-P_{AB})}{P_{BA}+P_{AB}}$	$(ABA) = \frac{P_{AB}P_{BA}^2}{P_{BA}+P_{AB}}$	$(BBB) = \frac{P_{AB}(1-P_{BA})^2}{P_{BA}+P_{AB}}$

Table 1-2. Triads of P-H and P-B random copolymer used in this thesis.

P-H copolymer	Fraction	P-B copolymer	Fraction
(HHH)	0.001	**(BBB)**	0.002
(PHH)	0.016	**(PBB)**	0.010
(PHP)	0.051	**(PBP)**	0.046
(HPH)	0.004	**(BPB)**	0.005
(PPH)	0.110	**(PPB)**	0.111
(PPP)	0.819	**(PPP)**	0.827

The property of random copolymer is determined not only by the content of comonomers, but also by the comonomer sequence. Sequence is used to describe how one species of comonomer is distributed along the chain backbone. It can be represented as ABA, ABB, BBB, etc., if two comonomers are denoted as A and B. During polymerization process, the tendencies of self-propagation of A and B is controlled by the reactivity r_A and r_B. For truly random

copolymerization, $r_A \times r_B = 1$, and the combination of comonomer A and B follows the first order Markov statistics. Six triads can be defined to characterize the sequence, which is listed in **Table 1-1**, with P_{AB} and P_{BA} being the condition probabilities. For our P-H and P-B random copolymer, we use the combination of P and H, or P and B to represent triads, which is listed in **Table 1-2**.

2 2D WAXS/SAXS Pattern Simulation

2.1 General theory: the notations

Two processes are involved in a scattering experiment, namely scattering of incident beam by scatterers and the interference of scattered secondary waves (assume high-order scattering is weak and negligible). Electromagnetic waves can interact with matter via various ways; it can be absorbed and scattered with or without frequency shift.[60, 61] So far as scattering is considered, whether or not scattering takes place with a change of frequency defines three different approaches that can be utilized to study structure and dynamics of matter. Scattering without change of frequency is called elastic scattering. A small shift of frequency that can only be probed as a line-broadening effect is called quasi-elastic scattering which is attributed to slow motion such as translation and rotation of particles. Similarly, inelastic scattering is defined under situations when large frequency shift is observed. Raman spectroscopy in which the frequency shift is caused by fast dynamics of molecules such as vibration falls into this category.

This thesis reports crystallization of random copolymer studied by using wide- and small-angle X-ray scattering (WAXS/SAXS) techniques that belong to elastic scattering class, focusing on spatial correlation of the system. All experiments are performed in the Fraunhofer diffraction regime where Fourier transform is the essential tool to bridge the density distribution in real space and the intensity map in reciprocal space.[60-63] General theories of WAXS and SAXS are briefly discussed below, followed by a section treating the special case of fiber scattering in the next section and the experimental practice.

An intuitive way to think of scattering phenomenon is pictorial description of Bragg's law, as shown in **Figure 2-1a**.[63] The directions of incident and scattered beams are defined by using two unit vectors $\mathbf{S_0}$ and $\mathbf{S_1}$, respectively. **Figure 2-1a** demonstrates the condition of scattering from a 2D lattice composed of a series of crystallographic planes. The path difference of incident and scattered beams between two adjacent planes is $|\mathbf{AC}|+|\mathbf{BC}|$ which is related to inter-plane distance d through the Bragg's law $1/d=(2/\lambda)\sin\theta$ where 2θ is the scattering angle and λ is the wavelength of the X-ray beam. Bragg's law needs not to be applied solely to

crystalline system, but is a general rule to relate characteristic distance of periodicity with interference of secondary waves at all length scales. In this sense, there is no fundamental difference between WAXS and SAXS, and the only requirement for observation of intensity maxima due to positive superposition of scattered wave is that the studied system exhibits a certain degree of order at the right length scale falling into the detection range of scattering experiment.

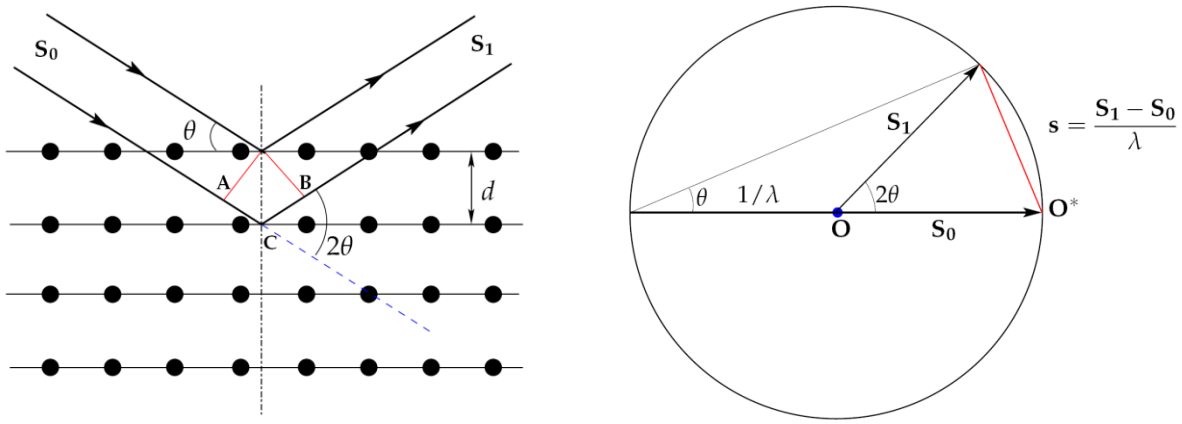

(a) **(b)**

Figure 2-1. Demonstration of Bragg's law using 2D lattice **(a)**; and Ewald construction **(b)**. Detailed explanation can be found in the context.

A more useful demonstration of Bragg's law is Ewald's construction as shown in **Figure 2-1b** in which Ewald sphere and reciprocal lattice are two major elements to understand the scattering process.[63] The circle with a radius of $1/\lambda$ is defined as Ewald sphere and the point $\mathbf{O}^*$ is the center of reciprocal space. $\mathbf{O}$ is the center of Ewald sphere around which $\mathbf{S_0}$ and $\mathbf{S_1}$ as defined before form a scattering angle 2θ. A scattering vector is naturally defined as $\mathbf{s} = (\mathbf{S_1} - \mathbf{S_0})/\lambda$. Following simple geometric derivations, we can rewrite the Bragg's law as follows

$$s = |\mathbf{s}| = 1/d = \frac{2}{\lambda}\sin\theta \qquad \textbf{(2.1)}$$

In **Eq.(2.1)**, s is the absolute value of scattering vector $\mathbf{s}$. The scattering vector is of primary importance; it has simple reciprocal relation to the d-spacing. Ewald construction nicely represents the physical requirement of a successful detection of scattering intensity: Ewald

sphere must intersect with the intensity distribution in the reciprocal space. This intensity distribution has various names depending on its nature, or more precisely, the structure of the system in real space. It is called reciprocal lattice for crystalline structure, pole figure for general cases of intensity maps,[64] and Polanyi sphere for system possessing fiber symmetry.[65, 66]

Figure 2-1b also delivers an important message that in scattering experiments (except for single crystal diffraction), the measured 2D scattering pattern represents intensities at thin shells with different radius in reciprocal space: it is the point intensity. This is important and the reason is two-fold. First, the ultimate goal of X-ray scattering analysis is to reproduce 3D real space structure based on information obtained in the reciprocal space. In some circumstances, a simple cut of Ewald sphere with the pole figure is sufficient to generate complete information. For example, in powder diffraction, crystals orient randomly, and hence produce evenly distributed intensity over the pole figure. In this case, orientation of the sample is not important; in any cases, the cut of Ewald sphere with the pole figure results in a series of rings (called Debye-Scherrer rings). However, for some other situations, if intensity distribution in the pole figure is anisotropic, orientation of the sample becomes critical. In this case, in order to have complete information of the structure of the sample, usually the sample is mounted in such a way that free rotation is allowed so that anisotropic density distribution in real space can be reconstructed successfully. This thesis mainly deals with system possessing fiber symmetry, thereby in principle, one orientation, namely placing the sample with its fiber axis perpendicular to the X-ray beam is enough to present entire intensity distribution over the Polanyi sphere. However, to test its validity, at least three orientations need to be employed. We will treat the detail in later sections in this chapter. Second, the intersection indicates that to change from 2D pattern to 1D intensity profile, appropriate averaging method needs to be used, which is important in some cases when 1D profile analysis such crystallinity determination is required. The detail will be treated in relevant parts in the following chapters.

As mentioned before, Fourier transformation is the tool to establish relationship between structures in real space and intensity in reciprocal space. Suppose in real space the system to be studied has a 3D density distribution characterized by $\rho(\mathbf{x})$, in reciprocal space the structure factor can be defined by its Fourier transform, written as[63, 67]

$$F(\mathbf{s}) = \int_V \rho(\mathbf{r}) e^{-i2\pi \mathbf{sr}} \mathrm{d}\mathbf{r} \qquad \textbf{(2.2)}$$

Neglecting all prefactor in the full expression of kinematic theory of X-ray scattering, the 3D intensity distribution in reciprocal space is simply the square of the modulus of $F(\mathbf{s})$ (**Eq.(2.3)**). Another approach to obtain $I(\mathbf{s})$ is directly Fourier transforming the autocorrelation function (spatial) of the density distribution. Therefore $I(\mathbf{s})$ has two possible forms

$$I(\mathbf{s}) = \mid F(\mathbf{s}) \mid^2 \qquad \textbf{(2.3)}$$

$$I(\mathbf{s}) = \int_V P(\mathbf{r}) e^{-i2\pi \mathbf{sr}} \mathrm{d}\mathbf{r} \qquad \textbf{(2.4)}$$

In **Eq.(2.4)**, $P(\mathbf{r})$ is the autocorrelation function or Patterson function as frequently used in crystallography community.[63, 68, 69] **Eq.(2.4)** is guaranteed by Wiener-Khinchin theorem. Although both **Eq.(2.3)** and **Eq.(2.4)** can be used to compute intensity distribution, one usually pick one of them which has the simplest form when applied to a given system. For the treatment of WAXS of crystal system, **Eq.(2.3)** is preferred as the structure can be easily obtained by considering all atomic groups in one unit cell. However, for disordered system, this approach is usually avoided since it will involve formidable calculation due to the large number of scattering units. In this case, one can first derive autocorrelation function and then directly perform Fourier transform on it. Be sure that all above expressions have simple forms because scattering vector, instead of its absolute value is used. Full expansion of those equations based on scalar value s is possible, which needs to employ a proper coordinate system. This will be discussed in detail in the following section.

2.2 Calculating fiber diffraction pattern

Using spherical coordinate, $I(\mathbf{s})$ can be written based on three parameters, s, ϕ and ψ, with the last two being termed as polar angle and azimuthal angle, respectively.[70] Fiber symmetry refers to the situation when density in real space or intensity in reciprocal space is independent of ψ. To consider preferred orientation of such system, first derive intensity distribution on the original coordinate (without performing orientation operation), defined as $I(s,\phi')$, and then performing orientation operation on it to generate fiber-averaged intensity

$J(s,\phi)$. This idea is demonstrated in **Figure 2-2** where all angles relating to two coordinate systems are shown.

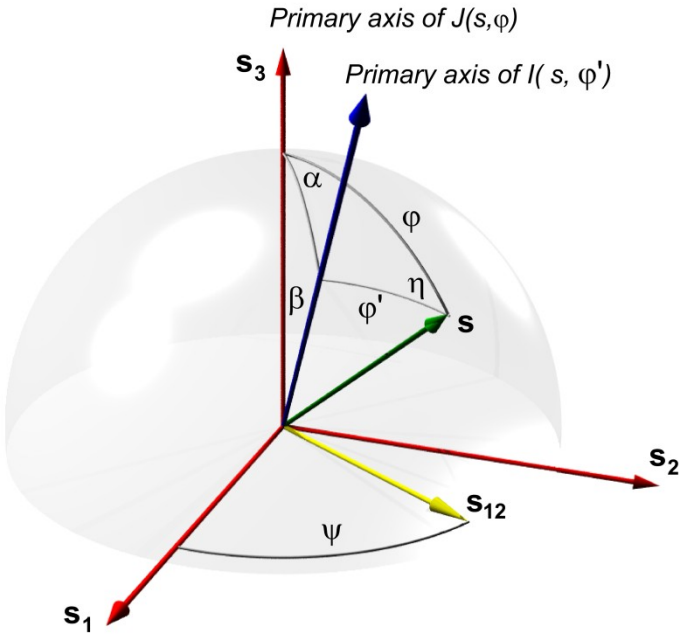

Figure2-2. Spherical trigonometric relationship between original coordinate system (without considering orientation) and the new coordinate system for fiber-averaged intensity calculation.

In **Figure 2-2**, β is the angle between primary axis of $J(s,\phi)$ and $I(s,\phi')$, and $g(\beta)$ defines the orientation distribution function (ODF). Thus the $J(s,\phi)$ can be written as[71-73]

$$J(s,\varphi)=\frac{1}{4\pi}\int_0^{2\pi}\mathrm{d}\alpha\int_0^{\pi}I(s,\varphi')g(\beta)\sin\beta\mathrm{d}\beta \qquad \textbf{(2.5)}$$

The ultimate goal is to establish a direct relationship between $J(s,\phi)$ and $I(s,\phi')$. After going through spherical trigonometric derivations, it ends up with

$$J(s,\phi)=\int_0^{\pi/2}I(s,\phi')F(\phi,\phi')\sin\phi'\mathrm{d}\phi' \qquad \textbf{(2.6)}$$

with $F(\phi,\phi')$ being the integral kernel which is related to orientation distribution $g(\beta)$ via

$$F(\phi,\phi') = \frac{1}{\pi}\int_0^{\pi} g(\beta)\mathrm{d}\eta \qquad \textbf{(2.7)}$$

Eq.(2.6) and **(2.7)** are the general forms of treating preferred orientation problem for simple fiber symmetric system. Angle β is the only parameter used as the variable, and the orientation distribution is fully characterized by $g(\beta)$. It can be further modified to fit WAXS and SAXS conditions, which will be discussed in detail below. What needs to be pointed out is that finding an proper ODF which is able to generate analytical expression after going through **Eq.(2.6)** and **(2.7)** is not an easy task. As we will see below, there are only few cases that analytical solutions can be fully given.

Regardless of the general forms of $J(s,\phi)$ and $F(\phi,\phi')$, different normalization schemes are possible. This thesis will strictly follow the normalizations used by Burger, as they are more uniform and have simpler forms. A comparison of Ruland's original normalizations and the ones adopted in this thesis are listed below.[71-73]

Table 2-1. Comparison of two systems of normalization in fiber pattern simulation.

Ruland's	**Burger's**
$\int_0^{\pi/2} g(\beta)\sin\beta\mathrm{d}\beta = \frac{1}{4\pi}$	$\int_0^{\pi/2} g(\beta)\sin\beta\mathrm{d}\beta = 1$
$\int_0^{\pi/2} F(\phi,\phi')\sin\phi'\mathrm{d}\phi' = 4$	$\int_0^{\pi/2} F(\phi,\phi')\sin\phi'\mathrm{d}\phi' = 1$

2.3 WAXS condition: the sharp peak approximation

A perfect crystal in real space can be mathematically described using a triplet of δ-functions with each impulse representing an atomic group in reality. Here and thereafter the term atomic group will be used to refer to the repeating motif in a crystal, be it atom, molecule, or segment of polymer chain. The positions of the atomic groups in the lattice can be defined in real space based on three vector **a**, **b**, and **c**, which represents three edges of a unit cell. The Fourier transform of a δ-function triplet is another set of δ-functions in the reciprocal space, with

reciprocal relationship with that in the real space. The physics behind it is that intensities in other positions are extinct due to interference (because of the rigorous periodicity). Correspondingly, another three vectors $\mathbf{a}^*$, $\mathbf{b}^*$, and $\mathbf{c}^*$ can be defined in reciprocal space to describe intensity nodes. The entire expression can be written as

$$\begin{aligned} \mathbf{x}_j &= p_j\mathbf{a} + q_j\mathbf{b} + r_j\mathbf{c} \\ \mathbf{s}_{hkl} &= h\mathbf{a}^* + k\mathbf{b}^* + l\mathbf{c}^* \end{aligned} \tag{2.8}$$

where $\mathbf{x}_j$ is the spatial position of the j-th atomic group. p_j, q_j and r_j are its fractional coordinates in $\mathbf{a}$, $\mathbf{b}$ and $\mathbf{c}$ directions. Similarly, each hkl node is located in $\mathbf{s}_{hkl}$, with h, k and l being the magnitude of the unit vectors $\mathbf{a}^*$, $\mathbf{b}^*$ and $\mathbf{c}^*$. Structure factor in this case can be written as[63]

$$F_{hkl} = \sum_{j=1}^{n} f_j \cdot \exp[-2\pi i \mathbf{s}_{hkl}\mathbf{x}_\mathbf{j}] = \sum_{j=1}^{n} f_j \exp[-2\pi i(p_j h + q_j k + r_j l)] \tag{2.9}$$

where f_j is the atomic form factor. In our case, carbon atom is used as it is the main element of the chain backbone. It can be numerically expressed in exponential series which is well documented elsewhere.[74] All hydrogen atoms are ignored in pattern simulations in this thesis, which yields an error of about 2%. In **Eq.(2.9)**, the summation goes over all coordinates of atomic groups in one unit cell. These coordinates are determined by crystallographic approach and can be found in reported literatures. In this case, **Eq.(2.3)** has a more specific form

$$I_{hkl}(\mathbf{s}) = |F_{hkl}(\mathbf{s})|^2 \tag{2.10}$$

as only intensity in the (*hkl*) nodes are needed to calculate. The calculated intensity is the integral intensity or overall intensity for a given (*hkl*) plane, and is of major interest for crystallographer in single-crystal diffraction experiment. For powder scattering, crystals are oriented randomly, thereby the calculated intensity needs to be diluted over the spherical surface with a radius of s_{hkl}, and the powder-averaged intensity is written as

$$\overline{I_{hkl}(s)} = \frac{1}{4\pi s_{hkl}^2} I_{hkl}(\mathbf{s}) \qquad \textbf{(2.11)}$$

Eq.(2.11) implies that a δ-function is included, since vector form of s is used in the right hand term, and the intensity can only be detected at a series crystallographic planes. Therefore, substituting **Eq.(2.11)** into **Eq.(2.6)** produces a trivial result,

$$J(s,\phi) = \overline{I_{hkl}(s)} \cdot F(\phi, \phi_{hkl}) \qquad \textbf{(2.12)}$$

Eq.(2.12) is the equation that will be adopted to calculate fiber-averaged intensity $J(s,\phi)$ for crystal system. It is based on the sharp-peak (δ-function approximation) which is generally valid at the length scale where the system exhibit rigorous periodicity.[75, 76] It fails if original intensity distribution $I(s,\phi')$ is broad, such as most supramolecular structure of polymer at nanometer length scale as probed using SAXS technique. We will deal with this problem in the later section. **Eq.(2.12)** has an simple form because it only requires a direction multiplication of powder scattering intensity and the integral kennel. Now the key task is to find a proper ODF so that $F(\phi,\phi')$ can have analytical expression and can offer reasonable peak shape to fit experimental data. Possible choices of ODF will be discussed in detail in the later section.

2.4 A more general condition: an example for SAXS data analysis

Lamellar structure in semi-crystalline polymers is usually not rigorously ordered, resulting in relative broad intensity distribution which makes the integration in **Eq.(2.6)** an unavoidable step. Two approaches can be applied to this problem. Numerical integration is always possible but it is computationally expensive, especially for 2D whole-pattern simulation. A feasible alternative is to use Legendre expansion which will be discussed in detail in this section.

For a given s position, if the ODF $g(\beta)$, the original intensity distribution $I(\phi')$, and the fiber-averaged intensity distribution $J(\phi)$ can be expanded into Legendre polynomials as

$$g(\beta) = \sum_{0}^{\infty} a_n P_{2n}(\cos\beta) \qquad \textbf{(2.13a)}$$

$$I(\phi') = \sum_{0}^{\infty} b_n P_{2n}(\cos\phi') \qquad \textbf{(2.13b)}$$

$$J(\phi) = \sum_{0}^{\infty} c_n P_{2n}(\cos\phi) \qquad \textbf{(2.13c)}$$

where a_n , b_n and c_n are Legendre expansion coefficients, then these coefficients can be correlated by using additional theorem which yields

$$c_n = \frac{a_n b_n}{1+4n} \qquad \textbf{(2.14)}$$

In practice, c_n is what one needs to construct simulated fiber-averaged intensity (see **Eq.(2.13c)**); a_n and b_n are obtained from ODF and experimental data, respectively. **Eq.(2.13)** and **Eq.(2.14)** provide the procedure of calculating polar distribution of fiber-averaged intensity at a given s. The whole-pattern computation also requires modeling of intensity at various s.[72, 73]

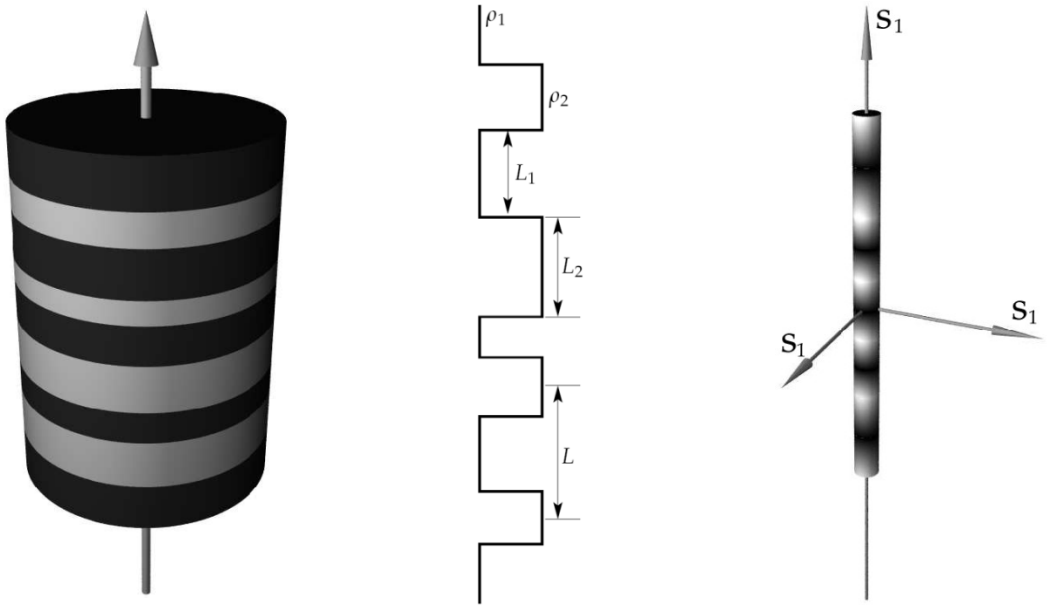

(a) **(b)** **(c)**

Figure 2-3. Cartoon illustration of a two-phase stack **(a)**; its density profile in the direction perpendicular to the layers **(b)**; and the corresponding intensity distribution in the reciprocal space**(c)**.

For lamellar structure in semi-crystalline polymers, stacking model and lattice model are often adopted to calculate the 1D scattering intensity profile. Details about the formalism of these two models can be found elsewhere.[77] Stacking model will be briefly discussed in the following context.[78, 79] Consider a two-phase stack which has a much larger lateral size as compared with its diameter, as shown in **Figure 2-3a**. The densities of two phases are denoted as ρ_1 and ρ_2, respectively. For semi-crystalline polymer, these are corresponding to the densities of lamellar crystals and amorphous layers. The thickness of the two phases are L_1 and L_2, and $L = L_1 + L_2$ is the inter-layer distance, or the long period that is used in SAXS theory (see **Figure 2-3b**). For such a system, the Fourier transform can be qualitatively illustrated in **Figure 2-3c**, described by three orthogonal coordinates, $\mathbf{s_1}$, $\mathbf{s_2}$ and $\mathbf{s_3}$. What of interest is the intensity distribution perpendicular to the layers, which is analytically given by

$$I_{1D}(s) = \frac{f}{s^2}\mathrm{Re}\left\{\frac{[1-H_1(s)][1-H_2(s)]}{1-H_1(s)H_2(s)}\right\} \qquad \textbf{(2.15)}$$

In **Eq.(2.15)**, Re represents the real part of an complex number. $H_1(s)$ and $H_2(s)$ are Fourier transform of statistical distribution of thickness 1 and 2; f is a prefactor. Again, to use **Eq.(2.6)**, powder averaged intensity distribution is required, and an extra s^2 should be divided to generate correct asymptotic behavior. Also, the lateral size may be finite, which makes the intensity distribution in s_{12} direction ($s_{12} = \sqrt{s_1^2 + s_2^2}$) not infinitely narrow, but has a bell-shape profile which can be empirically fit with proper distribution function denoted as $L_{12}(s_{12})$.With all these considerations, $I(s,\phi')$ can be finally written as[79]

$$I(s,\phi') = \frac{1}{4\pi s^2}\frac{1}{\pi s_{12}} I_{1D}(s_3) L_{12}(s_{12}) \qquad \textbf{(2.16)}$$

In **Eq.(2.16)**, 2D intensity distribution without considering orientation effect is separated into distributions along s_3 and along s_{12}, respectively. The $1/4\pi s^2$ represents the dilution of intensity over the pole figure, similar to the treatment of powder diffraction as described before. $1/\pi s_{12}$ is due to the fiber average of intensity along s_{12} direction, causing by the finite size effect.

Eq.(2.16), together with **Eq.(2.6)** give entire 2D SAXS intensity distribution with consideration of lateral size effect and preferred orientation. It can be fully computed using Legendre expansion approach discussed before. It should be pointed out that **Eq.(2.15)** only consider infinite long stacks. Finite size stacking problem has also being treated, which can be found elsewhere.[78] Several choices are possible for $L_{12}(12)$ among which Gaussian and Lorentzian distribution are frequently used. The reciprocal integral width ($1/w$, with w being the integral width of $L_{12}(12)$) gives an estimate of lateral size, which is similar to the treatment of Scherer's equation to derive crystal size in WAXS data analysis.

2.5 Parallel orientation, perpendicular orientation and oblique orientation[73]

Before discussing possible options of ODFs, we need to classify major orientation modes because it is important for deciding what ODF to choose. **Figure 2-4** shows three possible orientation modes for simple fiber symmetric system. A system possessing simple fiber symmetry can be characterized by two axes, namely, a fiber axis (FA) around which scattering intensity is a constant at all azimuthal angle, and a principle axis of rotation (PA) for scatters. In **Figure 2-4a**, FA is parallel to PA, which is termed as parallel orientation. ODF is peaked at 0^{o} in this case. **Figure 2-4b** illustrates the situation of perpendicular orientation, and ODF is peaked at 90^{o}. A complicated situation where FA and PA have an oblique angle, corresponding to an off-axis ODF, is shown in **Figure 2-4c**. This is termed as oblique orientation.

It will be shown later that the choice of proper ODF is dependent on orientation mode. So far no ODF has been constructed so that it can be applied to all three situations, and can generate analytical solution to $F(\phi,\phi')$. There are limited cases that simple OPFs can be used for both parallel and perpendicular orientations. The oblique orientation is important for four-point pattern calculation in SAXS data analysis; but unfortunately, there is no analytical solution to $F(\phi,\phi')$ so far. We will discuss an alternative approach later.

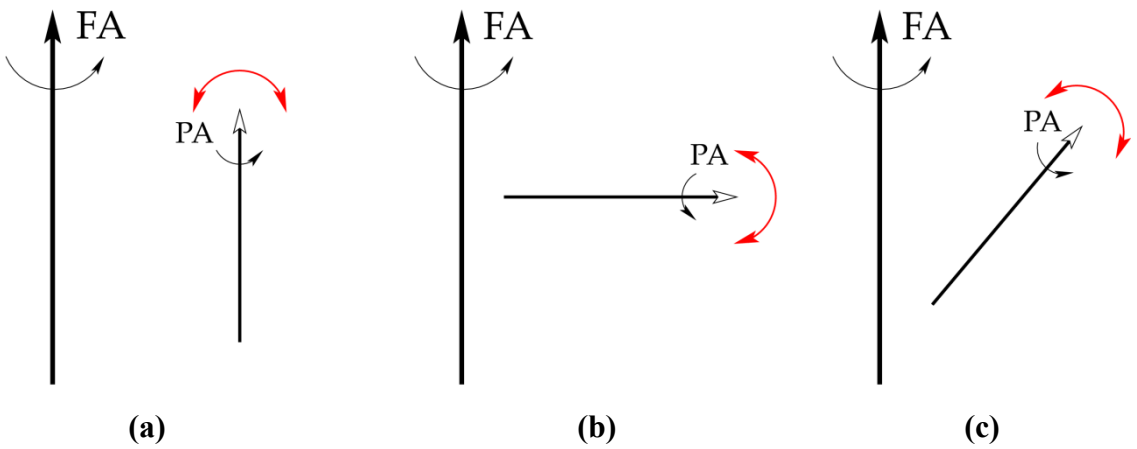

Figure 2-4. Illustration of three orientation modes, defined by a fiber axis (FA) and a principle axis of rotation (PA). **(a)** Parallel orientation; **(b)** perpendicular orientation; and **(c)** oblique orientation.

2.6 Examination of transformation kernel (ODF)

2.6.1 Onsager distribution[73, 75]

Onsager distribution was first created by Lars Onsager to describe the interaction of rod-like particles, and was independently derived by Burger to model polar distribution of scattering intensity. Onsager ODF can be written as

$$g_O(\beta) = p\cosh(p\cos\beta)/\sinh(p) \tag{2.17}$$

Eq.(2.17) can produce analytical solution when substituting to **Eq.(2.7)**, and the integral kernel $F(\phi,\phi')$ has the form

$$F_O(\phi,\phi') = \frac{p}{\sinh(p)}\cosh(x)I_0(y) \tag{2.18}$$

where $x = p\cos\phi\cos\phi'$, $y = p\sin\phi\sin\phi'$, and p is the parameter determines the breadth of the profile, namely, the orientation distribution of scatterers. I_0 is the modified Bessel function of the first kind of order zero. A demonstration of Onsager ODFs at various p is shown in **Figure 2-5**.

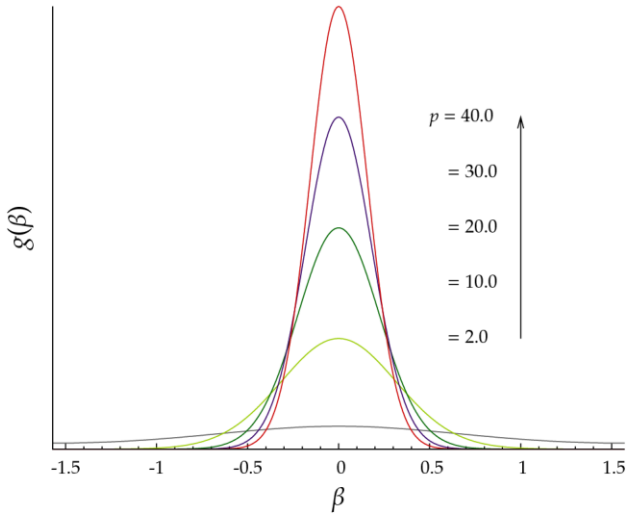

Figure 2-5. Onsager distribution at different p values (distribution width).

The transformation kernel $F(\phi,\phi')$ in this case has a nice bell-shape profile with a short tail, which makes it a reasonable choice to describe distribution in reality. However, Onsager function is not able to generate analytical solution for perpendicular and oblique orientation conditions. Several possible options for those cases are described below.

2.6.2 Poisson kernel[71, 73]

Ruland first use Poisson kernel to treat this problem. It has the following form:

$$g_p(\beta) = \frac{\sqrt{p}(1+p)}{\text{atanh}(\sqrt{p})}[(1+p)^2 - 4p\cos^2\beta]^{-1} \qquad \textbf{(2.19)}$$

Figure 2-6 shows examples of Poisson ODF. The advantage of Poisson kernel is that it can be used for both parallel and perpendicular orientations, as shown in **Figure 2-6a** and **2-6b**, respectively. A positive p represents parallel orientation; perpendicular orientation condition can be characterized by a negative p. This property makes it very convenient to use. However, it presents a sharp peak and a long tail, which resembles Lorentzian distribution, and may not be realistic in most cases.

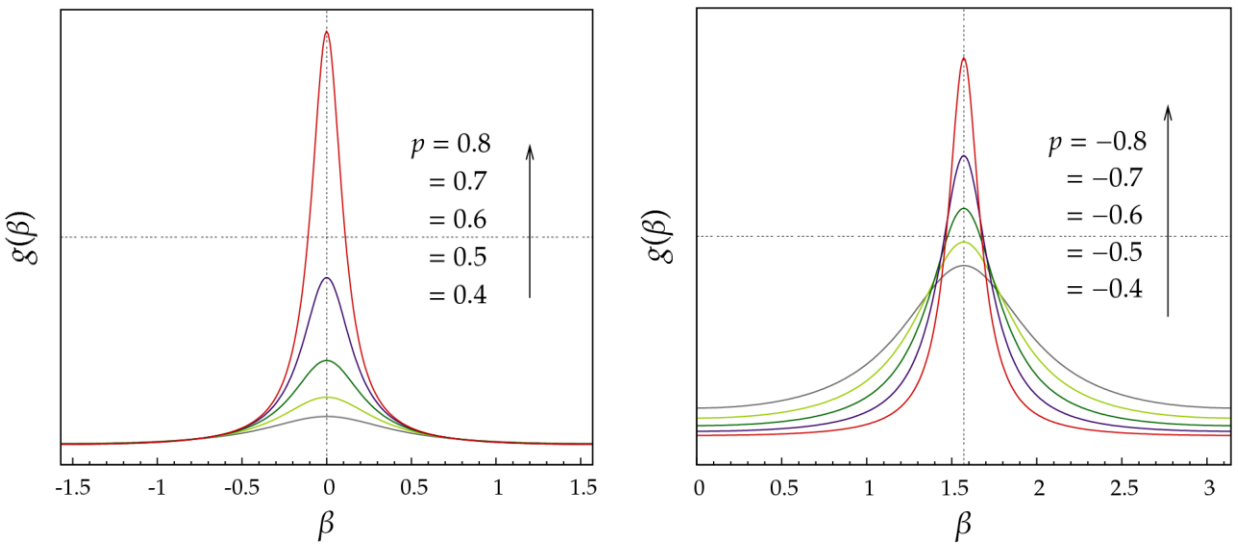

Figure 2-6. Poisson Kernel at different p values. Both profiles with positive **(a)** and negative p **(b)** are shown.

Substituting **Eq.(2.19)** into **Eq.(2.7)** results in an analytical solution as written below:

$$F_P(\phi,\phi') = \frac{\sqrt{p}}{2\ \mathrm{atanh}(\sqrt{p})}\left[\frac{1}{\sqrt{(1+p+2\sqrt{p}x)^2-4py^2}}+\frac{1}{\sqrt{(1+p-2\sqrt{p}x)^2-4py^2}}\right] \quad \textbf{(2.20)}$$

Be sure that in this case, p ranges from -1 to 1.

2.6.3 Maier-Saupe orientation distribution[73]

The Maier-Saupe ODF is defined as

$$g_M(\beta) = c\exp(p\cos^2\beta) = c'\exp(-p\sin^2\beta) \quad \textbf{(2.21)}$$

where c is the normalization prefactor which is given by

$$c = \frac{2\sqrt{p}}{\sqrt{pi}\ \mathrm{erfi}(\sqrt{p})} \quad \textbf{(2.22)}$$

$\mathrm{erfi}(x)$ is the imaginary error function defined as $\mathrm{erfi}(x) = \mathrm{erf}(x)/i$. Maier-Saupe ODF is another distribution function that allows to be applied to both parallel and perpendicular orientations, with p being specified as positive or negative values, respectively. But it is not convenient to use because a full closed form solution is still unavailable. Burger expanded the solution to **Eq.(2.7)** using a series of modified Bessel functions of the first kind, and the transformation kernel has the following form

$$F_M(\phi,\phi') = c\exp[p(x^2+y^2/2)]\left[I_0(2pxy)I_0(py^2/2) + 2\sum_{n=1}^{\infty} I_{2n}(2pxy)I_n(py^2/2)\right] \quad \textbf{(2.23)}$$

Expansion in Bessel function usually shows good property of convergence, hence **Eq.(2.24)** can produce reasonable profile by using only several terms. Examples of its application can be found elsewhere.[16]

2.6.4 $|\cos\beta|^p$ and $|\sin\beta|^p$ orientation distribution[75, 80]

$|\cos\beta|^p$ and $|\sin\beta|^p$ can be used as ODF to describe parallel and perpendicular orientation, respectively, as shown in **Eq.(2.24a)** and **Eq.(2.24b)**

$$g_C(\beta) = (1+p)|\cos\beta|^p \quad \textbf{(2.24a)}$$

$$g_S(\beta) = \frac{2\Gamma[(3+p)/2]}{\sqrt{\pi}\Gamma(1+p/2)}|\sin\beta|^2 \quad \textbf{(2.24b)}$$

Analytical solution to **Eq.(2.7)** is available for parallel orientation, as given in the reference, but not for perpendicular orientation.

2.7 Treating the oblique orientation[75]

We now consider the most complicated orientation mode, the oblique orientation, as shown in **Figure 2.4c**. Since in this case the ODF is peaked at an off-axis position, an intuitive approach is to shift the original ODF by an angle β_0, as shown below

$$\hat{g}(\beta) = g(\beta - \beta_0)$$

However, it becomes clear immediately that this modification would not be able to produce proper normalization. So far there is no simple ODF for oblique orientation that can be used conveniently (compare with Onsager distribution or Poisson kennel). A possible way out is to use transformation kernel F directly as the ODF, since as shown in **Table 2-1**, $F(\phi,\phi')$ is well normalized at arbitrary ϕ' s. The new ODF can be written as

$$\hat{g}(\beta) = F(\beta, \beta_0) \qquad \textbf{(2.25)}$$

Then, Legendre expansion approach can be used to reconstruct the fiber-averaged intensity.

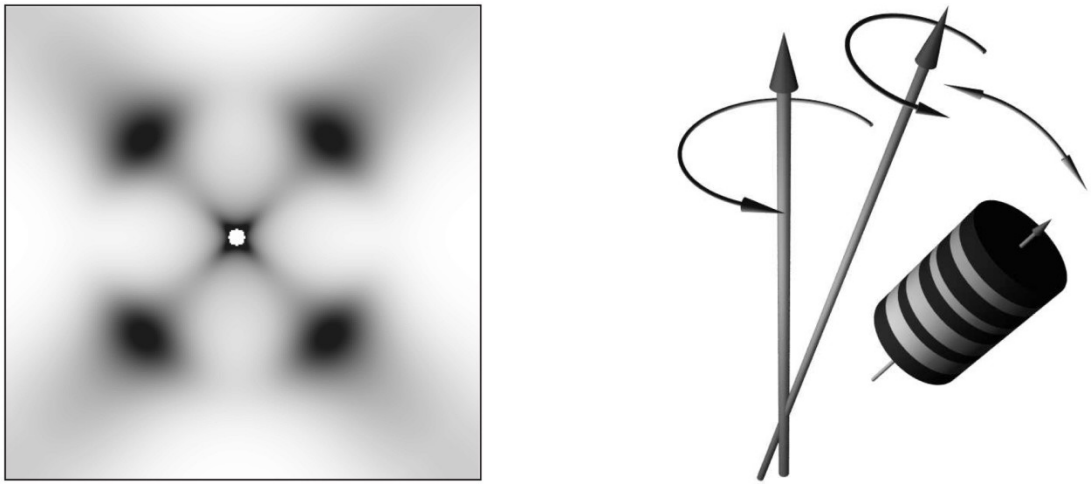

(a) **(b)**

Figure 2-7. Four-point SAXS pattern simulated using ODF defined in **Eq.(2.25) (a)**; and corresponding real space structure showing oblique orientation **(b)**.

Oblique orientation is important in the description of four-point pattern in SAXS experiment, which is frequently met when semi-crystalline polymer is uniaxially stretched. By using stacking model (**Eq.(2.15)** and **(2.16)**) and $\hat{g}(\beta)$ as defined in **Eq.(2.25),** and by employing Legendre expansion approach (**Eq.(2.13a-c)**), the 2D whole-pattern can be calculated. An example of SAXS pattern of oblique orientation of lamellar stacks with $\beta_0 = 40°$ is shown in **Figure 2-7a**, and a schematic illustration of corresponding real space structure in **Figure 2-7b**.

2.8 Experimental considerations

2.8.1 Experimental set-up[76, 81]

All WAXS/SAXS measurements were carried out at the Advanced Polymer Beamline (X27C) in the National Synchrotron Light Source (NSLS), Brookhaven National Laboratory (BNL). The wavelength of the X-ray beam was 1.371 Å. The beam diameter was 0.3mm. All scattering images were captured *in-situ* by a 2D MAR CCD camera, with a resolution of 1024 × 1024 pixels. The exposure time for data collecting varies; usually 15s was able to produce acceptable 2D scattering pattern. The scattering angle was calibrated by Al_2O_3 for WAXS measurement and by AgBe for SAXS. The sample-to-detector distance varies in each set of experiment, and is dependent on scattering geometry (SAXS or WAXS). The detail will be given in relevant places in the following chapters. Roughly it is 120 *mm* for WAXS measurement and *1900* mm for SAXS measurement.

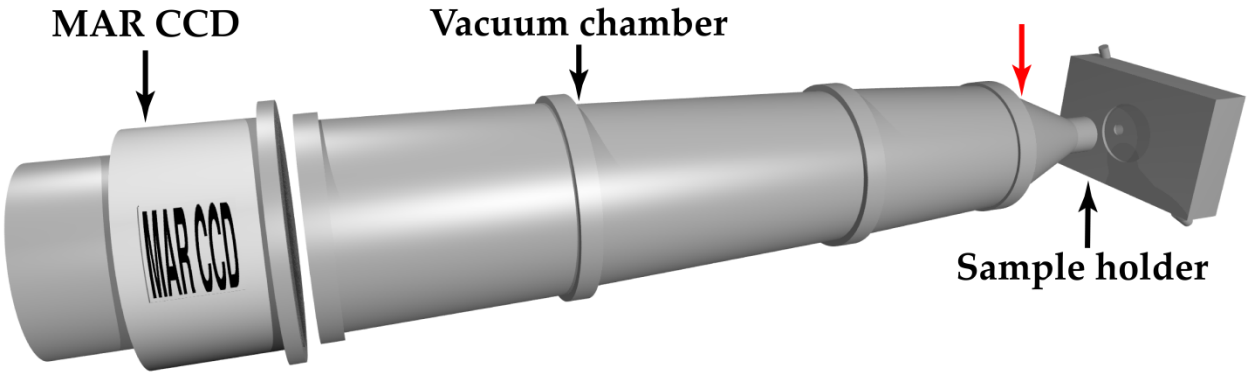

Figure 2-8. Schematics of synchrotron-based X-ray scattering set-up. Detailed explanation can be found in the context.

Figure 2-8 demonstrate the layout of SAXS/WAXS set-up in the X27c Beamline hatch. X-ray beam goes from left to right. Collimation system where the original X-ray beam was reshaped and collimated by three pin-holes before the sample holder is not shown. In SAXS experiment, after striking on the sample, the scattered beam passes through a vacuum chamber designed to avoid unwanted air background scattering, and then reaches a 2D MAR CCD camera which is used to record 2D pattern for all experiments. Vacuum chamber is not needed in WAXS experiment, and the MAR CCD camera is moved to a position right after the sample holder, as shown by the red arrow in **Figure 2-8**. Different sample holders are possible (**Figure 2-8**

demonstrates the shear stage as an example); the details of sample holder in different experiments will be introduced in detail in experimental section of each of the following chapters.

2.8.2 Testing the fiber symmetry approximation

2D scattering pattern calculation discussed in this chapter is based on the assumption of simple fiber symmetry which means that system is symmetric in both principal axis of rotation and fiber axis (see **Figure 2-4**). In practice, the treatment of scattering problem on system deviated from simple fiber symmetry will be very complicated, if not impossible. It should be pointed out that the symmetry around both axes does not necessary mean that an individual scatterer can possess such high order symmetry, but can be fulfilled by a statistical average over many scatterers, as scattering experiment itself is a process of performing ensemble average. Both experiments in the presence of step shear (weak flow) and uniaxial tensile force were performed, and it turned out that fiber symmetry approximation can be used to analyze our data.

A simple way of testing the validity of fiber symmetry is to shoot the X-ray in three perpendicular directions with respect to the sample, as shown in **Figure 2-9** where a propyene-1-buene random copolymer (P-B, details about experiments on this sample will be discussed in relevant chapters) uniaxially stretched to strain = 2.0 was tested with three perpendicular orientations in WAXS measurement. The stretching direction is vertical, and hence the fiber axis is assumed to be in consistent with this direction. It was found that the face-on and edge-on experiment (shooting X-ray in two perpendicular directions around the fiber axis) showed almost identical diffraction patterns (see also **Figure 2-10**); while the diffraction is isotropic if the X-ray beam direction is in parallel to the fiber axis. This proves scattering is identical around the fiber axis.

Shear experiment is more complicated, as shear flow is composed of a stretching component and a rotational component. In this case, fiber axis is possible to have two directions. Same test as performed for sample being stretched has not been done for sheared sample, as the shape of the sample (flat and round) makes it difficult to be mounted with different orientations. However, as will be shown in later chapter, pattern calculated with assumption of simple fiber symmetry can fit the data quite well. Therefore, it still applies to the condition of sheared sample, at least to the first approximation.

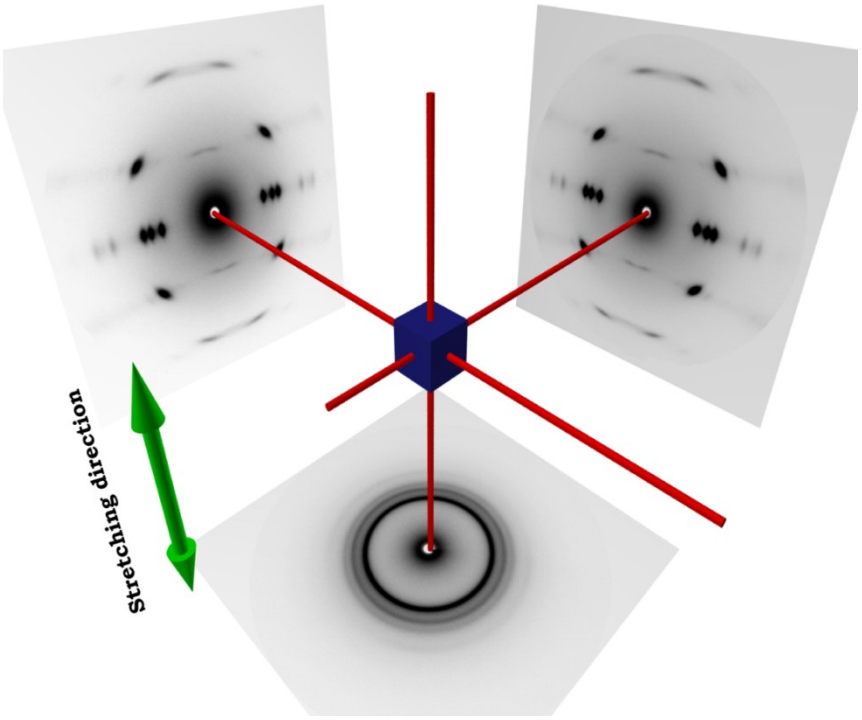

Figure 2-8. Demonstration of testing fiber symmetry by shooting X-ray from three perpendicular directions. In practice, X-ray beam direction is fixed, and sample can be oriented.

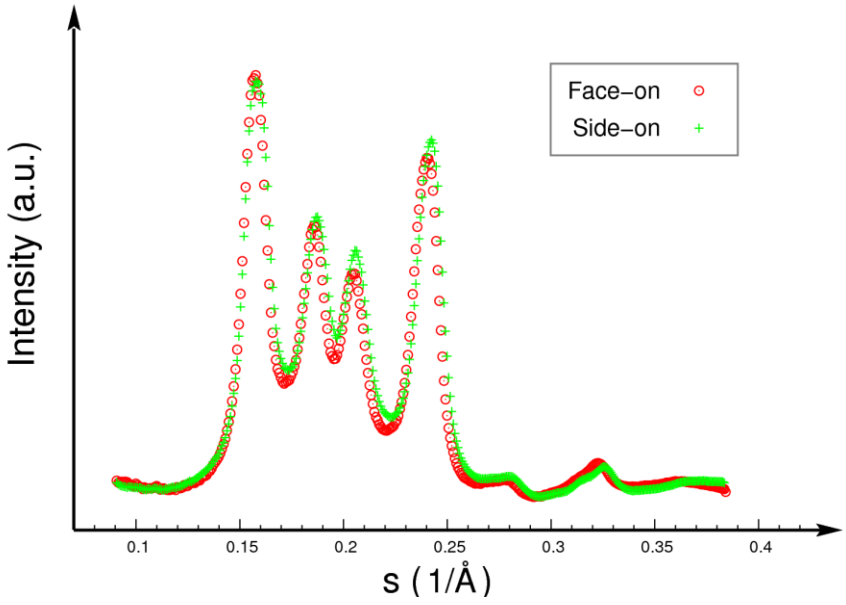

Figure 2-9. 1D scattering profiles obtained from two perpendicular directions around the fiber axis. Intensities are scaled with consideration of sample thickness difference.

2.9 Summary

This chapter reviews the general theory of X-ray scattering that is applicable to both WAXS and SAXS. Methodology of 2D fiber scattering pattern simulation is introduced. For crystal system at atomic length scale as revealed by WAXS, sharp peak approximation was made and the fiber-averaged intensity was determined by simple multiplication of powder diffraction intensity and the transformation kernel F. The former can be obtained by conventional crystallographic approach and the later requires careful choice of ODF that is preferred to have analytical solution to the transformation kernel. In the SAXS regime, when rigorous order is not achievable such as the case of lamellar structure in semi-crystalline polymer, the sharp peak approximation fails and the integration in **Eq.(2.6)** is not avoidable. In this case, the Legendre expansion approach was introduced to make the 2D SAXS pattern calculation more feasible. The 2D distribution of intensity can be decoupled into a polar distribution solely caused by orientation effect and an intensity distribution in s_{12} direction due to the lateral width effect. Intensity in s_3 direction is given by possible two-phase models among which the stacking model was introduced.

Possible options of ODFs were discussed. For parallel orientation, Onsager function is recommended because of its nice peak shape and its simplicity. Poisson kernel is so far the only analytical ODF that is applicable to both parallel and perpendicular orientation, but its shape is not realistic for practical purpose. Maier-Saupe ODF is also possible to describe both orientation modes, but cannot produce analytical solution to the transformation kernel F. A feasible solution is to expand it into modified Bessel function series that shows good convergence. $|\cos(\beta)|^p$ and $|\sin(\beta)|^p$ types of ODFs are also discussed but they don't offer particular advantages over others. Simple shift of β angle in ODF fails to produce proper normalization for oblique orientation. In this case, known transformation kernel is recommended to be directly used as the ODF, and the integration in **Eq.(2.6)** needs to be solved either numerically or by Legendre expansion approach. Experimental details of WAXS/SAXS set-up were described. The validity of the fundamental assumption, the simple fiber symmetry was discussed. It is an excellent approximation for uniaxial stretching measurement; but the condition may be more complicated for sheared sample.

3 Quiescent Crystallization

3.1 Introduction

In this chapter, the crystallization of propylene-1-hexene (P-H) with low content of 1-hexene comonomer is examined in detail, focusing on the influence of the temperature. Experiments were performed at quiescent condition. As has been introduced in chapter 1 that when the concentration of noncrystallizable comonomer is low, no new crystal forms can grow from copolymer matrix, that are different from those grown from homopolymer composed of only crystallizable monomer. As for isotactic polypropylene (iPP), three crystal modifications have been identified, namely, α, β and γ-phase. Although only α-phase will be dealt in this chapter, all modifications have been observed in shear- or stretching-induced crystallization. Therefore, the unit cell types, symmetry operations and chain arrangement in the unit cells of these three polymorphs will be briefly introduced in this section.

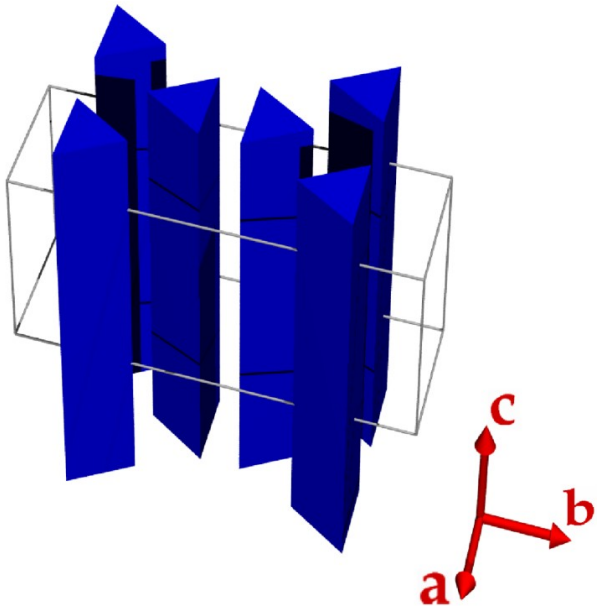

Figure 3-1. Cartoon illustration of a unit cell of α-form crystal of iPP homopolymer.

The α-form polymorph was the first firmly identified crystal form of iPP.[82] It has a monoclinic unit cell with the cell parameters of a = 6.65 Å, b = 20.96 Å, c = 6.5 Å, and β = 99.2°. Chains align in parallel to the c-axis. For iPP, 3_1 helix with a length of 6.6 Å is the

building block of all three polymorphs. Therefore, charity is important in chain packing in the unit cells of iPP. For the purpose of simplicity, prisms will be used to represent arrangement of polymer chains in the unit cells. Each α-phase unit cell contains 6 polymer chains, following the space group C2/c. A cartoon illustration of the α-form unit cell of iPP is shown in **Figure 3-1**. Since polymer chains are all parallelly aligned with respect to the *c*-axis, the α-phase is stable if crystals adopt a *c*-axis orientation in the presence of uniaxial tensile force. The detail will be discussed in chapter 5 and 6.

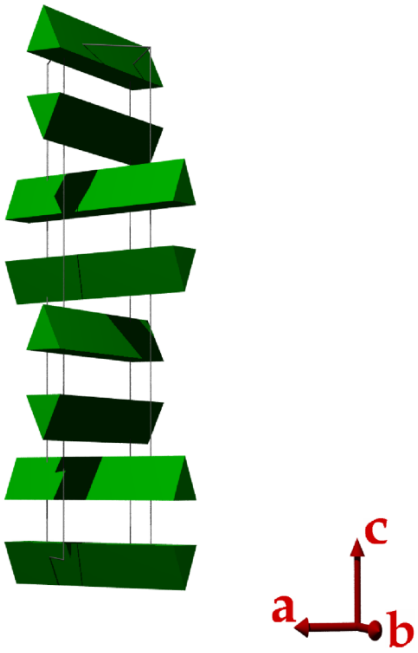

Figure 3-2. Cartoon illustration of a unit cell of γ-form crystal of iPP homopolymer.

The γ-form crystal is often grown (co-crystallize) within the α-form crystal in quiescent condition. It is also favored due to chain defect or special crystallization conditions such as high pressure. Brückner et al.[83, 84] first solved the unique structure of the γ-form crystal with an unusual non-parallel chain packing with respect to the *c*-axis. In this case, chains pile along the *c*-axis in a cross-hatched style, forming a large orthorhombic unit cell (a = 8.54 Å, b = 9.93 Å, c = 42.41 Å). The diagonal of the *ab*-plane has a length of 13.0 Å which is about the same size of the length of two 3_1 helices. There are totally 4 layers, 8 chains in one unit cell; each layer contains 2 chains with opposite charity. The symmetry operation follows *Fddd* space group. A cartoon illustration of γ-phase is shown in **Figure 3-2**.

The β-phase is the last piece of the puzzle of iPP polymorphism. It was solved by Brückner et. al.[85], and independently by Lotz.[86] β-form is the most disordered modification; and hence is thermodynamically unstable. This is one of the reasons that it was bought to attention a long time ago, but was only fully characterized in the early 1990's. It has a trigonal or hexagonal unit cell ($a = b = 11.02$ Å, $c = 6.49$ Å) with three chains align in parallel to the c-axis. The a and b arms are large, which explains the low density and high degree of disorder. The packing energy calculation showed that $P3_121$ space group produces the optimal packing.[87] A cartoon illustration of β-phase is shown in **Figure 3-3**.

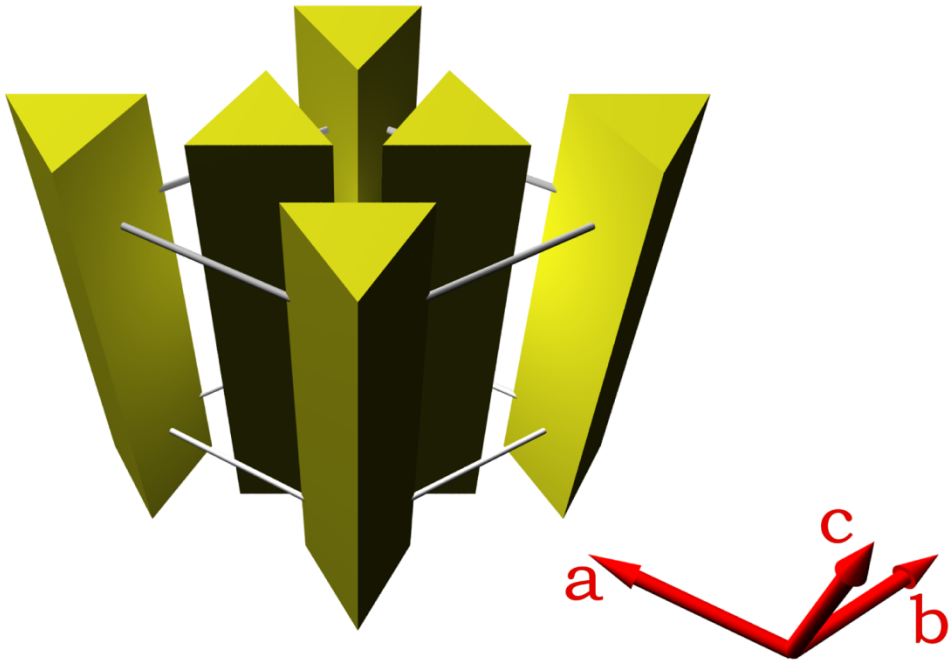

Figure 3-3. Cartoon illustration of a unit cell of β-form crystal of iPP homopolymer.

3.2 Materials and experimental protocols

The P-H random copolymer was synthesized by ExxonMobil Chemical Company. The number average molecular weight (M_n) of the chosen sample was 14,300 g/mol and the molecular weight distribution was 2.8. The mole fraction of hexene component was 5%. The endothermic peak of DSC trace in heating experiment was 126.4 ^oC (with 10 ^oC/min heating rate).

The temperature protocol for synchrotron X-ray experiment was as follows. The sample was first melted at 200 ^{o}C for 5 min to remove all residual stress and thermal history. After that, the sample was quenched (at a cooling rate of 100 ^{o}C/min) to desired temperatures for isothermal crystallization experiment. An INSTECH hot stage equipped with a precision temperature controller was used to heat treat the samples, where the accuracy of the temperature control was ± 0.1 ^{o}C. The isothermal crystallization process was monitored *in-situ* by time-resolved SAXS/WAXS techniques (see chapter 2). Four temperatures, 40 ^{o}C, 60 ^{o}C, 80 ^{o}C and 100 ^{o}C, were chosen for the study. Experimental set-up of combined SAXS/WAXS measurements has been introduced in chapter 2. In this study, the exposure time for data collection was 30 *s*. The sample-to-detector distances were 1890.0 *mm* for SAXS measurement and 120.6 *mm* for WAXS measurement.

3.3 Results and Discussion

3.3.1 A general description of crystallization process

The crystal structure P-H random copolymer can be determined by the WAXS method. **Figure 3-4** shows 1D intensity profiles from the final 2D WAXS patterns of P-H copolymer fully crystallized under 100 ^{o}C, 80 ^{o}C, 60 ^{o}C and 40 ^{o}C, respectively. In these profiles, the integrated diffraction intensity is plotted against the absolute value of scattering vector which has been discussed in chapter 2. Although varied in magnitude, all profiles in **Figure 3-4** exhibit four diffraction peaks located at the s values of 1.57, 1.87, 2.06 and 2.41 nm^{-1}. These peaks match the characteristic reflections from the α-phase crystal form of iPP homopolymer, and they can be indexed as (110), (040), (130) and (111) reflections, respectively.[88]

To investigate the crystallization kinetics, the evolutions of crystallinity as a function of time at different temperatures are shown in **Figure 3-5a**. The degree of crystallinity was estimated from the 1D WAXS profiles, by dividing the sum of areas of all crystalline peaks by the total area (this procedure was carried out by deconvoluting the diffraction profile into crystalline and amorphous components using a curve fitting program). The 'crystallinity' obtained in this way should be termed as relative crystallinity index, for it is not truly equivalent to the absolute value of crystallinity. Hereafter, such "crystallinity" will be used to show the general trend of the crystallization process in this study.

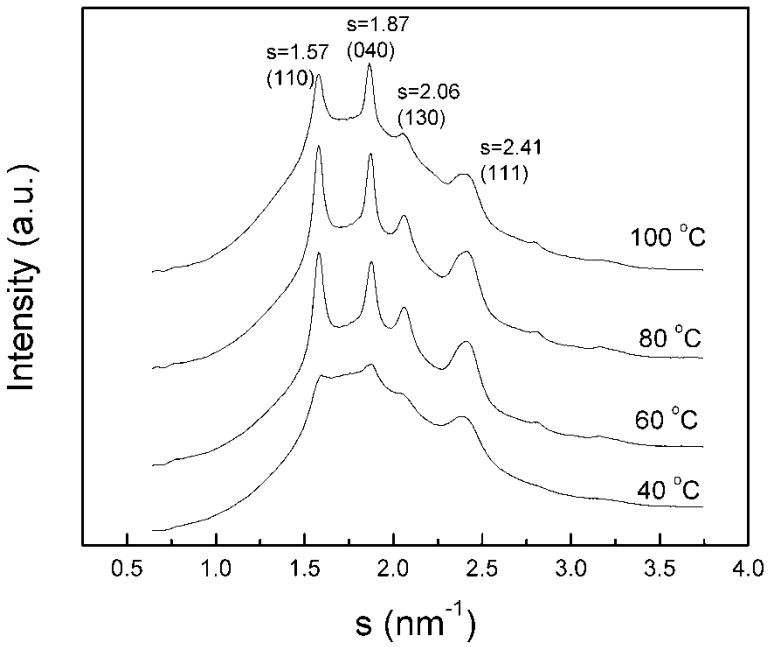

Figure 3-4. Final integrated WAXS profiles of P-H copolymer fully melt crystallized at 100 °C, 80 °C, 60 °C and 40 °C.

In **Figure 3-5a**, the crystallinity curve of sample isothermally crystallized at 100 °C shows a typical behavior, containing three stages: an early stage that can be called the induction period where crystallinity equals zero, an intermediate stage where crystallinity increases with time quickly, and a late stage where crystallinity reaches a plateau value, indicating crystallization is fully accomplished.[37, 89] As the crystallization temperature decreases, the crystallization kinetics becomes faster. This can be clearly seen from **Figure 3-5b** which displays induction time and crystallization half time obtained from **Figure 3-5a** at different temperatures. Both parameters increase (i.e., the slower crystallization rate) with crystallization temperature. In **Figure 3-5b**, the induction time was determined by extrapolating the interception between the early stage and intermediate stage, where the crystallization half time is the time span that the sample requires to achieve half of its final crystallinity. The highest crystallinity achieved in the chosen sample was around 12 % when samples were annealed at temperatures of 60 °C and 80 °C. This might be due to the optimal coupling of chain mobility and crystallization driving force (i.e., degree of supercooling, as discussed in chapter 1). However, this crystallinity value is very low when compared with that typically found in fully crystallized iPP homopolymer (> 60%). This is because that the non-crystallizable hexene component significantly hinders the crystallization ability of random copolymer, which will be discussed later.

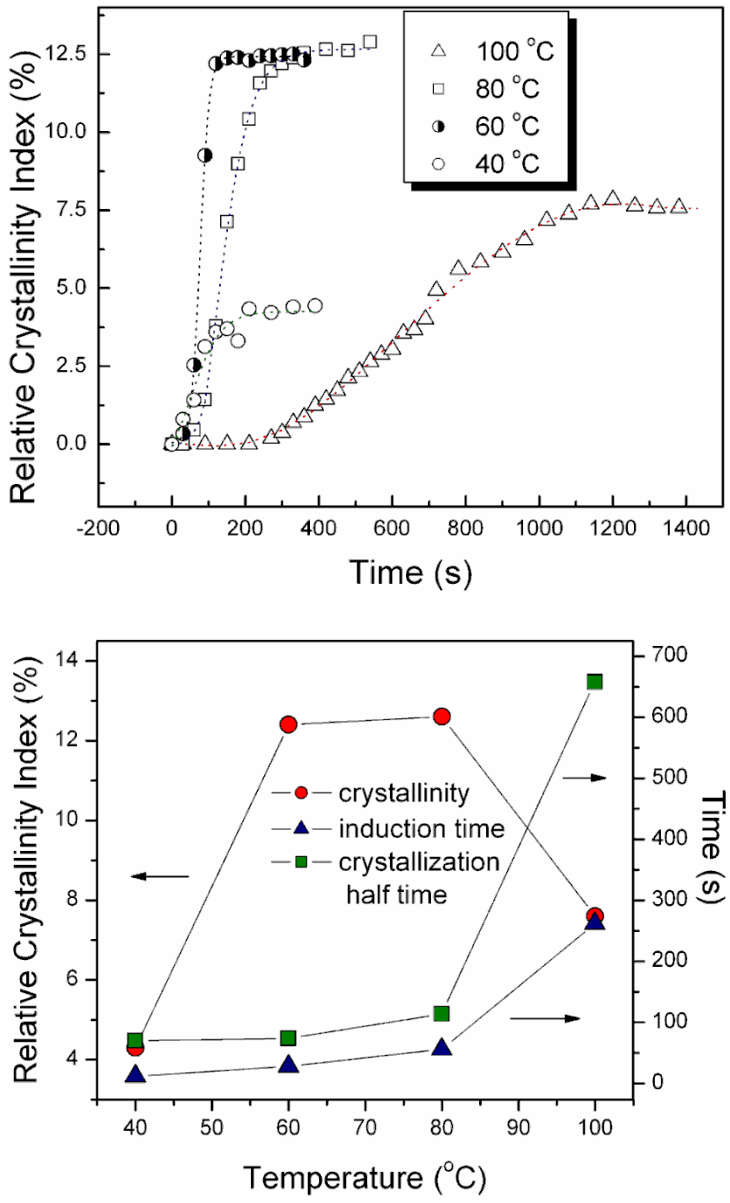

Figure 3-5. (a) Crystallinity versus time plots of samples crystallized at 100 °C, 80 °C, 60 °C and 40 °C. **(b)** Induction time and crystallization half time obtained from each curve in **(a)** at different temperatures.

3.3.2 Comparative study of crystallization at high- and low-temperature

The crystallization curves from samples crystallized at temperatures of two opposite ends, i.e., 100 °C and 40 °C are quite different, and deserve a close look. The difference in kinetics appears to be associated with the different crystalline structure. **Figure 3-6** shows the evolution of SAXS profiles of P-H copolymer annealed at 100 °C and 40 °C, respectively. It is clear that the 100 °C profiles (**Figure 3-6a**) eventually show a scattering maximum corresponding to a long

period of about 18 *nm*. The WAXS reflections at this temperature are also strong and sharp (see **Figure 3-4**). These are features of normal lamellar crystalline structure that usually developed in polymer crystallization. On the contrary, SAXS profiles at 40 ^{o}C are quite featureless (**Figure 3-6b**): intensity decreases monotonically with *s*. The lack of scattering maxima in SAXS profiles at 40 ^{o}C indicates that the scatterers formed under this condition have little or no correlation with each other. Nevertheless, the corresponding WAXS profile in **Figure 3-4** still exhibits four diffraction peaks indicating the existence of crystal structure. However, as compared with diffraction profiles of crystalline formed at 100 ^{o}C, these peaks are weak and diffuse. The crystallinity under this condition is only about 5%, as shown in **Figure 3-5**. The broad reflection peak in WAXS profile has two implications. First, the line width has a reciprocal relationship with the crystal size; a broad profile indicates a small crystal.[63] Second, it is found that the width increases with the scattering angle, which is a signature of disorder of the second kind.[77] All these results point to a distinctive morphology when P-H sample was annealed at 40 ^{o}C: crystalline regions are small blocks sparsely dispersed, with a large amount of defects imbedded.

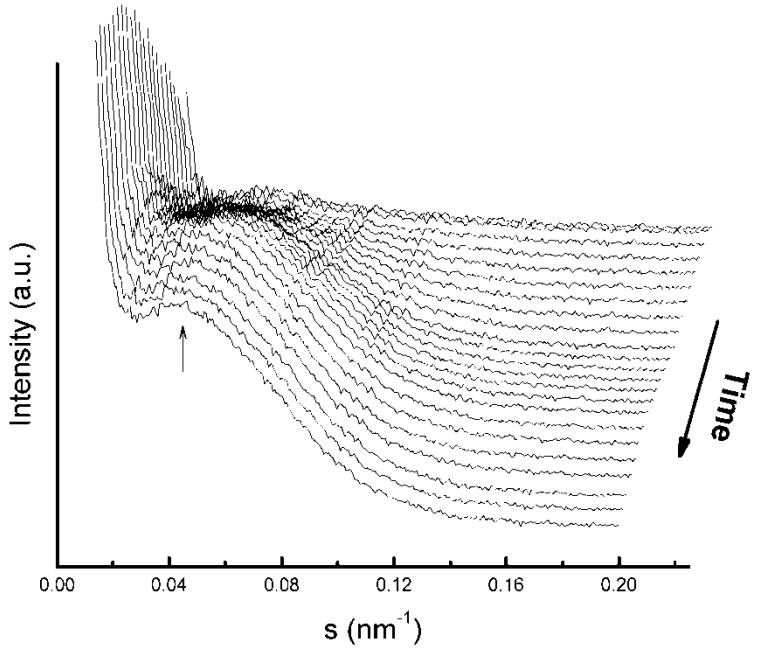

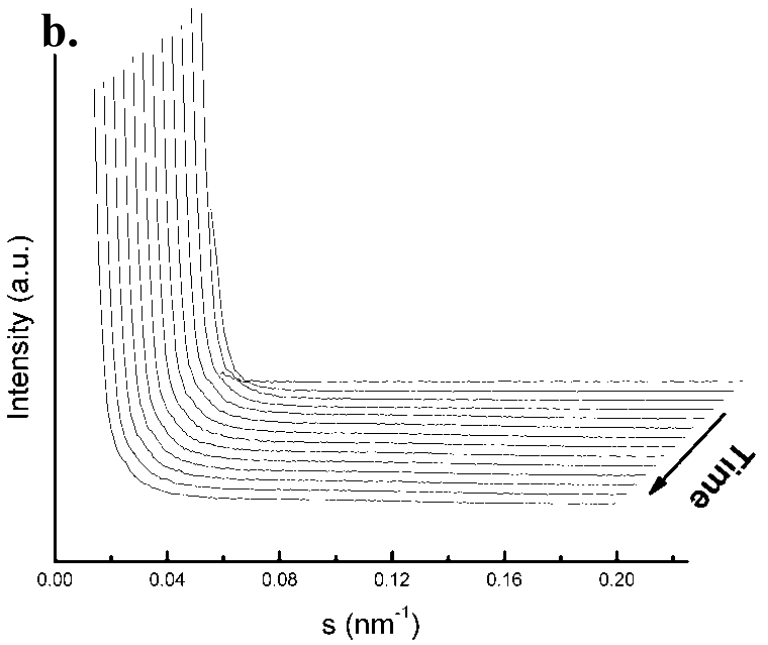

Figure 3-6. Evolutions of SAXS profiles for samples crystallized at **(a)** 100 °C and **(b)** 40 °C.

Figure 3-7 represents the comparison of scattering invariant (left y-axis) and crystallinity (right y-axis) changes as a function of time when samples were crystallized at 100 °C. The scattering invariant Q was obtained from the SAXS profile using the following expression.

$$Q = \int_0^\infty I(q) q^2 dq \qquad \textbf{(3.1)}$$

The value of Q is proportional to the mean square density fluctuations occurred in the system; this may include all phase changes leading to the inhomogeneity of the system (e.g. both crystallization and micro-phase separation will contribute to the invariant).[68] In **Figure 3-7**, it is seen that at the crystallization temperature of 100 °C, P-H copolymer experiences an induction period of about 240 *s*, within which no WAXS signal change can be detected. However, during this period, the SAXS scattering invariant continues to rise; and the SAXS profiles at the end of the induction period actually exhibit a broad shoulder indicating the existence of a weak correlation of the formed domains. But this texture must not contain any crystalline structure since there is no reflection peaks detected by WAXS in the meantime. The physical origin of the increase of scattering invariant prior to crystallization might be quite complicated. Our previous study indicated that even for iPP homopolymer, crystallization onset time derived from SAXS method appeared earlier than that from WAXS method.[90] For homopolymer, the density

fluctuation might be corresponding to the formation of certain type of precursor that triggers further crystallization. Similar results have also been reported by many other authors using different techniques such as polarized light scattering and rheological measurement.[91-93] For random copolymer, segregation between two incompatible species should also be considered. Such micro-phase separation behavior in random copolymer has been predicted by several theoretical works[44, 47, 48, 94] and computer simulations[95-97]; and it has also been experimentally verified.[98, 99] Since in our case hexene comonomer cannot be incorporated into crystal structure, the density fluctuation during the induction period could be hybridization of both processes, followed by the subsequent crystallization.

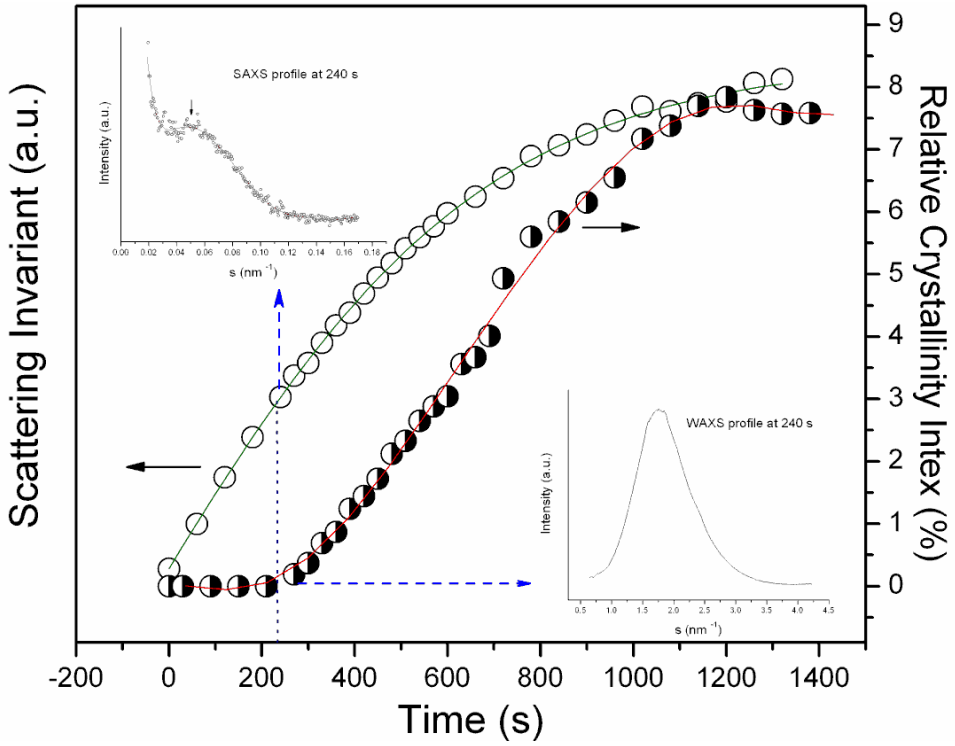

Figure 3-7. Scattering invariant (left) and relative crystallinity index (right) versus time plot when sample was met crystallized at 100 ^{o}C. The two insets exhibit SAXS and WAXS profiles at 240s, which is in the end of the induction period.

To take a close look, the time-resolved SAXS profiles (**Figure 3-6a**) are divided into two parts as shown in **Figures 3-8a** and **3-8b**. In **Figure 3-8**, all symbols represent the scattering data points, and the solid lines represent the corresponding polynomial fitted curves. In the early stage (**Figure 3-8a**), the scattering profiles are generally weak, but they do persistently exhibit a scattering peak (the first profile showing the scattering peak is at t > 90 s) at a fixed location

($s = 0.054\,nm^{-1}$), corresponding to a long period of $L = 1/s = 18.5\ nm$. After induction period, real crystallization took place and lamellar crystalline structure was formed gradually. **Figure 3-8b** shows evolution of SAXS profile during this period. It can be found that the intensity maximum moves toward low angle as crystallization proceeds, and eventually fixates at s=0.044 nm^{-1}. For homopolymer, once general shape of lamellar structure is formed, SAXS intensity maximum usually keeps unchanged during annealing. In the middle or late stage, it will even move toward large angle due to interpenetration of lamellae caused by secondary crystallization. Shifting of intensity maximum toward low angle as indicated in our experiment is probably caused by continuous exclusion of hexene segments from crystalline structure, leading to an increase of long period. This is not surprising since hexene part cannot be crystallized into crystal in our specimen. For this reason, we believe that segregation between hexene and propylene segments may be an important influential factor that contributes to the increase of scattering invariant in the early stage. Furthermore, this segment segregation process may play an important role in subsequent structure formation of crystalline, for it can be seen that the final crystalline morphology is quite different: sufficient long induction period favors classic lamellar structure while drastic quench leads to very disordered small crystal blocks.

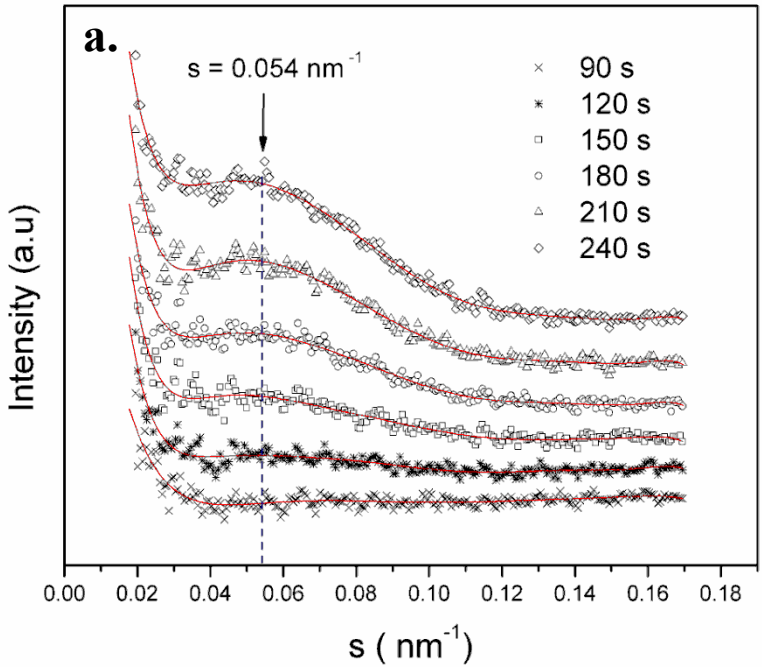

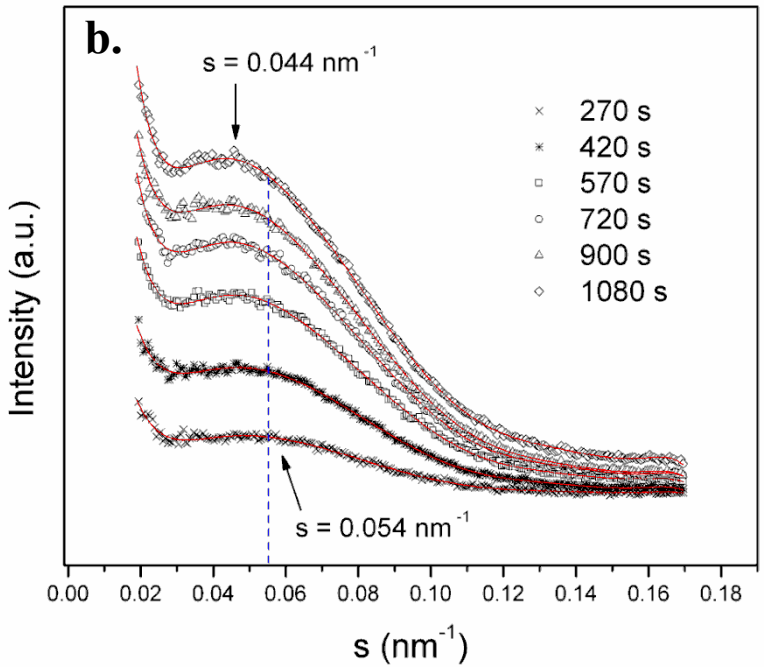

Figure 3-8. Time-resolved SAXS profiles during crystallization at 100 ^{o}C **(a)** during the induction period; **(b)** after the induction period.

In **Figure 3-8a**, the peak position remains unchanged in the induction period, but its magnitude increases with time, which is shown in **Figure 3-9**. Generally there are two mechanisms for phase separation, i.e. spinodal decomposition (SD)[100] and nucleation and growth (NG).[9] In scattering experiment, the bicontinuous interpenetrating two-phase structure results in a spinodal ring with the position of intensity maximum representing inter-domain distance. In the early stage of spinodal decomposition, the intensity maximum keeps unchanged, but the intensity increases exponentially with time, which can be described by Cahn-Hilliard linear theory. In the late stage, intensity maximum moves toward small angle and the intensity change follows the power law due to the phase coarsening.[101, 102] NG theory predicts a consistent intensity increase following power law.[101, 103] In our study, it is difficult to conclude which one better fit the segregation process because the scattering intensity in the early stage is too weak for detailed analysis. In **Figure 3-9**, it is hard to judge whether the relationship of peak intensity and time can be described by exponential or power function. Trustworthy analysis of the early stage density fluctuation process must rely on a well-chosen model system which shall give good phase contrast between segregated domains. Furthermore, crystallization temperature must be carefully chosen so that the induction time is long enough to generate sufficient data points. At the final stage of crystallization, the peak fixates at the position of $s = 0.044\ nm^{-1}$, corresponding to a long

period of 22.7 *nm*. Lamellar thickness can be estimated via ideal two-phase model. In this case, long period represents the total length of periodicity with combined crystalline and amorphous layers, and lamellar thickness can be calculated by multiplying the long period with crystalline fraction (i.e., 7.8 % as shown in **Figure 3-5**), which leads to a value of 17.7 Å. Even though the two-phase model may underestimate the lamellar thickness because of possible existence of transition layer, and because of the existence of lamellar clusters such as spherulites, this value is still very small as compared with the typical lamellar thickness of iPP homopolymer which usually locates in the range of 100 Å. Some recent studies[50-53, 104] reported the existence of thin lamellar structure because of the lower melting temperature in random ethylene-based copolymer system, which is consistent with our findings.

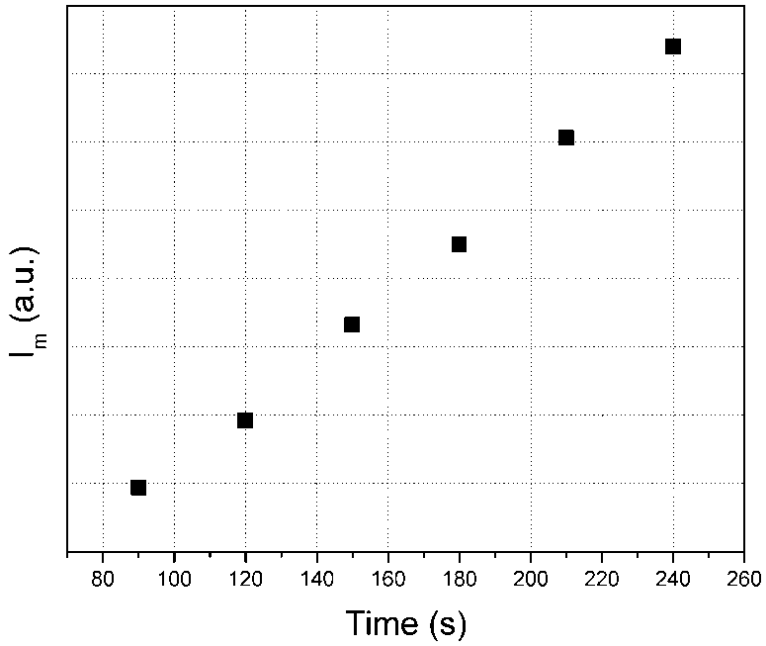

Figure 3-9. Change of peak intensity as a function of time during the early stage of crystallization at 100 ^{o}C.

Figure 3-10 illustrates the comparison of crystallinity (from WAXS) and invariant (from SAXS) for crystallization at 40 ^{o}C. Under this condition, due to the large degree of supercooling, crystallization kinetics was greatly enhanced. The scattering invariant and crystallinity increase with time in pace. The diffraction peaks was observed in WAXS profiles at the very beginning of the crystallization; and patterns was fixed after 200 *s*. In-sets in **Figure 3-10** show the scattering profiles of SAXS and WAXS after crystallization was accomplished. As discussed earlier, since reflection peaks in WAXS profile are very weak and diffuse, their positions can only be roughly

assigned to α-form crystal (see **Figure 3-4**). Monotonically-decreased SAXS profile indicates that those small crystal blocks in the system scatter independently, i.e., they are sparsely dispersed in the amorphous matrix.

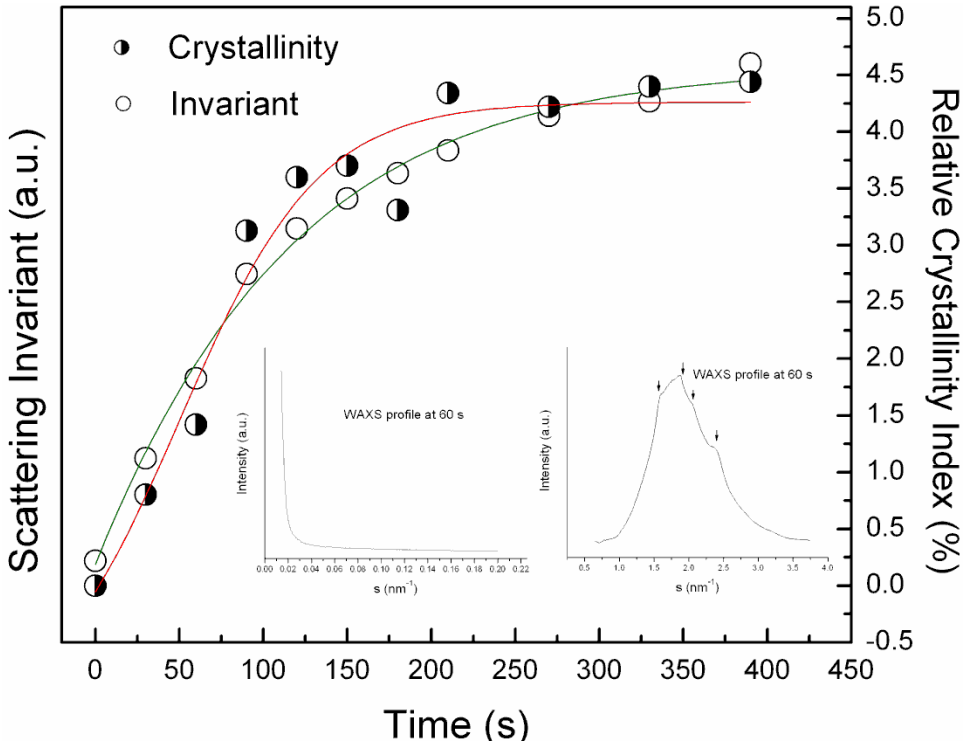

Figure 3-10. Scattering invariant (left) and relative crystallinity index (right) versus time plot when sample was crystallized at 40 °C. The two insets exhibit SAXS and WAXS profiles at the very beginning of the crystallization process.

Dimension of the crystal block can be estimated by using the Guinier's method[68, 69] which correlates the scattering intensity with radius gyration of aggregate in dilute solution at low angles, as expressed is **Eq. (3.2)**,

$$I_s = I_0 \exp(-\frac{R_g^2 q^2}{3}) \qquad \textbf{(3.2)}$$

where I_s is the scattering intensity and I_0 is intensity of incident light. R_g is the radius of gyration; q is the wave vector which has the same physical meaning as s ($q = 2\pi \cdot s$). By apply logarithmic operation on both sides, **Eq. (3.2)** can be rewritten as

$$\ln(I_s) = \ln I_0 - \frac{R_g^2}{3} q^2 \qquad \textbf{(3.3)}$$

Plotting $\ln(I_s)$ against q^2 or s^2 leads to a straight line and the radius of gyration can be obtained from its slope. **Figure 3-11** shows a series of Guinier plots obtained at different times and crystallization temperature of 40 ^{o}C based on **Eq.(3.3)**.

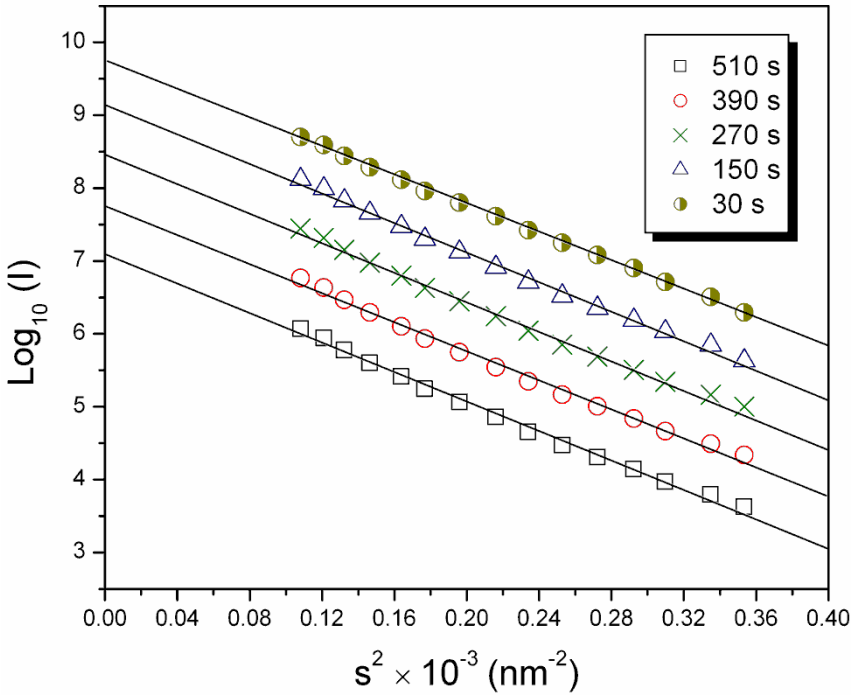

Figure 3-11. Guinier plots obtained from SAXS profiles of sample crystallized at 40 ^{o}C.

The radius of gyration calculated from all the Guinier plots fluctuate around 27.5 nm, which remains almost unchanged during crystallization (as shown in **Figure 3-12**). The dimension of small crystal block at 40 ^{o}C and that of lamellar crystalline structure at 100 ^{o}C are in the same order of magnitude. At this temperature, crystal blocks were quickly developed into this dimension due to large driving force. The quickly-formed crystals could hardly grow further and become more perfect because of low chain mobility. These blocks are highly disordered and therefore not stable, which can be seen by comparing the melting behavior of both crystallites formed at 40 ^{o}C and 100 ^{o}C. This experiment was carried out by gradually melting (4 ^{o}C/min) the fully crystallized sample after isothermal crystallization.

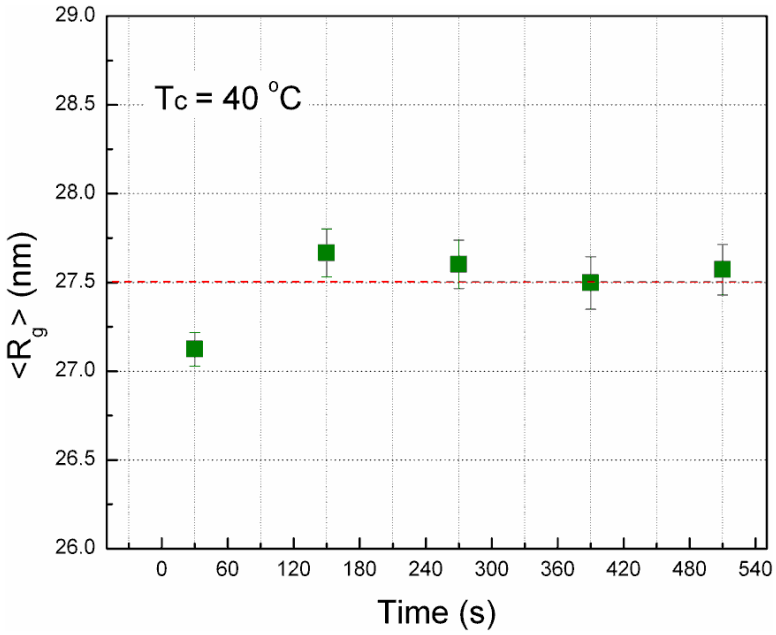

Figure 3-12. Radius of gyration (obtained from Guinier's plot) change as a function of time (crystallization temperature was 40 °C).

The changes of crystallinity derived by *in-situ* WAXS experiments under both conditions are illustrated in **Figure 3-13**. The hollow circles represent the crystallinity change during heating of sample fully crystallized at 40 °C. The initial crystallinity, as was shown earlier, is 4.8 % and it remains unchanged until at temperature around 60 °C, indicating that the chains at these low temperatures are still not sufficiently mobile. From 60 °C to 100 °C the crystallinity increases notably due to recrystallization process. After this period, the crystallinity begins to decrease until the sample becomes completely molten. The heating process of sample crystallized at 100 °C is displayed as hollow squares, where the crystallinity increases very slightly then begins to decrease with the increasing temperature. Above 118.2 °C (point **c**), the crystallinity of samples crystallized at two different temperatures merges into a same trend, as represented by the solid line. The extrapolated nominal melting point in **Figure 3-13** is 140 °C. By intercepting the solid line with the initial stage of melting (i.e., the horizontal dotted line), melting point for samples crystallized at different temperature can be determined: melting point **a** at 108.4 °C for the sample crystallized at 40 °C, and melting point **b** at 114.8 °C for the sample crystallized at 100 °C. The difference of 6.4 °C indicates the less stable crystalline structure formed at the lower crystallization temperature, which is consistent with the results from the structure analysis made earlier. In **Figure 3-13**, the crystallinity change from point **c** to zero is 7.1 %, whereas the crystallinity increase during heating from 40 °C to 100 °C is 5.4 % which is

smaller. This indicates that during heating, part of the crystals can be melted and recrystallized into more stable lamellar crystals.

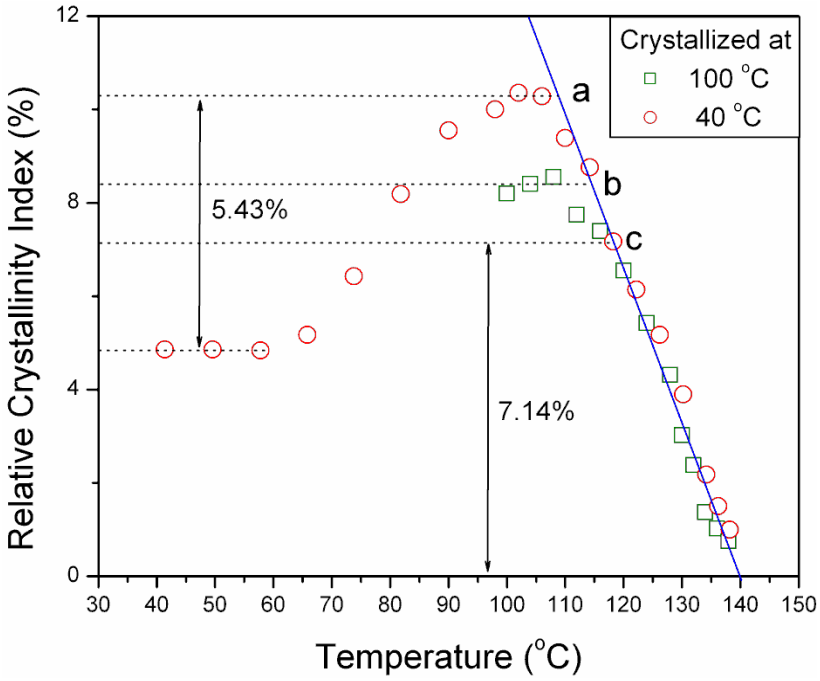

Figure 3-13. The crystallinity change during heating (at a heating rate of 4 °C/min) of fully crystallized samples at 100 °C (□) and at 40 °C (○).

At this point, it can be concluded that the morphology of random copolymer crystallites is kinetically controlled. The process of segmental segregation plays an important role in the subsequent growth and perfection of crystallites. With the assistance of such a pre-ordering process, the lamellar structure formation is favored at high temperatures. While at low temperatures, the crystallization rate is greatly enhanced. However, once parts of iPP crystallizable segments are segregated from the amorphous matrix, driven by the large degree of supercooling, they are rapidly crystallized into a less ordered structure, where the formed crystallites become small blocks with no correlation with each other.

3.4 Summary

The crystallization and melting behavior of P-H copolymer by was investigated by using time-resolved SAXS/WAXS technique. Some relevant correlations between the crystal superstructure and crystallization kinetics can be made as follows.

1. The P-H random copolymer with 5.7 % mole fraction of hexene content can only form α-phase crystal of iPP homopolymer. The hexene component cannot be incorporated into the unit cell under this concentration.

2. The kinetics of crystallization varies with temperature, and it plays an important role in later structure formation of crystalline. At high temperature (100 ^{o}C), the system exhibits a long induction period, during which segmental segregation between propylene and hexene component (often termed as liquid-liquid phase separation) takes place. This segregation can serve as a pre-ordering process, and lead to the formation of thermally stable lamellar crystal structure. At low temperature (40 ^{o}C), the propylene component is rapidly crystallized from the matrix and frozen into small crystal blocks due to the low chain mobility and large crystallization driving force (supercooling).

3. The heating experiments confirmed that the crystallites formed at 40 ^{o}C are less stable. During heating, part of crystal blocks can be melted and recrystallized into more thermally stable lamellar crystals.

4 Shear-Induced Crystallization

4.1 Introduction

Another type of propylene-based copolymer, propylene-1-butene random copolymer (P-B) with low content of comonomer butene is selected as a model system to study shear-induced crystallization behavior for random copolymer. With low concentration of non-crystallizable comonomer, no new crystal form can be formed. In the last chapter, it has been shown that P-H copolymer with low hexene content crystallizes into α-form crystal of iPP homopolymer. α-form is the most common modification of iPP. However, as will be shown later, a small amount of butene is able to change the preference of forming α-form crystal of iPP under conditions of both quiescent and shear-induced crystallization.

Regardless of polymorphism, there are several aspects that shear can influence the polymer crystallization. In dilute polymer solution, a shear flow can generate coil-to-stretch transition if the shear rate exceeds a critical value. This transition is sharp, and an entire chain is able to be extended. In polymer melt, a full extension of a single chain is difficult to achieve, as polymers in bulk are entangled with each other. However, shear is able to stretch and orient chain segments in localized regions. This orientation lowers the nucleation barrier, as described in chapter 1. Furthermore, it creates surfaces for subsequent crystal growth. Therefore, the entire crystallization kinetics will be greatly enhanced, which will be discussed in relevant parts in this chapter.

In scattering experiment, scattering patterns of semi-crystalline polymer being sheared or stretched (stretching experiment will be discussed in later chapters) are anisotropic. This indicates that an advanced data analysis must be based on the whole-pattern. This is of particular importance if the system shows polymorphism, as it is possible to distinguish different modifications by identifying orientation of different diffraction peaks, which is much more trustworthy as compared to 1D scattering profile analysis. An example is given in **Figure 4-1** which shows WAXS patterns of P-B copolymer crystallized quiescently (**Figure 4-1a**) and after

a step shear (**Figure 4-1b**). The shear direction is vertical; other details are not important at this moment, and will be described in the following section.

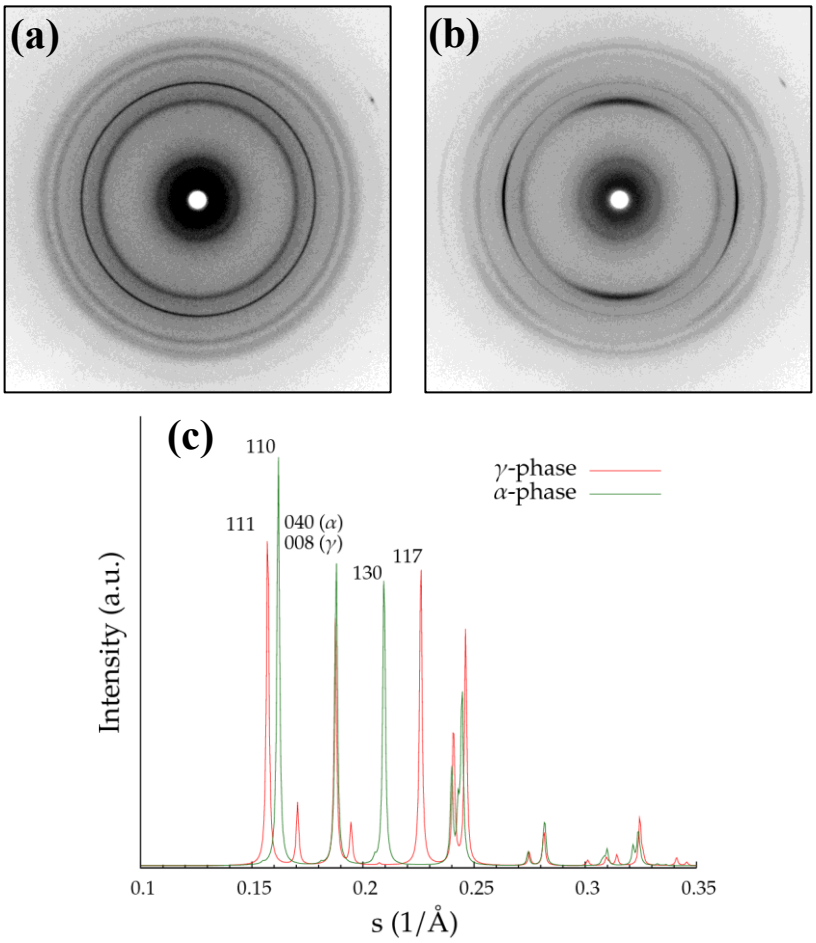

Figure 4-1. Powder diffraction pattern of P-B random copolymer crystallizaed at 100 ^{o}C **(a)**; Fiber diffraction pattern of the sample sample crystallized at 100 ^{o}C after a step-shear with the shear rate being 100 s^{-1}, for 3 s **(b)**; and calculated powder diffraction scattering profiles of α- and γ-form crystals.

It will be shown later that this system consists of both α- and γ-phase of iPP homopolymer. Since these two phases have close packing energy within the unit cells, the reflection peaks in 1D scattering profile are close to each other (see in **Figure 4-1c** the theoretical powder diffraction profiles of α- and γ-phase). In practice, reflection peaks will be broadened due to finite size (also possible to be due to the disorder of the second kind at large angle[63]), which makes profiles from two modifications largely overlapped. In this case, powder diffraction pattern (**Figure 4-1a)** cannot provide extra information, but anisotropic diffraction

pattern due to orientation as shown in **Figure 4-1b** can unambiguously identify each phase and its orientation mode. For example, the strong diffraction arc on the equator in **Figure 4-1b** clearly indicates that the *c*-axis of the γ-phase lies horizontally (details will be given later).

In this chapter, 2D whole-pattern analysis will be performed for crystallization of P-B random copolymer induced by a step-shear. Useful information such as polymorphism, preferred orientation, and crystal disorder can be generated unambiguously.by using this approach. The results will give more insights into the crystallization mechanism of random copolymer.

4.2 Practical considerations for 2D WAXS whole-pattern analysis

4.2.1 Calculation details

As introduced in chapter 2, the first task for 2D WAXS pattern simulation is to calculate the powder diffraction intensities for all (*hkl*) planes. To use **Eq.(2.9)**, coordinates of atomic groups in one unit cell are needed. The asymmetric unit of all three crystal forms of iPP consists of 9 carbon atoms, corresponding to one 3_1 helix. The asymmetric units for α- and γ-phase were directly adopted from original publications of Natta and Corradini,[88] and of Brückner[83]. The complete set of coordinates are generated using *C2/c* and *Fddd* space groups for α- and γ-phase, respectively. Due to the nature of copolymer, the dimensions of the unit cells are not exactly equal to the reported values. α-form possess a monoclinic unit cell with the cell parameters being a = 6.70 Å, b=21.76 Å, c=6.83 Å, β =99.3°. γ-form's unit cell is orthorhombic with a = 8.54 Å, b = 9.93 Å and c = 43.37 Å. The absolute value of scattering vector s for a given (*hkl*) is determined by cell parameters, and the formula is written in **Eq.(4.1)** and **(4.2)** for monoclinic and orthorhombic unit cell, respectively.[105]

$$s = \sqrt{\frac{h^2}{a^2 \sin^2\beta} + \frac{k^2}{b^2} + \frac{l^2}{c^2 \sin^2\beta} - \frac{2hl\cos\beta}{ac\sin^2\beta}} \qquad \textbf{(4.1)}$$

$$s = \sqrt{\frac{h^2}{a^2} + \frac{k^2}{b^2} + \frac{l^2}{c^2}} \qquad \textbf{(4.2)}$$

Once powder intensities of each (*hkl*) were obtained, **Eq.(2.12)** was then used to calculate the fiber-averaged intensity. Onsager ODF (**Eq.(2.17)**) was adopted to produce polar distribution of intensity (other possibilities will be discussed later, Onsager ODF is the simplest one to use); and the transformation kernel $F(\phi,\phi_{hkl})$ was given in **Eq.(2.18)**. The line-broadening in $I(s)\sim s$ profile was modeled by using Lorentzian function, characterized by a single parameter, the integral width w_c. $1/w_c$ directly gives the size of the crystal, which is essentially equivalent to the size obtained by using Scherrer's equation.[63] Three Gaussian distributions were used to model the amorphous halo.

4.2.2 Goodness-of-fit

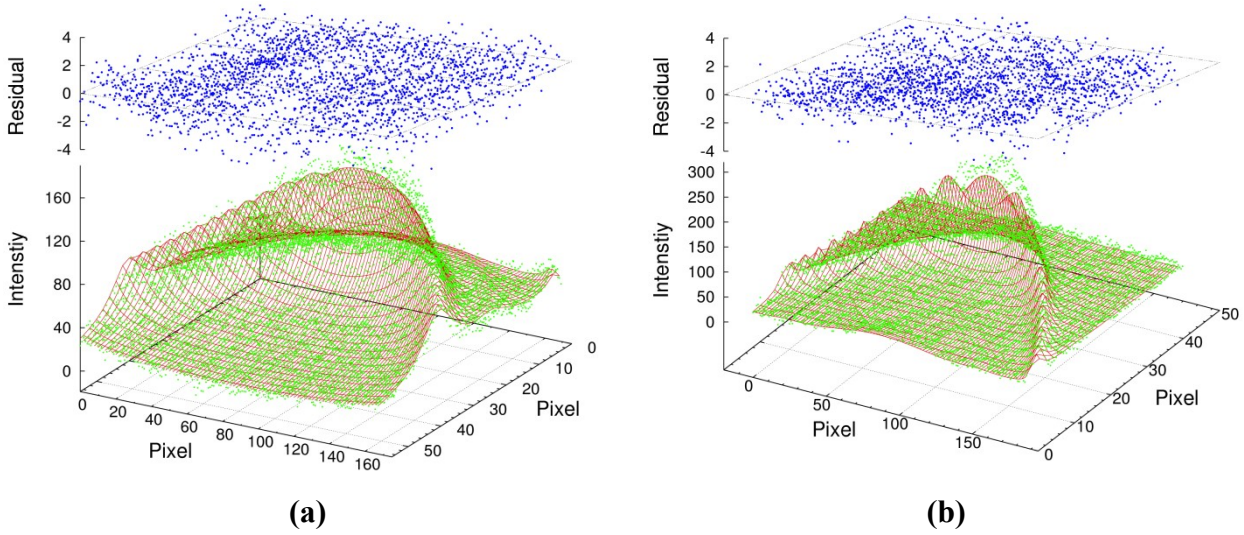

(a) **(b)**

Figure 4-2. Examples of experimental (dot) and simulated intensity (mesh) of the diffraction arcs peaked at s=0.156 Å^{-1} **(a)** and at s=0.184 Å^{-1} **(b)** of P-B random copolymer. The two arcs are corresponding to $(111)\gamma$ **(a)** and a superposition of $(040)\alpha$ and $(008)\gamma$ **(b)**. The detail of polymorphism is discussed in the context. Residual was defined as $(X_{\exp}-X_{\sin})/\sigma$, with $X_{\exp}$ and $X_{\sin}$ being the intensities from the experimental data and simulation, respectively, and σ being the standard deviation obtained from the Poisson distribution according to photon counting statistics.

Simulated pattern was registered on a 256×256 lattice and was compared with the experimental pattern. Data fitting was performed on the trial-and-error base, as a nonlinear fitting for a 256×256 data set is not feasible with current computation power available. 1D profiles

($I(s) \sim s$ plot) from experimental and simulated data were compared first to judge if peak positions are matched well. To further check the goodness-of-fit, the main diffraction peaks from experimental and simulated results were examined with the χ^2 analysis. **Figure 4-2** shows the fitting of (008) and (111) peaks of the γ-phase as an example. The fitting residual was defined as $(X_{exp} - X_{sim})/\sigma$, where X_{exp} and X_{sim} are the intensities from the experimental data and simulation, respectively; σ is the standard deviation obtained from the Poisson distribution according to photon counting statistics. χ^2 per degree of freedom should be as close to one as possible.

4.3 Experimental

4.3.1 Materials and sample preparation

The P-B random copolymer was provided by ExxonMobil Chemical Company. The number average molecular weight M_n of the sample was 56,000 g/mol and the polydispersity was 1.97. The mole fraction of the butylene component was 5.7%. The DSC heating experiment showed a melting peak at 122 ^oC. The ring-like sample was obtained by first melting and compressing the bulk polymer in a 1.0 mm thick mold, and then naturally cooling down to the room temperature. The film was then cut into ring-shape to fit the shear stage.

4.3.2 Shear-induced crystallization experiment

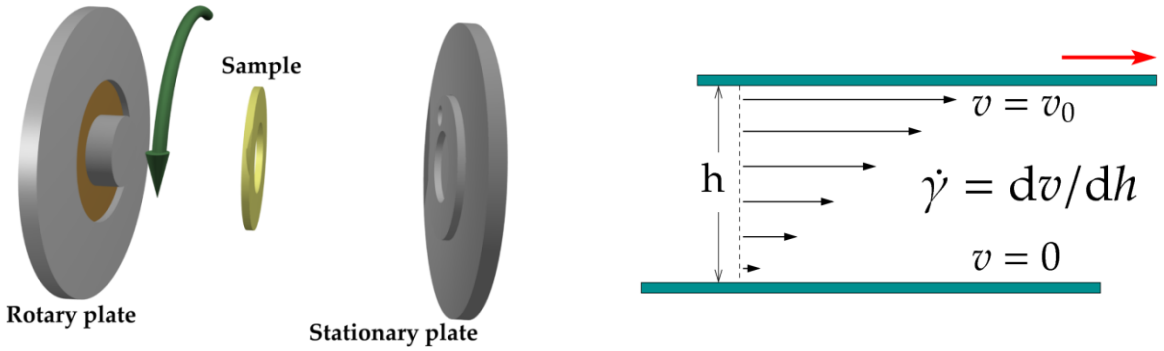

Figure 4.3. Schematic of parallel plate shear mechanism **(a)**; and pictorial illustration of the definition of shear flow **(b)**.

A Linkam CSS-450 high-temperature shearing stage modified for *in-situ* WAXS measurement was used to precisely control temperature and shear field. **Figure 4.3a** illustrates the scheme of parallel plate geometry for producing shear flow. It is composed of a rotary plate and a stationary plate. The stationary plate is fixed, with a hole near the edge to let X-ray passes through. A piece of Kapton film is embedded in the rotary plate, so that X-ray can always pass through it during rotation. The rotation of the rotary plate produces the shear field as illustrated in **Figure 4.3b**. The strength of the shear is characterized by the shear rate, which is equal to $\mathrm{d}v/\mathrm{d}h$, with v and h being the velocity of translation motion of the upper moving plate (in rotary shear geometry, this is equal to the rotation motion, as shear is applied in the tangential direction of the rotation). Shear direction is vertical for data shown in this chapter. Detailed information of shear apparatus could be found in our previous publication.[81] Shear rate varied in radial direction in the parallel plate shear geometry. The point directly exposure to X-ray was fixed and calculated shear rate was the value at that measuring point all along our experiments.[81] The stress field also had a gradient along this direction due to the nature of shear flow, which will be discussed in the relevant places in the context.

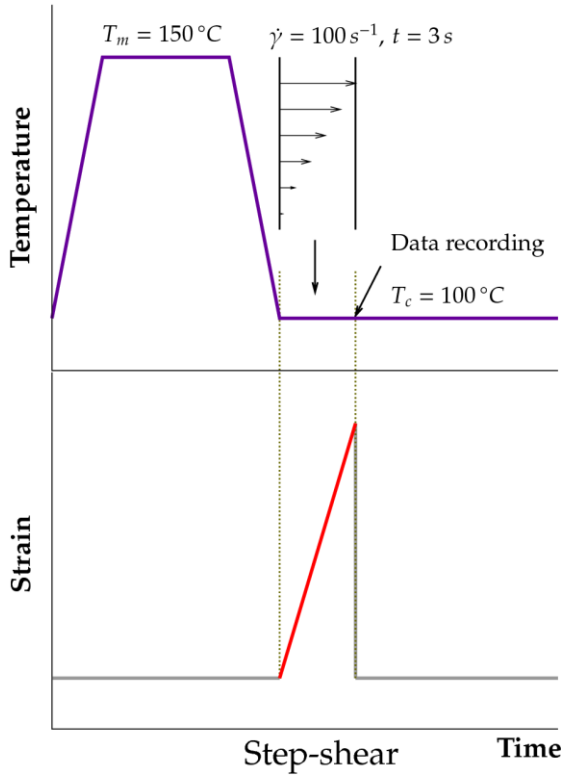

Figure 4-4. Schematic of the experimental protocol.

The chosen experimental procedure was as follows. First, the sample was melted and kept at 150 ^{o}C (30 ^{o}C above peak position of endothermic peak DSC heating test) for 5 *min*. After that, it was cooled down to the crystallization temperature, 100 ^{o}C with a cooling rate of -30 ^{o}C/min. Immediately after the sample reached 100 ^{o}C, a step shear was applied. The shear rate was 100 s^{-1} and shear duration was 3s. The isothermal crystallization process of the sample at this temperature was recorded on-line by WAXS and SAXS. Since our shear rate was relatively high, sample condition was checked after each experiment. The shape of samples was well kept. No fracture was observed at this shear condition. The exposure time for each image collection was 30 *s*. The sample-to-detector distance was 121 *mm*. A schematic of the experimental protocol is shown in **Figure 4.4**.

4.4 Polymorphism and orientation modes

A preliminary analysis starts from noticing the diffraction peak at s=0.223 Å^{-1}, which is the signature of the existence of γ-modification, and can be assigned to $(117)_\gamma$. Then the first arc near the meridian (s=0.156 Å^{-1}) and the second arc in the equator (s=0.184 Å^{-1}) should be indexed as $(111)_\gamma$ and $(008)_\gamma$, respectively. Since the $(008)_\gamma$ arc locates at the equator, the *c*-axis of the γ-phase must orients horizontally. This initial judgment generates several possibilities of orientation modes of the γ-phase, as shown in **Figure 4-5**.

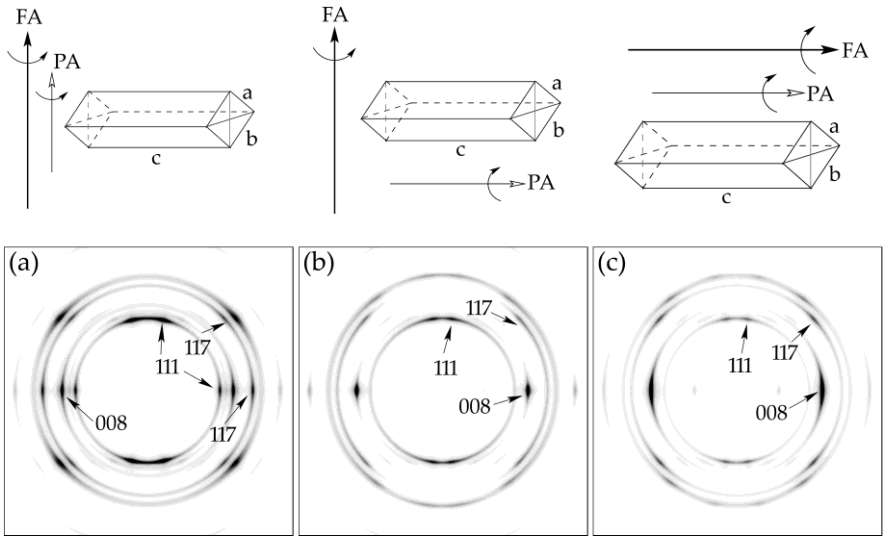

Figure 4-5. Orientation modes and their corresponding fiber diffraction patterns of γ-phase iPP. **(a)-(c)** represent diagonal orientation, perpendicular orientation and cross-β configuration, respectively. Detailed description can be found in the context.

In **Figure 4-5**, FA and PA refers to the fiber axis and the principal axis of rotation, respectively, as defined in chapter 2. The second row shows the fiber diffraction patterns corresponding to structures in the first row. The fiber diffraction pattern was generated using Poisson kernel which is feasible for both parallel and perpendicular orientation. As can be seen that Poisson kernel produces a very long tail, thus it is not realistic for quantitatively analysis. However, the purpose of **Figure 4-5** is to qualitatively compare the simulated patterns with experimental ones such as shown in **Figure 4-1b**, in order to decide the orientation mode which will be the starting point for the further quantitative analysis, thus Poisson kernel offers a convenient way to treat both orientation modes.

Figure 4-5a and **4-5c** represent two parallel orientation modes, since PA is in consistent with FA. The difference is that in **Figure 4-5a**, both FA and PA are vertical and the diagonal of *ab*-plane (chain direction) is in parallel to them. This was termed as 'parallel orientation' by de Rosa[58] (the detail of this orientation mode will be discussed in detail in chapter 5). The term stems from the fact that polymer chains in this case intend to be in parallel to the FA to the largest degree (half of the 8 chains are in parallel to the FA and the other half has an 80 ^{o} angle with respect to it, due to the nature of cross-hatching). Thus it actually refers to the parallel chain packing (with respect to the FA). To avoid confusion with our previously defined parallel orientation which means that FA and PA are in parallel to each other, we term it as 'diagonal orientation'. In **Figure 4-5c**, FA, PA and the *c*-axis of the γ-phase unit cell are all parallel, which is essentially equivalent to the so-called 'cross-β configuration'.[58] This orientation mode is frequently met in stretching experiment, with the *c*-axis of the γ-phase unit cell being in parallel to the stretching direction (FA). **Figure 4-5b** represents the perpendicular orientation, with the *c*-axis of the γ-phase unit cell being in parallel to the PA but perpendicular to the FA. All these three modes are able to produce $(008)_{\gamma}$ arc in the horizontal direction and $(111)_{\gamma}$ near the vertical direction.

The 'cross-β configuration' (**Figure 4-5c**) will be used for later quantitative analysis for the following reasons. First, the strongest diffraction arc is $(008)_{\gamma}$. Second, it is found that the $(008)_{\gamma}$ arc is relatively broad, as compared to that in other orientation modes. These findings are in consistent with the fiber diffraction pattern of P-B copolymer shown in **Figure 4-1b**.

Perpendicular orientation has a signature that all $(11l)$ arcs appear at both off-axis position and the equator. The off-axis arcs are natural because the ϕ_{hkl} for a $(11l)$ plane is nonzero. The equatorial arcs are due to the multiplicity, or to change a word, are originated from $(\bar{1},1,l)$, $(1,\bar{1},l)$, $(\bar{1},1,\bar{l})$ and $(1,\bar{1},\bar{l})$. These equatorial arcs, including (111) and (117) are not distinguishable in the experimental pattern. All arcs' positions in **Figure 4-5b** are also consistent with experimental observation. However, as explained before, **Figure 4-5c** presents nicer arc shapes. It has been pointed out in chapter 2 that shear flow is complex as compared with uniaxial stretching. Thus, it is possible that all these orientation modes appear in reality. We select the parallel 'cross-β configuration' as shown in **Figure 4-5c** as a first approximation, and it will be shown later, this model fit experimental data quite well.

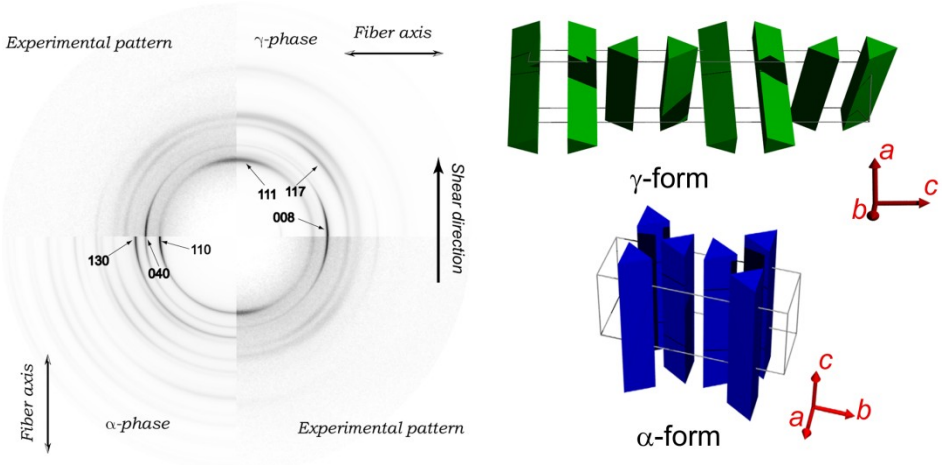

Figure 4-6. 2D WAXS patterns of experimental data (upper-left and lower-right corners), simulated γ-form (upper-right corner) and simulated α-form (lower-left corner) crystals. The experimental pattern was gathered 960 *s* after the step-shear when the crystallization process was complete. The flow direction was vertical; the fiber directions of γ-phase and α-phase were set to be horizontal and vertical, respectively. Cartoon illustrations of orientation of γ- and α-phase are shown on the right.

Figure 4-6 shows a comparison of experimental WAXS pattern (at 960 *s* when crystallization is fully completed) and calculated fiber diffraction patterns of both α- and γ-phase. In **Figure 4-6**, shear direction is vertical. The experimental patterns are shown in upper left and lower right corners, with air background being subtracted. Pattern of the γ-phase with cross-β configuration is shown in the upper right corner. Diffraction pattern of the α-phase having a parallel orientation with the *c*-axis aligned to the fiber axis (vertical) is shown in the

lower left corner. It is evidenced that γ-phase pattern fit the experimental data much better. Following the convention,[81, 106] we term the orientation mode for the α-phase as *c*-axis orientation which is featured by three equatorial arcs representing (110)α, (040)α and (130)α, respectively (assuming the fiber axis is vertical). The *c*-axis orientation is one of the major orientation modes for the α-phase; the details of both conditions will be discussed in chapter 5, as they are not important in this study. It also needs to be pointed out that the reflection of (111) plane in the γ-phase seems to be appeared in the vertical direction. In fact, this is not the case and can be explained as follows. The polar angle ϕ_{hkl} of the (111) plane is 81.5 ^{o} (the horizontal direction is zero degree), which is very close to the vertical direction. Because of its broad polar distribution, the (111) reflection plane appears to be one arc in this direction, although it actually consists of two arcs centered at 81.5^{o} and 98.5^{o}, respectively.

As has been shown in **Figure 4-5**, three orientation modes may account for the fact that the *c*-axis of the γ-phase unit cell orients horizontally. Modes in **Figure 4-5a** has been observed before, when iPP was processed by injection molding,[107] as well as stretched uniaxially at very small strains.[108] Fiber diffraction pattern in **Figure 4-5b** is theoretically possible but not experimentally observed before. Our calculation based on **Figure 4-5c** fits the experimental data, which is reasonable, since in this case the nature of the shear flow needs to be considered. Shear is a weak flow, as compared to uniaxial stretching (extensional flow). Furthermore, its deformation tensor can be decomposed into rate-of-strain tensor and vorticity tensor, denoted as *2D* and *2W*, respectively.[109]

$$2D = \begin{vmatrix} 0 & \dot{\gamma} & 0 \\ \dot{\gamma} & 0 & 0 \\ 0 & 0 & 0 \end{vmatrix};\ 2W = \begin{vmatrix} 0 & \dot{\gamma} & 0 \\ -\dot{\gamma} & 0 & 0 \\ 0 & 0 & 0 \end{vmatrix} \qquad \textbf{(4.3)}$$

As seen from **Eq.(4.3)**, in the rate-of-strain tensor, two off-diagonal components are equal, which is responsible to the motion of uniaxial stretching. While the same components in the vorticity tensor are equal in magnitude but have opposite signs, indicating the rotational motion. The rotational flow might take an important role in the formation of perpendicular orientation of the *c*-axis with respect to the flow direction. Similar result was also reported in carbon nanotube-polymer composite under shear. For example, Ezquerra et. al.[110, 111] tested

poly(butylene terephthalate) (PBT)/carbon nanotube nanocomposite with rheo-SAXS measurement. A unique orientation of PBT lamellar crystals growing in parallel to shear direction was observed after applying a step shear at crystallization temperature. Shear was able to rotate carbon nanotube and small crystals grown at early stage to 90° with respect to the flow direction, and therefore induced the growth of lamellar crystals in parallel to the flow direction.

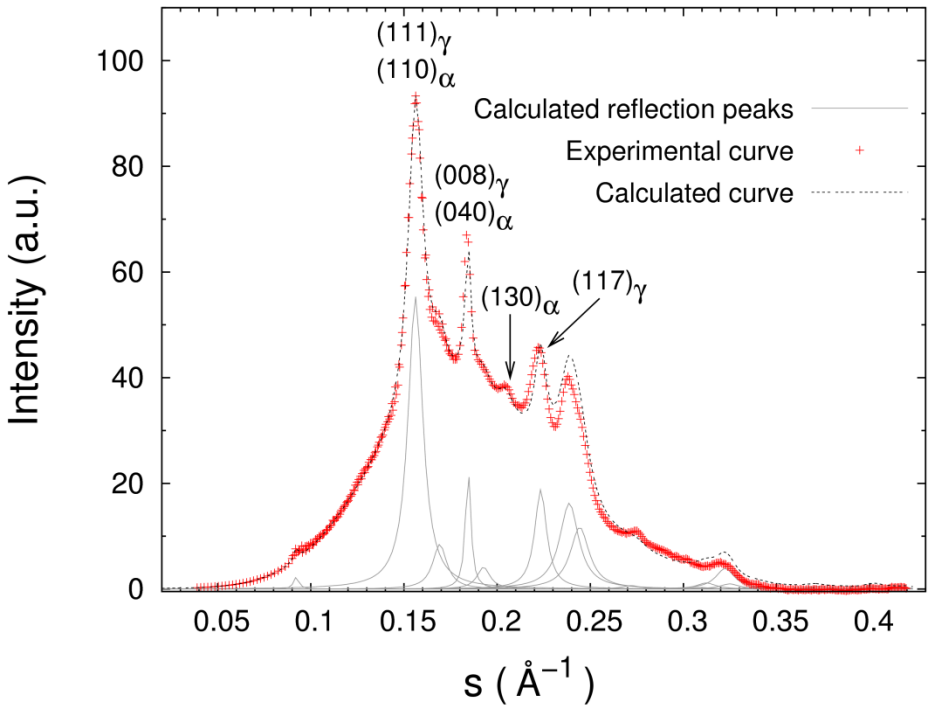

Figure 4-7. 1D integrated intensity profile from experimental data (cross point) and simulation (dashed line), where 20% of α-phase was added in the simulation. Calculated reflection peaks from the γ-phase iPP is shown below the overall profile.

Although the dominant polymorph in the chosen system is γ-form crystal, there is evidence indicating the existence of a small amount of α-form crystal, which can be analyzed according to **Figure 4-7** which shows the 1D integrated intensity profile comparing experimental data (cross data point) and simulated result (dashed line) which consists of 20 wt% of α-form and 80 wt% of γ-form crystals. The intensity integration scheme is as follows:

$$I(s) = \int_0^{\pi/2} I(s,\phi)\sin\phi \mathrm{d}\phi \qquad \textbf{(4.4)}$$

The contribution of α-form crystal was included because it was found that there was a small reflection peak appearing at s = 0.205 Å^{-1}. This peak was absent from calculated reflections of

the γ-form crystal, but can be indexed as one of the characteristics peaks of the α-phase, namely, $(130)_\alpha$ (see detail in **Figure 4-1c**).

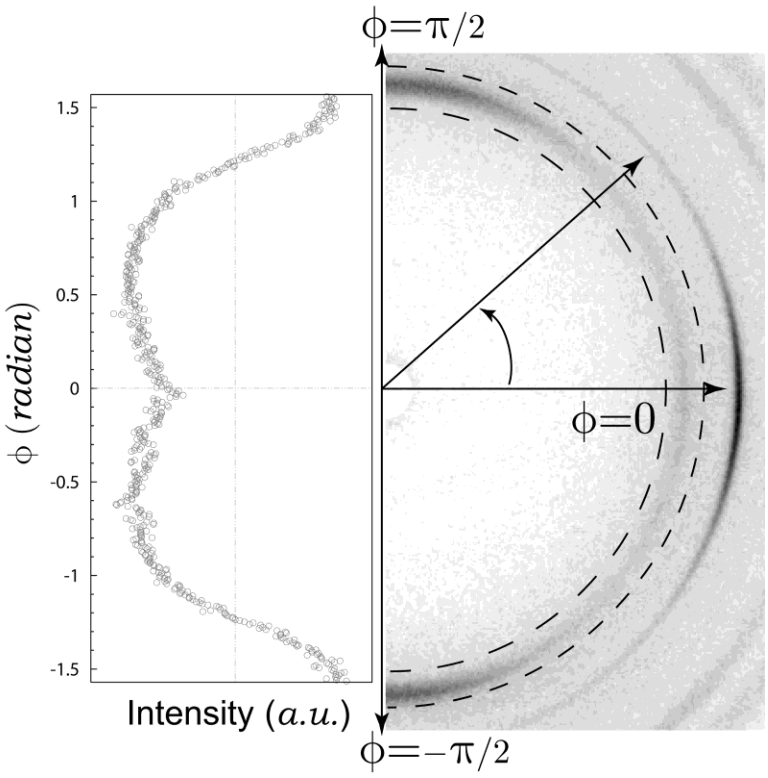

Figure 4-8. Polar intensity scan of reflections from (111) plane of γ-phase (close to vertical direction) and (110) plane of α-phase (in horizontal direction).

As described earlier, polymer chains in the α-form crystal are in parallel to the *c*-axis. When external force is applied, the *c*-axis is intended to align along the force field. Although our P-B copolymer is dominant by the γ-form crystal under shear, the orientation geometry of a small amount of α-form crystal can still be identified. **Figure 4-8** shows the polar intensity scan of reflections from (*hkl*) planes at $s = 0.157$ Å^{-1}, i.e., (111) plane of the γ-phase or (110) plane of the α-phase. Since the arcs close to the vertical direction have been indexed as (111) plane of γ-phase, the intensity maxima in the horizontal direction (although very weak, it is still distinguishable) must be due to (110) plane of α-phase. This indicates that α-form crystal adopted a different orientation mode when compared with the γ-form crystal, i.e., its *c*-axis must be in parallel to the shear direction.

4.5 Structure development during crystallization

The whole-pattern analysis also allowed us to distinguish scattered intensity from both portions of oriented crystals and unoriented crystals. Chains in bulk state cannot response to external field in a uniform manner. After the cessation of the step-shear, shorter chains intend to relax faster;[112] the orientation of later-grown crystals is less influenced by shear. Correspondingly, for a given (*hkl*) plane, both isotropic fraction (ring with uniform intensity distribution) and oriented fraction were observed in diffraction pattern. In this case, **Eq.(2.12)** can be modified using an additional parameter P_0 which quantifies the portion of unoriented crystal, as follows.

$$J(s,\phi) = \overline{I_{hkl}(s)} \cdot [P_0 + (1-P_0)F(\phi,\phi_{hkl})] \qquad \textbf{(4.5)}$$

where P_0 varies from 0 to 1. For powder pattern, P_0 =1 since the second term in the bracket describing the polar distribution of intensity vanishes. More details of crystallization kinetics can thus be investigated, and results are shown in **Figure 4-9**.

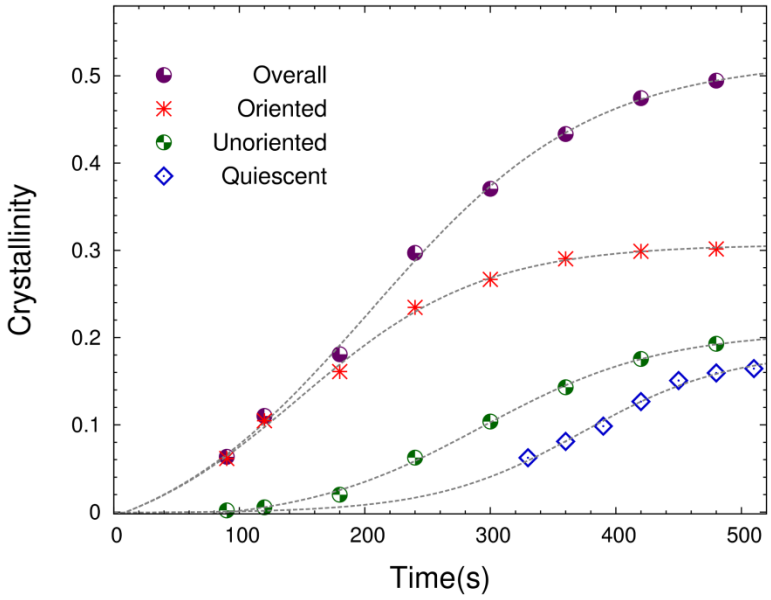

Figure 4-9. Crystallinity change as a function of time. Contributions from both oriented and unoriented crystals are shown. Result from quiescent crystallization is also shown for comparison purpose.

Overall crystallinity change during shear-induced crystallization and that during quiescent crystallization is plotted together for comparison purpose, where the first measureable value was about 5%. Below this value, the scattered intensity was too weak to give confident

result. In **Figure 4-9**, it is seen that the shear flow not only enhance the crystallization kinetics but also the crystallinity of P-B copolymer. In quiescent crystallization, the crystallization half-time is about 360 *s* and the final crystallinity is about 17%. With the application of a step-shear, the crystallization half-time decreases to 240 *s* and the final crystallinity become 49%.

The enhancement of crystallization under external field, in both kinetics and final crystallinity has been reported by many authors before.[113, 114] This phenomenon is a consequence of the influence of shear on two aspects of the crystallization process, i.e., nucleation and growth. On one hand, shear stretches and aligns polymer chains, which lowers nucleation barrier considerably.[115-117] The nucleation density is thus greatly enhanced. On the other hand, flow-induced nuclei serve as good substrates for further growth of crystals. This point can be well explained by typical microscopic image of cross section of polypropylene after extrusion.[118] Usually the skin layer has much higher space filling degree by crystals as compared to that in core layer.[118-120] Furthermore, the large increase of crystallinity was mainly contributed by the oriented portion of crystals. After subtraction of this portion, the remained crystallinity (from pure unoriented portion of crystals) was found to be decreased to a level of about 20%. However, the unoriented crystal fraction was still slightly higher than that of quiescent crystallization; and the corresponding crystallization rate was also faster. This behavior might be due to the enhancement of nucleation density induced by shear:[120] small nuclei may not induce the geometric orientation of crystals, but they can speed up the crystallization process. **Figure 4-9** also indicates even though the experimental data point below 5% was not accessible, the curve can be extrapolated to the very early stage of crystallization. In the early stage, the scattering was weak due to the low volume fraction of the nuclei and/or poor crystal ordering.

To investigate the change of crystal ordering, the model of disorder of the first kind was used to analyze the *in-situ* WAXS results. In this analysis, each atomic group is allowed to deviate from its corresponding ideal crystallographic position independently, which is to say, the structure factors become different for the unit cell in different spatial positions. The averaged structure factor $\overline{F}_{\mathrm{hkl}}$ can be written as follows, considering this random deviation.[63]

$$\overline{F_{hkl}} = F_{hkl} \cdot \exp\left(-\frac{2\pi^2}{3} s^2 \Delta X^2 \right) = F_{hkl} \cdot \exp\left[-\frac{2\pi^2}{3} \left(s_{12}^2 \Delta X_{12}^2 + s_3^2 \Delta X_3^2 \right) \right] \qquad \textbf{(4.5)}$$

where ΔX represents the averaged deviation of atomic groups from their ideal crystallographic position. Since we assume the system consists of fiber symmetry, ΔX can be further decomposed to ΔX_{12} (deviation in the *ab*-plane) and ΔX_3 (deviation along the *c*-axis). This equation is equivalent to the formula of Debye-Waller factor, which is often used to characterize the deviation due to thermal agitation. The change of ΔX as a function of time during crystallization is shown in **Figure 4-10**. It is seen that ΔX decreases continuously during crystallization, indicating crystals become more and more perfect. The continuous decrease of ΔX can give some insights into the crystallization structure formed at the early stage. If this trend is consistent, the deviation must be large at very early stage, making it reasonable to speculate that during this period, small crystal blocks with large degree of disorder has already been formed. These tiny crystal blocks eventually evolve into large crystalline lamellae.[121 122]

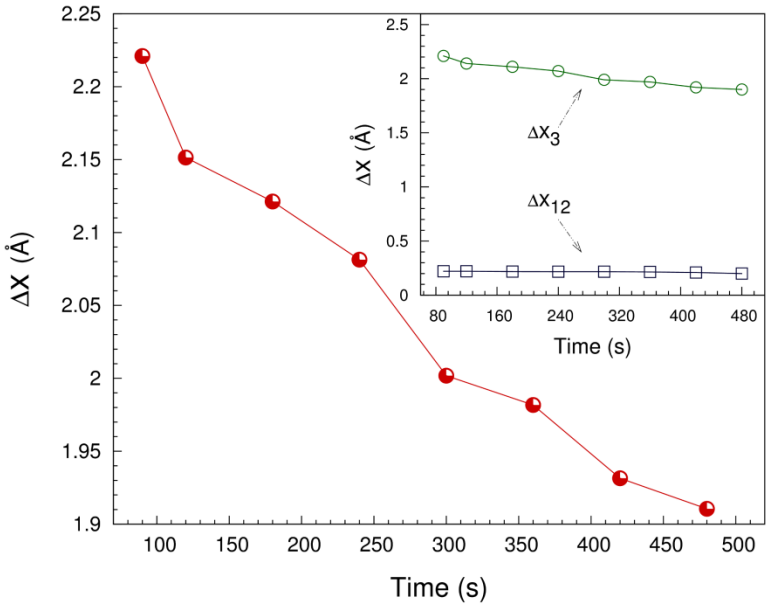

Figure 4-10. Change of deviation of atomic group from their ideal crystallographic positions, ΔX, as a function of crystallization time. In-set shows the deviations in the *ab*-plane (ΔX_{12}) and that along the *c*-axis (ΔX_3).

The in-set of **Figure 4-10** shows the changes of ΔX_{12} and ΔX_3 with time. It is found that the overall deviation is mainly contributed by ΔX_3, i.e., deviation along the horizontal direction. This is manifested in the scattering profile that reflection peaks near the horizontal direction suffer a systematic decrease in intensity. It further means that the stacking fault would be mainly due to the bilayer packing along the *c*-axis. This is reasonable since the *c*-axis direction has more

spatial degree of freedom for the γ-phase. Using **Eq.(4.5)**, we can also compare the crystallinity with and without considering the disorder effect. The results are shown in **Figure 4-11**. In **Figure 4-11**, X_1 refers to the overall crystallinity, i.e., with consideration of disorder; and X_2 is the crystallinity of 'perfect' crystals without defect (their changes are shown in the in-set). $(X_1 - X_2)/X_1$ naturally gives the content of defect in overall crystallinity. For the random copolymer system, this value is very high. It is about 50% in the early stage of crystallization. This is because that the non-crystallizable comonomer segments hinder the chain arrangement in crystals. The ratio decreases with the eclipse of time, indicating crystals become more and more ordered. These results are in agreement with **Figure 4-10**.

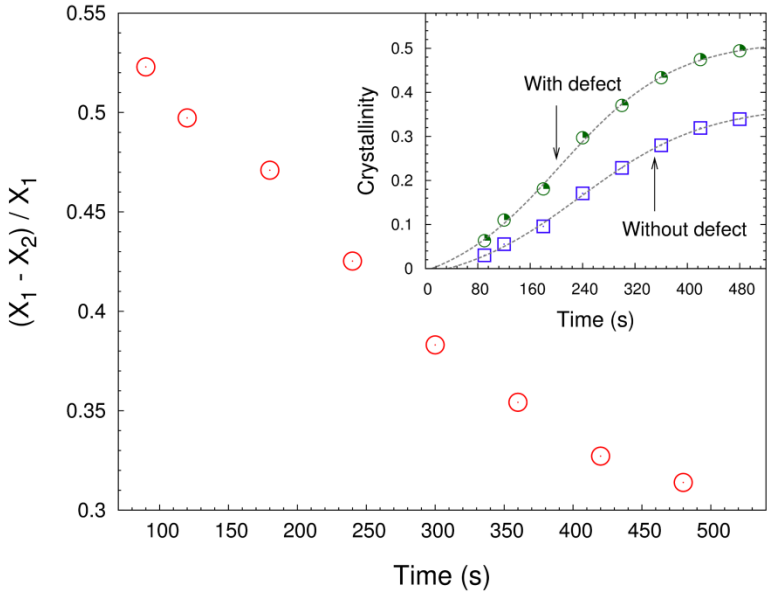

Figure 4-11. Ratio of crystallinity contributed by defect and overall crystallinity change as a function of time. In-set shows crystallization curves using crystallinity calculated with and without considering influence of disorder.

Together with the ordering process, crystals grow in the same time. Crystal size can be calculated using the reciprocal integral width. (008) plane was used for evaluation since it directly gave the size along *c*-axis of γ-form crystal. The result is plotted in **Figure 4-12**. The first measurable value is 16 *nm*, starting from the 90 *s*. It increases to about 18.5 nm after 150 s and reaches the plateau value. After that, although the ordering process continued (seen from **Figure 4-10 and 4-11**), the sizes of crystals stopped increasing. The ordering process and crystal

growth need not to be dependent with each other since crystal growth is also restricted by other factors such as crystal impingement, poisoning on growth facet, and so on.

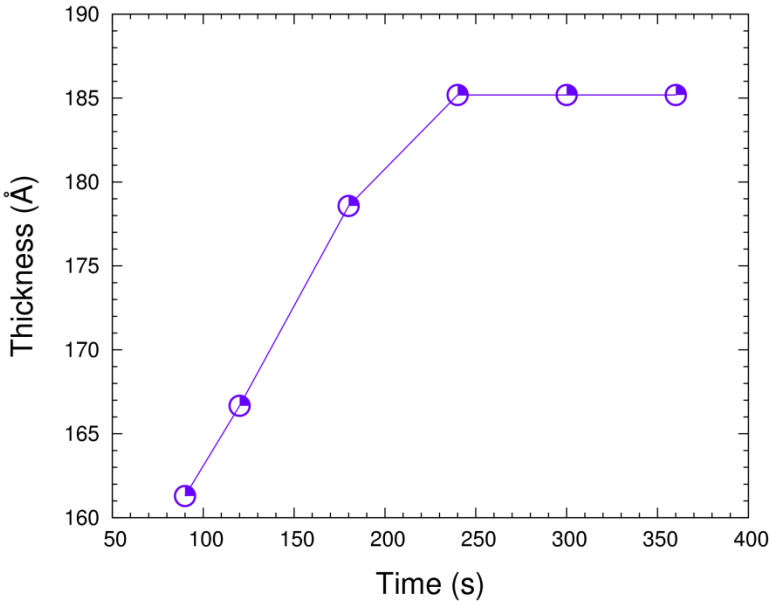

Figure 4-12. Change of crystal dimension of γ-phase along *c*-axis, derived from reciprocal integral peak width of the (008) peak.

The degree of orientation can be quantified with Hermans' orientation parameter $\langle P_2 \rangle$, which varies from -0.5 to 1.[64] Negative values represent perpendicular orientation situation. Since we adopted parallel orientation for calculation, $\langle P_2 \rangle$ ranges from 0 to 1, with 0 corresponding to random orientation and 1 to perfect alignment of crystals in the direction of fiber axis. Using the Onsager distribution, $<P_2>$ can be analytically given by[75]

$$\langle P_2 \rangle = 1 - 3[\coth(p) - 1/p]/p \qquad \textbf{(4.6)}$$

When the portion of unoriented crystals is subtracted, $\langle P_2 \rangle$ becomes the degree of orientation of pure oriented crystals. The results are shown in **Figure 4-13**, where the change of $<P_2>$ that is related to the breadth of polar distribution of intensity, is plotted as a function of crystallization time. In is seen that the value of $\langle P_2 \rangle$ exhibits a decrease trend during crystallization. This could be attributed to the chain relaxation after shear. The rate of decrease was significant in the early stage and was slowed down after that, due to the increase of viscosity during the solidification process.

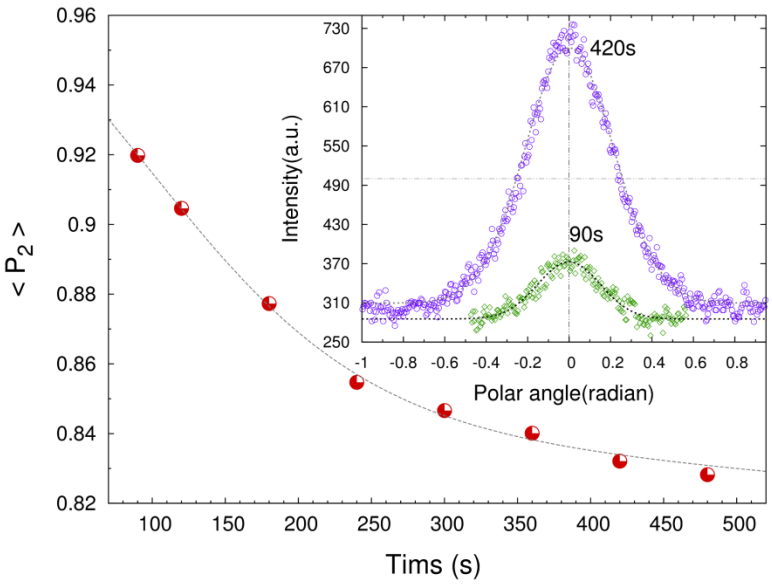

Figure 4-13. Change of $\langle P_2 \rangle$ as a function of time. In-set shows polar scans of intensity peaked at s = 0.184 Å^{-1} (i.e., the (008) plane for γ-phase and (040) plane for α-phase) from experimental data gathered at 90 s and 420 s, respectively.

4.6 Summary

The shear-induced crystallization behavior of P-B random copolymer was investigated using time-resolved WAXS technique. The experimental data was analyzed using the 2D whole-pattern simulation approach. Comprehensive consideration of scattered intensity dependence on both polar angle ϕ and scattering vector s made it possible to identify the polymorphism as well as preferred orientation of the polymer. The main conclusions can be summarized as follows:

1. When crystallized at 100 ^{o}C, the P-B copolymer was dominated by γ-form crystal of iPP, which was coexistent with about 20% of α-form crystal. The application of shear made the c-axis of γ-form crystal oriented perpendicular to the shear direction, while α-form crystal showed conventional orientation mode with the c-axis parallel to the shear direction.

2. The kinetics study indicated that the shear flow significantly accelerated the crystallization rate. The crystallinity was also greatly increased as compared with that in quiescent crystallization. These enhancements were mainly due to the increased fraction of oriented polymer chains.

3. The crystal perfection process was clearly revealed by the analysis using the model of disorder of the first kind. A very large amount of crystal defect was found in P-B random copolymer, especially in the early stage.

4. The degree of crystal orientation was calculated, which indicated a continuous decrease in the early stage, owing to the relaxation behavior of polymer chains after the step-shear.

5 Crystallization during Uniaxial Stretching

5.1 Introduction

In chapter 4, crystallization of P-B copolymer after being deformed by a step-shear was investigated in detail by 2D WAXS technique, facilitated with whole-pattern simulation. In that case, shear flow was performed on the supercooled polymer melt; and the crystallization was completely influenced by the extension/orientation of chains in the liquid state (although viscous). The entire crystallization process took place in quiescent condition after shear. Another type of external force field, namely, uniaxial stretching which is much stronger (but simpler in nature) compared to the shear flow can also be employed. Uniaxial stretching is frequently utilized in industry to produce high performance polymeric material, e.g., polymeric fibers with high tensile modulus. In this process, sample is fixed in two ends and is continuously extended by mechanical force introduced by a stretching machine. Polymer chains can be highly oriented in the machine direction, resulting in an excellent mechanical property.

A macroscopic method to directly measure the response of polymer bulk to the external tensile force is the stress-strain curve which is obtained by recording the stress loaded to the sample during stretching as a function of strain (sample deformation). **Figure 5-1** shows the stress-strain curve of P-B copolymer uniaxially stretched at 100 ^{o}C (detailed description of the experimental procedure can be found in the experimental section).The general trend is typical for semi-crystalline polymer. In **Figure 5-1**, Point 1 is the yield point. We refer the interval from the very beginning of stretching till the end of yielding (point 2, strain ≈ 0.5) as the early stage. The interval from point 2 to point 3 during which stress keeps almost unchanged as strain increases, is referred to as the intermediate stage. After the point 3 till the end of stretching, stress increases monotonically with strain. We denote this period as the late stage. It should be mentioned that the division of a stress-strain curve is dependent on the procedure of the stretching experiment. Some authors[123, 124] found that for the real stress-strain curve (corrected for sample thickness variation), five regions can be distinguished. This sample thickness correction was not performed for our experiment, and hence the curves obtained are more precisely to be called the engineering

stress-strain curve. The division of three stages is easy to be implemented with WAXS/SAXS patterns being monitored.

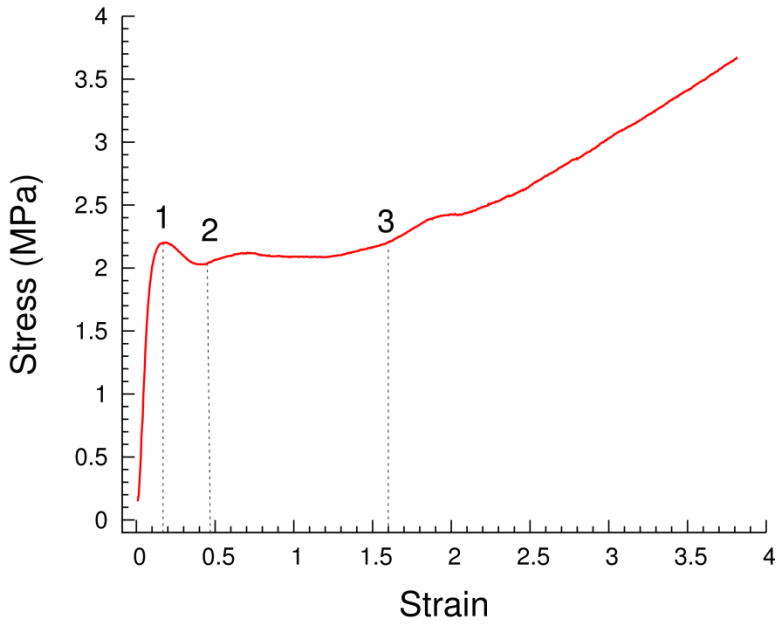

Figure 5-1. Stress-strain curve of P-B co-polymer stretched at 100 ^{o}C.

The main difference between shear-induced crystallization experiment described in chapter 4 and the stretching experiment which will be dealt with in this and the following chapters is that tensile force is continuously applied to the bulk polymer sample during the entire process. The tensile force can be very strong since two ends of the sample are fixed by two clamps of the stretching machine; while in step-shear experiment, shear is generated by two rotary plates that are attached to the outer surface of the sample. This difference implies that there are two processes that are possible to take place. On one hand, tensile force stretches polymer chains, which is favorable for crystallization as discussed before. On the other hand, it can be very strong and is able to deform or destruct preexisting crystals. These two competitive processes control the polymorphism, as well as morphology of the polymer, and consequently, determine the mechanical performance of the material. The task of this and the following two chapters is to reveal this structure-property relationship of propylene-based random copolymer. Chapter 5 and 6 will focus on P-B with low content of butene comonomer; chapter 7 will examine the influence of temperature.

5.2 Experimental

5.2.1 The stretching instrument

An INSTRON machine was used to apply uniaxial stretching. The stretching instrument and the geometry of scattering experiment are illustrated in **Figure 5-2**. Stretching is applied to the sample (in a dumbbell shape) by two moving stages that move in the same speed but in opposite directions (up and down). In this way, the force is transmitted symmetrically; and the central part of the sample will remain in the same position during the experiment, so that the recorded scattering patterns represent structure development in the same position in the sample. Two clamps are connected to the stages and are used to fix the ends of the sample. A chamber covered by Kapton films is mounted outside to surround the sample; hot nitrogen air is blew into the chamber by a heat gun to control the temperature. The speed of stretching was set to 6 *mm*/*min* in all experiments.

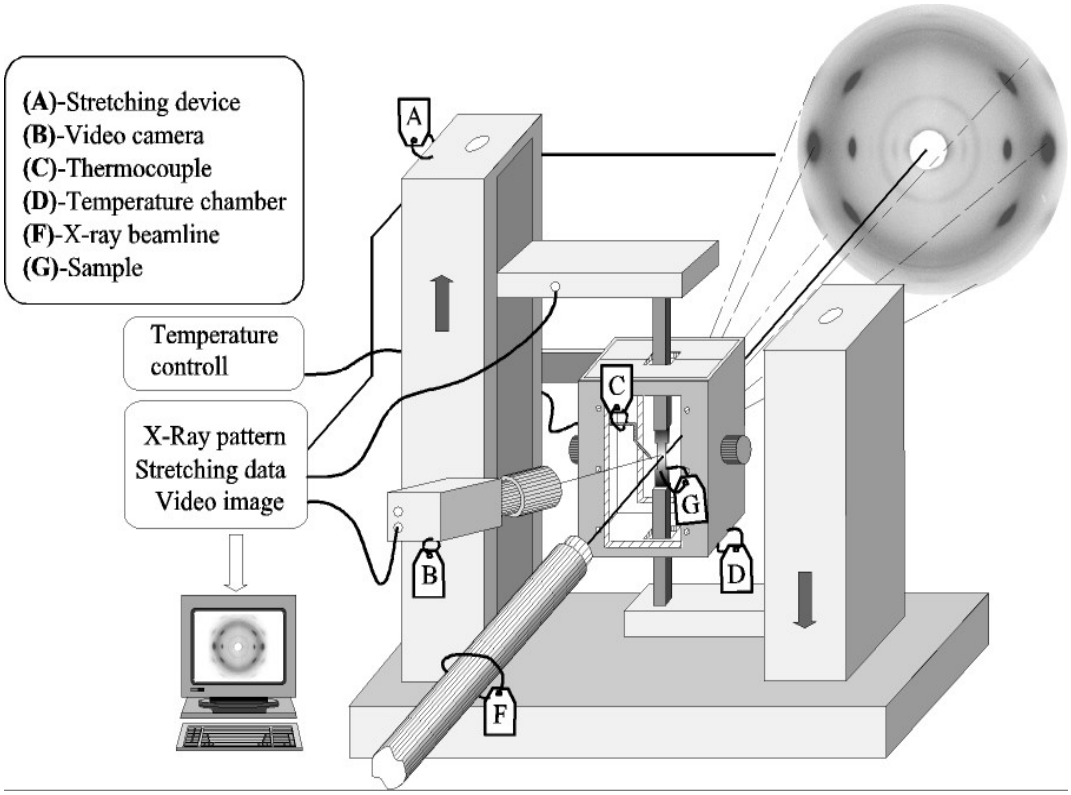

Figure 5-2. Schematic of the stretching machine and the geometry of the time-resolved scattering experiment.

5.2.2 Materials and experimental procedure

Sample tested in this chapter is the same as that has been described in chapter 4, and hence will not be repeated here. Bulk sample was first melted and kept at 150 ^{o}C using a mold with a thickness of 1.0 *mm* for 5 *min* and then naturally cooled down to the room temperature. The film was then cut into 30.0 *mm* long dumbbell-shape pieces. The widths of two ends and the central part of the dumbbell were 9.0 *mm* and 4.0 *mm*, respectively. The experimental protocol is as follows. The sample was held by two clamps of the INSTRON machine and was kept at 100 ^{o}C for 2 *min* to reach thermal equilibrium and then uniaxially stretched with a constant speed of 6.0 *mm*/*min* at this temperature. In the same time, scattering patterns during stretching were captured by a MAR CCD camera in a time-resolved manner. A schematic of the procedure is shown in **Figure 5-3**. The stretching experiment was terminated at the strain of 3.7.

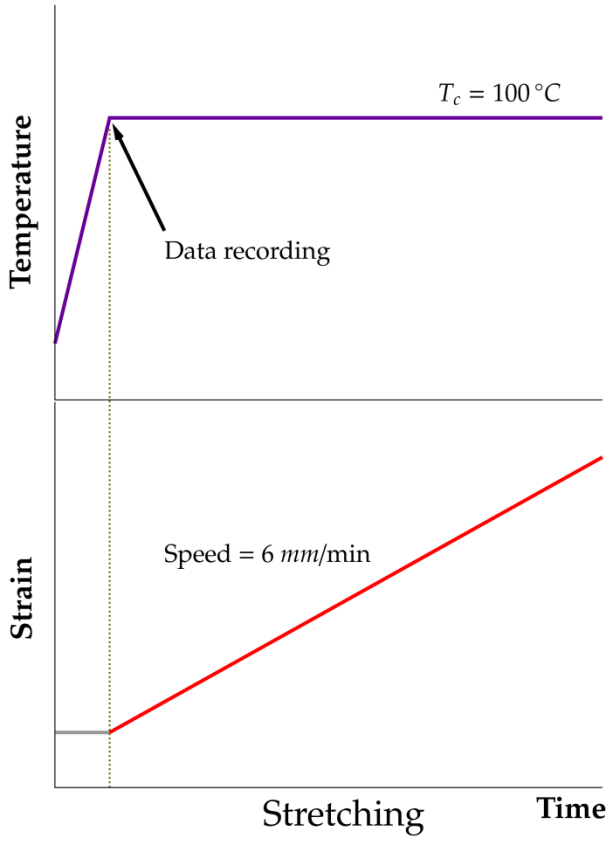

Figure 5-3. Schematic of the experimental protocol.

5.3 Polymorphism and preferred orientation

5.3.1 A preliminary analysis

Based on the analysis in chapter 4, two candidate crystal forms, namely, α - and γ -phase are selected at this moment. Keep in mind that γ -phase is the dominant modification in the static condition. A typical diffraction pattern of P-B copolymer stretched at 100 ^{o}C with strain = 0.5 is shown in **Figure 5-4**. As has been shown in **Figure 4-1c** in chapter 4, diffraction peaks of α - and γ -phase are largely overlapped, therefore in **Figure 5-4**, all possible (*hkl*)s are indexed for main diffraction arcs. The diffraction pattern obtained under stretching is more complicated as compared with that in shear experiment. Three equatorial arcs are visible, which can be naturally assigned to the α -phase with the most common orientation mode, namely, the *c*-axis is in parallel to the fiber axis (in this case, the stretching direction). The three arcs can be indexed as (110), (040) and (130), respectively. Assignment of $(117)\gamma$ and $(130)\alpha$ are straightforward, as they are signature peaks of these two modifications. The innermost arc close to the meridian and the second arc in the equator are possible to be assigned to the γ -phase, indexed as (111) and (008). This has been explained in chapter 4, in **Figure 4-5**. As will be shown later, α -phase becomes important in the stretching experiment, we also need to consider the other possibility of its orientation, that is, the daughter lamella (or lamellar branch) which has an about 80 ^{o} angle with respect to a mother lamella. Consequently, if mother lamellae adopt a *c*-axis orientation, the (110) of the unit cells in a daughter lamella will appear near the meridian, as shown in **Figure 5-4**. Since the arcs are broad, the innermost arc near the equator (not on the equator) can also be due to the cross-β configuration of the γ -phase, indexed as (111). Cross-β configuration has been discussed in chapter 4. In that case, the fiber axis is horizontal, and hence the $(111)\gamma$ is close to the vertical direction. If arcs close to the horizontal direction are assigned to $(111)\gamma$, owing to the cross-β configuration, the fiber axis must be vertical, which is true for our stretching experiment, as shown in chapter 2, **Figure 2-9**.

A unique character of diffraction pattern formed under stretching is the occurrence of a strong off-axis diffraction arc in the position around s=0.19 Å^{-1}, in the same s value as that of $(008)\gamma$ and $(040)\alpha$. In both orientation modes of the α -phase (mother and daughter lamellae),

(040) arc is located in the equator. Therefore this off-axis arc is tentatively assigned to (008) plane of the γ-phase. We will explain its formalism later.

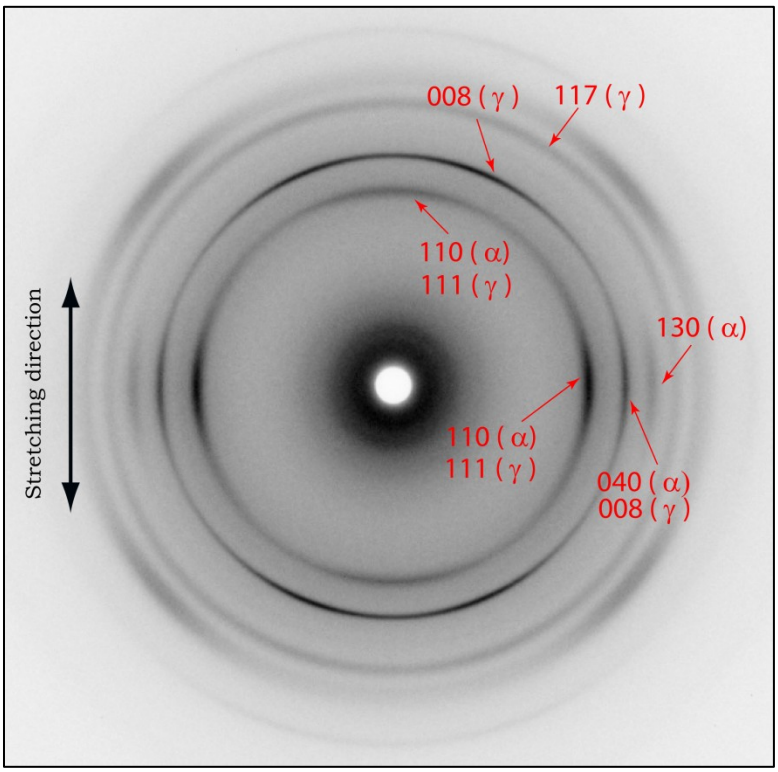

Figure 5-4. Fiber diffraction pattern of P-B copolymer stretched under 100 ^{o}C at strain = 0.5. All possible (*hkl*)s of α - and γ-phase are indexed for main diffraction arcs.

5.3.2 Considering the orientation mode

Deciphering fiber diffraction pattern such as the one shown in **Figure 5-4** needs to be very careful. Information of peak positions based on the s values alone is not enough to describe the real structure. Main diffraction arcs in **Figure 5-4** will be analyzed one by one with consideration of possible orientation modes, as discussed as follows. As mentioned above, the second arc in the equator is possible to be index as $(008)\gamma$ and $(040)\alpha$. Possible orientation modes corresponding to the first case has been illustrated in **Figure 4-5**, in chapter 4. **Figure 4-5c** should be excluded first, as in this stretching experiment, the fiber axis is vertical. **Figure 4-5b** is possible but is not realistic in uniaxial stretching as in this case only extensional force is applied to the sample; rotational force vanishes. Therefore the diagonal orientation as shown in **Figure 4-5a** and the cross-β configuration with the fiber axis being vertical will be two

candidates for γ-phase's orientation. Together with two orientation modes of the α-phase, i.e., the *c*-axis orientation of mother lamellae and unit cells in daughter lamellae, four possible orientation modes are illustrated in **Figure 5-5**.

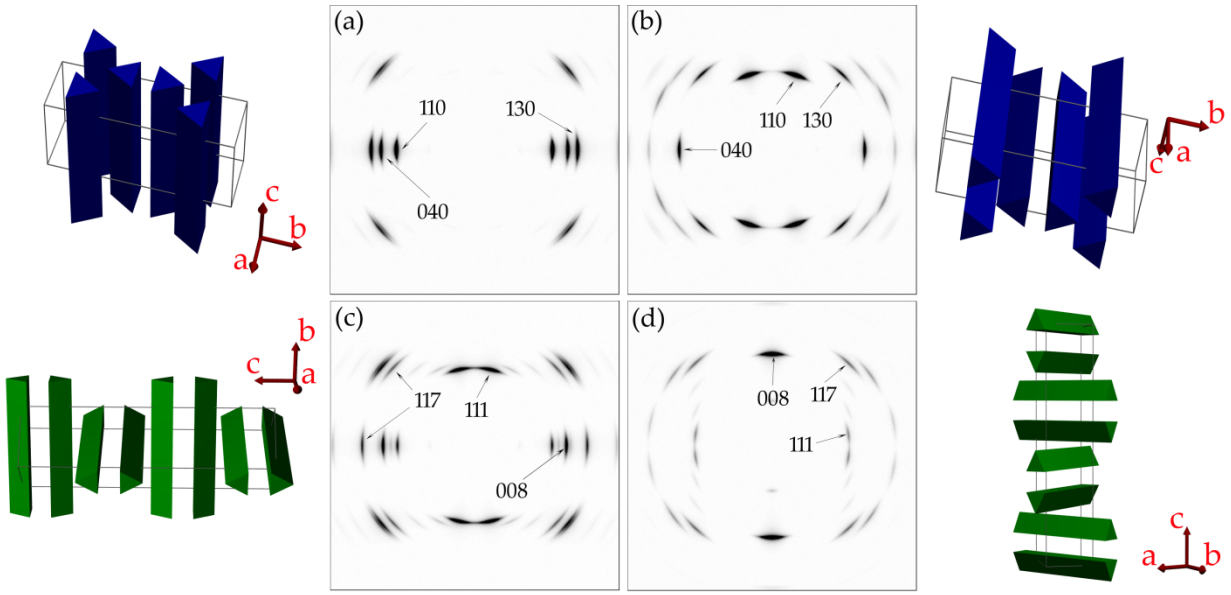

Figure 5-5. Simulated fiber diffraction patterns of the α-phase with the *c*-axis orientation **(a)**; daughter lamellae of the α-phase **(b)**; γ-phase diagonal orientation **(c)** and γ-phase with cross-β configuration **(d).** Model of unit cells are shown beside patterns. The fiber axis is vertical.

All patterns in **Figure 5-5** belong to parallel orientation. Therefore Onsager ODF was used to calculate the patterns. For the γ-phase, **Figure 5-5c** is first excluded because 1) (117) is split into three arcs with one of them located on the equator (see chapter 4 for detail), and this is not observed; and 2) (008) is on the equator, which cannot explain the off-axis arcs as shown in **Figure 5-4**. Cross-β configuration shown in **Figure 5-5d** has been reported for stretching of iPP. A slight modification of this orientation mode makes it possible to fit our data, that is to say, the *c*-axis of the unit cell needs to be tilted in some way, rather than be in parallel to the fiber axis. The scheme of the *c*-axis tilting will be introduced later. At this moment, it needs to be pointed out that if cross-β configuration is employed, the first arc near the meridian cannot be generated by the γ phase. Therefore it must be due to the unit cells in daughter lamellae of the α-phase, as shown in **Figure 5-5b**. **Figure 5-5a** which represents the mother lamellae with the *c*-axis orientation explains the three equatorial arcs quite well.

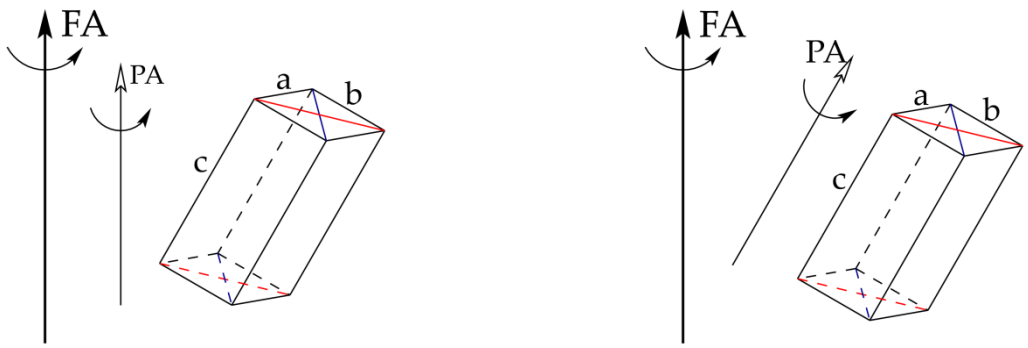

(a) **(b)**

Figure 5-6. Two possible schemes of tilting of γ-phase unit cell. **(a)** parallel orientation; **(b)** oblique orientation. Details can be found in chapter 2.

There are two possibilities for the γ-phase to generate off-axis (008) diffraction arcs. The simplest one is to keep the parallel orientation mode, but tilt the unit cell with respect to the FA (or PA, as they are the same for parallel orientation) for a degree ϕ_{008}, which is shown in **Figure 5-6a**. The other way, as shown in **Figure 5-6b**, is to use oblique orientation. As has been explained in chapter 2, simulation of oblique orientation is not straightforward. The main difficulty lies in the fact that no appropriate ODF can be used to produce analytical solution to the transformation kernel $F(\phi,\phi')$. Therefore numerical integration or Legendre expansion approach has to be employed. For WAXS pattern, this would be a formidable task, as these operations have to be applied to all diffraction arcs, which is apparently not feasible with currently available computation ability. Thus the first model, i.e., the tilted cross-β configuration will be used for calculation, keeping in mind that the oblique orientation might be more realistic. The tilted cross-β configuration model will become more realistic when (008) arcs are close to the meridian, which is what has been observed (the change of the tilting angle of (008) arcs will be discussed later).

To calculate scattering pattern of this type, one need to rotate coordinates of a unit cell accordingly beforehand. The coordinate rotation can be done in a standard way: the new coordinate $\mathbf{x}'$ after rotation is related to the original one $\mathbf{x}$ by[70]

$$\mathbf{x}' = \mathbf{T}_r \cdot \mathbf{x} \qquad \textbf{(5.1)}$$

where $\mathbf{T}_r$ is the rotational tensor. For simple fiber symmetry, rotating about the *a*- or the *b*-axis for a $\pm\phi_{008}$ degree leads to the same tilting of the (008) plane in fiber diffraction patterns. However, since other reflection planes will also be subjected to a change if rotated, it is required that the entire pattern generated after coordinate rotation must be in consistent with experimental one, not just the single (008) plane. With this consideration, simple rotation over the *b*-axis for $\pm\phi_{008}$ was finally adopted, giving equal possibility of positive and negative value (clock-wise and anti-clock-wise). After rotating original coordinates of atomic groups, a new set of coordinates is generated. Calculation of fiber diffraction pattern will be entirely based on the new coordinates, and the methodology has been introduced in chapter 2 and 4.

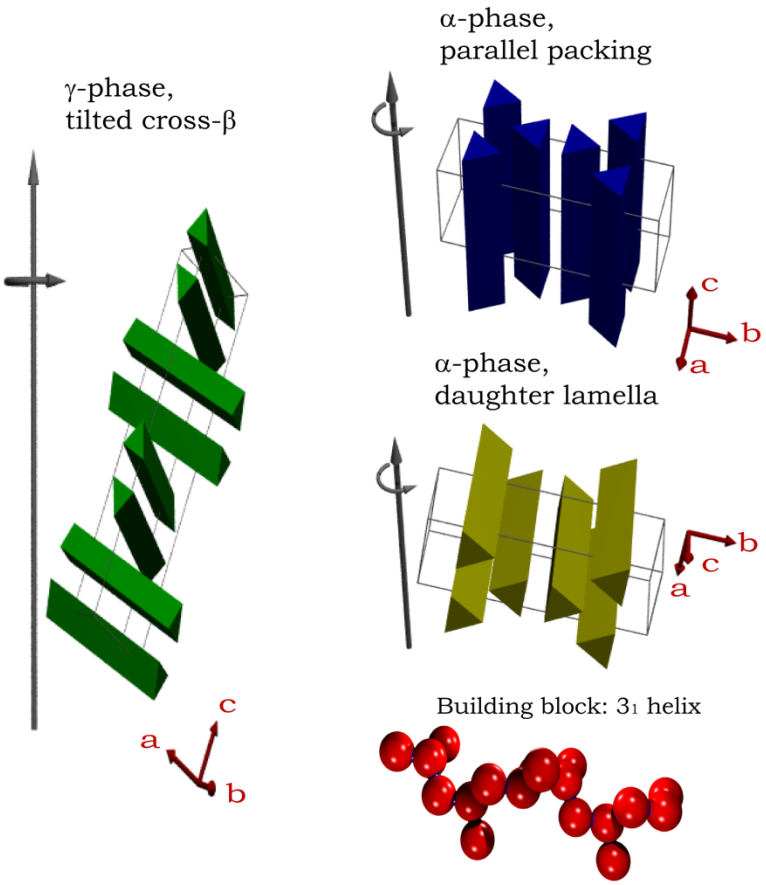

Figure 5-7. Illustration of two crystal modifications of iPP and their possible orientation modes occurred during stretching experiment at 100 ^{o}C.

Figure 5-7 illustrates two crystal modifications with three orientation modes that are used for 2D fiber diffraction pattern simulation in this study. It consists of the γ-phase with tilted

cross-β configuration, the mother lamellae with the *c*-axis orientation and the daughter lamellae with the *c*-axis having an 80 ^{o}C angle with respect to the fiber axis. Examples of comparison of simulated 2D WAXS patterns with the corresponding experimental counterparts that are generated with the considerations of all above facts are shown in **Figure 5-8**. Simulated and experimental patterns at two strains, i.e., 0.5 and 2.2, corresponding to the structure after yielding and structure in the late stage of stretching are shown. Again, in both figures in **Figure 5-8**, the upper left and lower right corners are quarters from the experimental pattern, and the other two complimentary corners show the simulated ones. In the early stage, there are still considerable amount of the γ-phase, but as stretching proceeds, the α-phase becomes dominant (the γ-to-α transition will be discussed in detail later). Main diffraction arcs are indexed. It needs to be pointed out that in the late stage when only little γ-phase is survived, the first innermost arcs close to the meridian still exist. This further indicates that they are not contributed by γ-phase with diagonal orientation as shown in **Figure 5-5c**, but by the (110) arcs of daughter lamellae of α-phase.

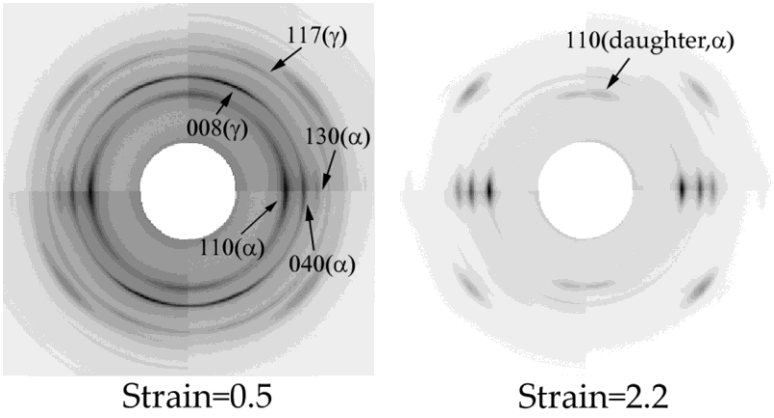

Figure 5-8. Typical WAXS patterns at low strain (0.5) and high strain (2.2). The upper-left and lower-right quarters are experimental data; upper-right and lower-left quarters are computed ones. The polymorphs used for diffraction pattern computation are annotated; their orientation modes are discussed in the context.

A detailed comparison of experimental data and simulated pattern is shown in **Figure 5-9** where polar dependence of scattering intensity at around s=0.16 Å^{-1} and s=0.19 Å^{-1} (**Figure 5-9a** and **5-9b**), and the 1D scattering profile (**Figure 5-9c**) from experimental data and simulated result are plotted. The schemes of obtaining intensity change as a function of polar angle are shown on the right side of **Figure 5-9a** and **5-9b**. It is convincing that the current model explains

the experimental WAXS pattern quite well. However, the molecular mechanism of the tilting of the cross-β configuration of the γ-phase is not clear at this moment.

The tilted cross-β configuration deserves a deeper analysis. The unit cell orientation/tilting is possible to be coupled with lamellar orientation which is revealed by SAXS. **Figure 5-10a** shows a typical SAXS pattern in the early stage of stretching during which SAXS patterns change from isotropic ring to a four-point pattern. It is interesting that the four lobes in SAXS pattern move toward the equator as stretching proceeds, and the tilting angle (polar angle of the intensity maximum of a lobe with respect to the fiber axis) ϕ_{SAXS} is roughly equal to $\pi/2-\phi_{008}$. The change of the tilting angle during stretching as obtained from both WAXS and SAXS patterns are shown in **Figure 5-10b**. ϕ_{008} is retrievable till the end of stretching in WAXS patterns. But after the completeness of yielding (around strain = 0.5, seen from the stress-strain curve), the change slows down and eventually ϕ_{008} is fixed at an angle about 20 ^{o}. There are only 5 data points that can be obtained from SAXS images, since SAXS pattern only exhibit four-point pattern in the early stage (strain < 0.6); after that, it changes into two-point pattern which will be discussed in detail later.

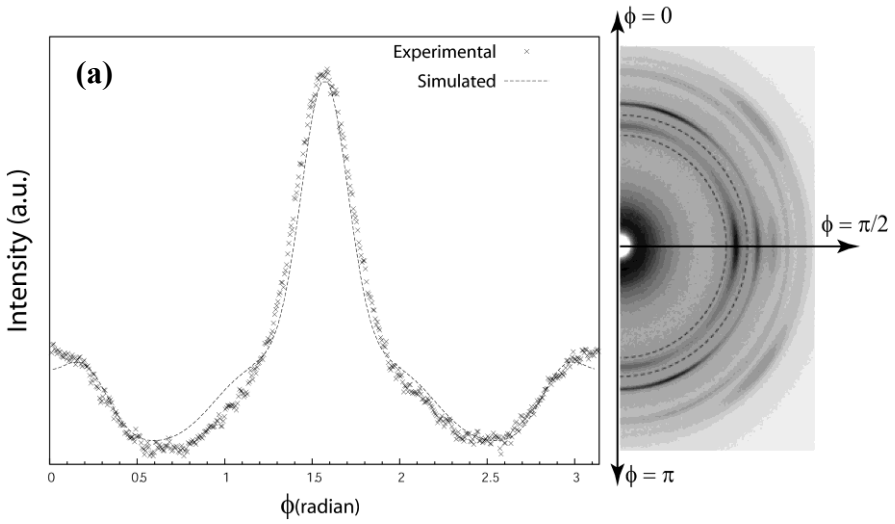

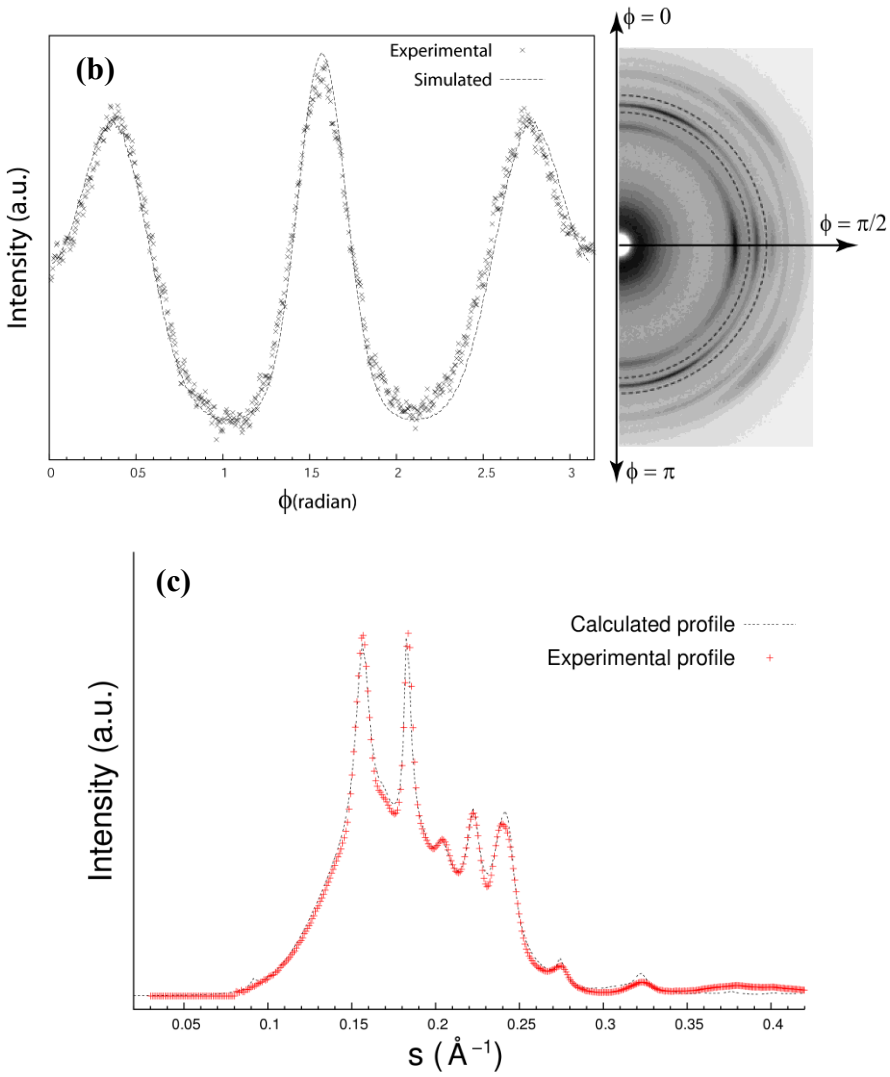

Figure 5-9. Selected profiles of intensity distribution over polar angle ϕ (**a, b**). Profiles on the left are corresponding to intensity within regions between dashed lines in diffraction patterns. A comparison of 1D scattering profile is shown in (**c**). P-B copolymer was stretched under 100 ^{o}C at strain = 0.5. The content of α -phase equals 60%.

The consistency of the change of WAXS and SAXS patterns strongly suggests that the 'four-point' lobes are closely related to the orientation of the γ-phase lamellae (remember that γ-phase is the dominant modification in the initial state). The geometric relationship between unit cells and a lamella that accommodates them is shown in **Figure 5-10c**. The *c*-axis of the γ-phase unit cell is in parallel to the long axis of a lamella. In **Figure 5-10c**, ϕ_1 and ϕ_2 is equivalent to ϕ_{008} and ϕ_{SAXS} in WAXS and SAXS pattern, respectively; and they are complementary. Stretching polymer bulk is a complex process, since force is transmitted to the

entire chain network, rather than a single chain. For semi-crystalline polymer, lamellar crystals are embedded in the amorphous matrix, and hence the force is not directly applied upon crystals, but being transmitted to lamellae via the network. As shown in **Figure 5-10c**, a γ-phase lamella is anisotropic in shape, with the long axis being the direction of the packing of cross-hatched bilayers. A vertical force tends to rotate and align the *c*-axis in parallel to the force direction. That's the reason (008) arc moves toward the meridian while four-point lobe move in an opposite direction. However, as will be shown below, γ-phase is gradually transformed into α-phase, or, to change a word, the system experiences a phase inversion. Crystals in the network after yielding is dominated by the α-phase, and the γ-phase crystals become less connected with the network. As a consequence, force cannot be effectively transmitted to the γ-phase crystals, and this explains why ϕ_{008} cannot further decrease to zero degree. The change of the nature of the network during stretching will be discussed in detail later.

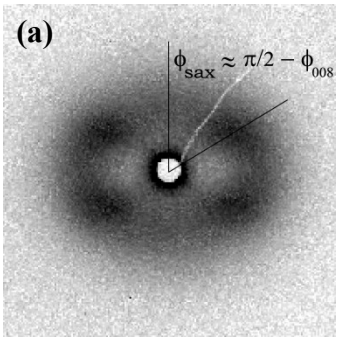

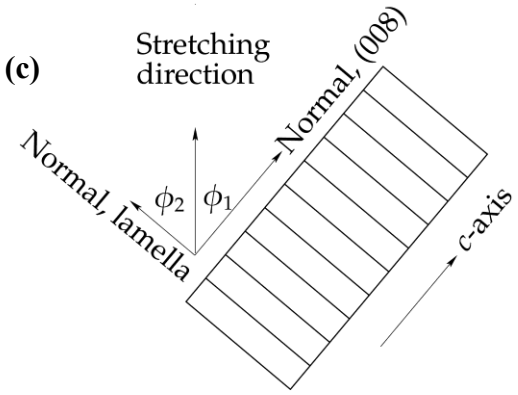

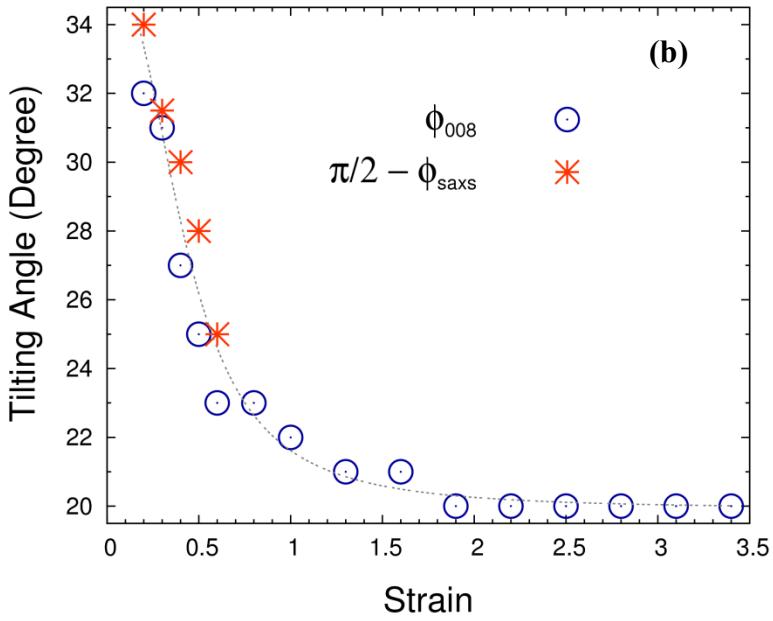

Figure 5-10. A typical four-point SAXS pattern at strain = 0.5 **(a)**; Change of tilting angle as obtained from both SAXS and WAXS data as a function of strain **(b)**; A schematic of arrangement of γ-phase unit cell within a lamellar crystal **(c)**.

5.4 γ-to-α transition

The crystallization process in stretching experiment is quite different from that induced by a step-shear. In the latter case, as indicated in chapter 4, crystallinity increases monotonically. However, as discussed in the introduction section, two competitive processes, namely, the destruction of crystalline due to strong tensile force and recrystallization induced by chain orientation, may take place in the stretching experiment. As a consequence, the crystallinity change as a function of time (or strain) exhibits a nonmonotonic behavior, as shown in **Figure 5-11**. It decreases slightly in the very early stage (strain < 0.2) and then keeps increasing. This decrease is related to yielding. An usual interpretation of structure change before yielding of semi-crystalline polymers is the destruction of lamellar aggregates (spherulites) formed under quiescent condition.[123] Since the temperature (100 ^{o}C) is appropriate, recrystallization takes place in the same time, which results in a continuous increase of crystallinity after yielding.

Disorder effect can be treated in the same way as introduced in chapter 4, using **Eq.(4.5)**. The in-set in **Figure 5-11** shows the portion of disorder change as a function of strain. The monotonic increase of disordered portion is attributed to stress being imposed on crystals,

causing atomic groups being deviated from their ideal positions. This trend is completely opposite to that observed in shear-induced crystallization in which a perfection process has been reported.[76] It again stresses the nature of the stretching-induced crystallization process: crystallization proceeds with the presence of strong tensile force.

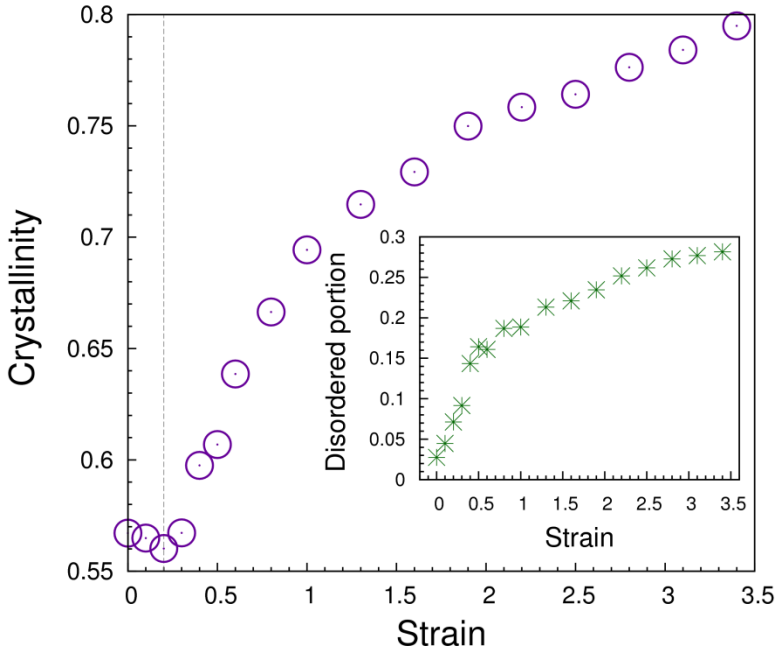

Figure 5-11. Crystallinity change during stretching process. In-set shows change of the portion due to disorder effect.

The crystallinity can be further decomposed into fractions from γ- and α-phase, respectively, as shown in **Figure 5-12**. An opposite trend of change of fractions from two phases is clearly seen. With the fact that the γ-form crystals adopted a tilted cross-β configuration in which the *c*-axis is close to the stretching direction, it is easy to understand that they are unstable if stretched, since chains are packed layer by layer along the *c*-axis in the unit cell. The stretching induced destruction of crystal resembles the melting process.[6] Because polymer chains are still quite mobile at this high temperature, they are intended to form more stable crystal form, the α-phase in this case. Apparently, with parallel packing of polymer chains along the stretching direction, the unit cell of the α-form crystal is more durable as compared with that of the γ-phase. The in-set of **Figure 5-12** shows the relative percentage of the α-phase in the crystalline portion. In the late stage, the composition is completely inversed. α-phase becomes the dominant modification with a relative ratio of about 90%.

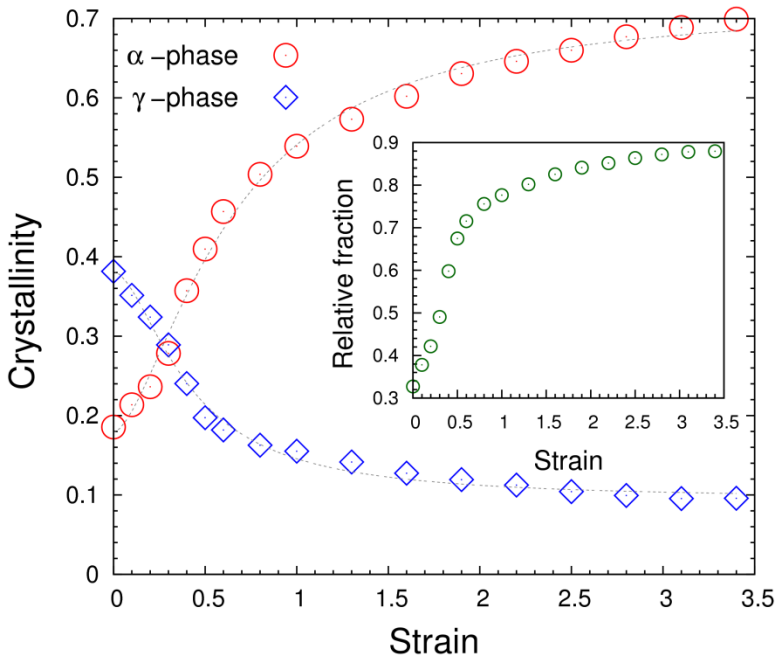

Figure 5-12. Change of crystallinity contributed by γ - and α -phase, respectively. In-set shows the relative fraction of α -phase in crystalline part. It equals 1 if crystalline is completely composed of α -phase.

The degree of orientation of both γ - and α -form crystal can be characterized by the single parameter $\langle P_2 \rangle$ (see chapter 4 for detail); their change as a function of strain are exhibited in **Figure 5-13**. For both phases, $\langle P_2 \rangle$ increases rapidly in the very early stage, followed by a slow increase extending all the way through the intermediate to the late stage. Beyond the point where strain ≈ 0.5, $\langle P_2 \rangle$ of the α -phase becomes higher than that of the γ -phase. $\langle P_2 \rangle$ is only used to characterize oriented portion of crystals. The polar scan of intensity shows constant baseline which is corresponding to unoriented crystals of which the fraction is defined as P_0. The apparent degree of orientation including oriented and unoriented portions is $\langle P_2 \rangle (1 - P_0)$, denoted as $\langle P_2 \rangle_a$. The in-set of **Figure 5-13a** shows its development for both phases. The change of P_0 can be found in **Figure 5-13b**. Again, strain ≈ 0.5 is a critical point beyond which P_0 turns to a slow decrease mode. The decrease of P_0 of the α -phase lasts to the very late stage of stretching where almost all crystals are oriented. In contrast to this continuous decrease, P_0 of the γ -phase gradually reaches a plateau value which is about 40 % higher than that of the α -phase in the late stage. While in the early stage, the unoriented portion of α -phase is lower than that of γ -phase

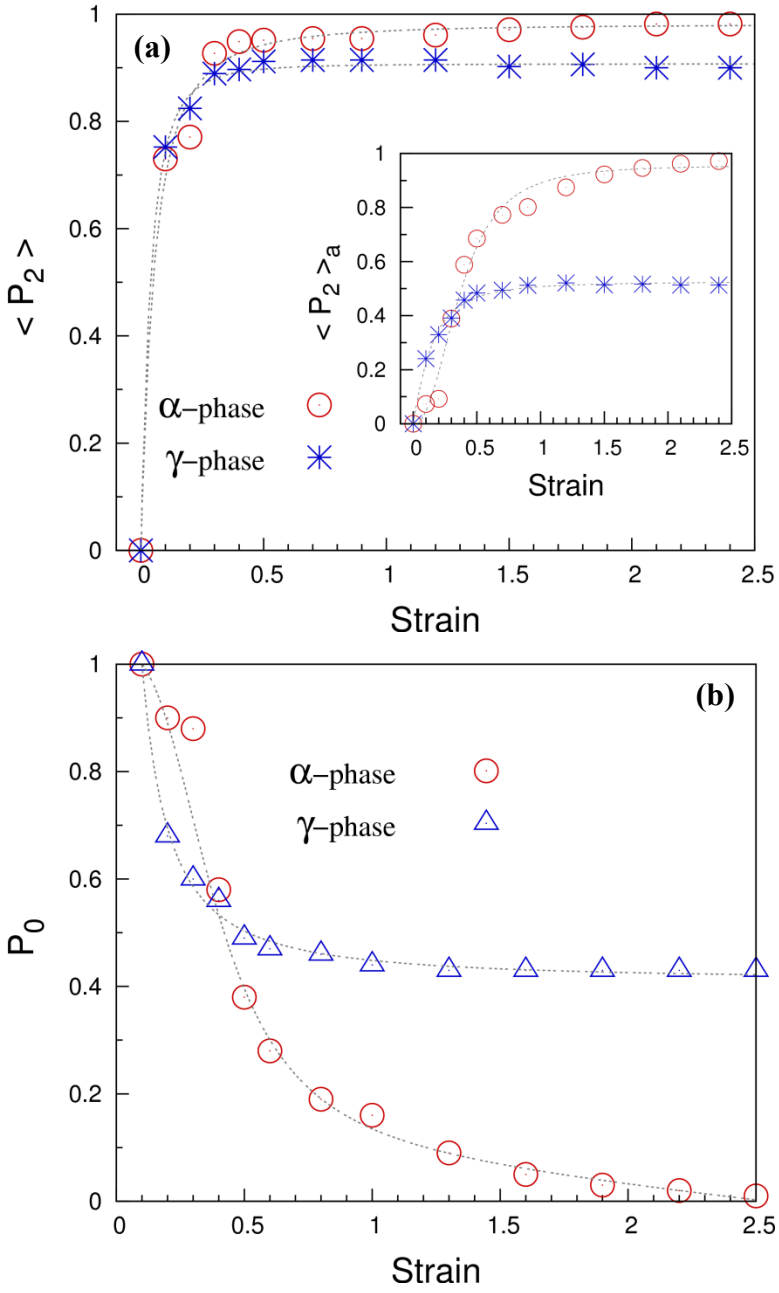

Figure 5-13. Change of Hermans' orientation function $\langle P_2 \rangle$ **(a)** and unoriented portion P_0 **(b)** of γ- and α-phase during stretching. In-set in **(a)** is the same plot of apparent degree of orientation $\langle P_2 \rangle_a$ which is defined in the context.

The common feature of both plots in **Figure 5-13** is the inversion of the changing trend of dependent variables ($\langle P_2 \rangle$, P_0 and $\langle P_2 \rangle_a$) of γ and α-phase. It is directly related to the γ-to-α transition and the change of the nature of the nature work as a consequence. Since the γ-phase is dominant in the beginning, it largely bears the tensile force, and therefore is easy to be

oriented, resulting in an abrupt increase in all these parameters. However, the cross-β configuration cannot survive the continuously increased deformation, owing to it non-parallel chain-packing nature. Newly grown α-phase takes over the role as cross-linkers embedded in the network. In this case, force is mainly transmitted to the α-phase; and the γ-phase becomes less entangled with the surroundings. This scheme not only explains the inversion behavior, but also why the $(008)_\gamma$ cannot be further merged together with the fiber axis, as force is mainly bore by the α-phase network.

5.5 Morphology

To have an integrated understanding of structure development at hierarchical length scales, selected WAXS/SAXS patterns at different strain are shown in **Figure 5-14**. '**E**' and '**S**' in WAXS patterns represent quarters of experimental data and simulated counterpart. As discussed before, in the early stage, the four-point SAXS pattern is closely related to the alignment of the γ-phase lamellae. After that, two-point SAXS patterns are formed, corresponding to the α-phase lamellar structure. The newly grown α-phase lamellae has about the same inter-lamellar distance as that of initial state lamellar structure. This can be evidenced from development of long period L obtained from 1D SAXS profile.

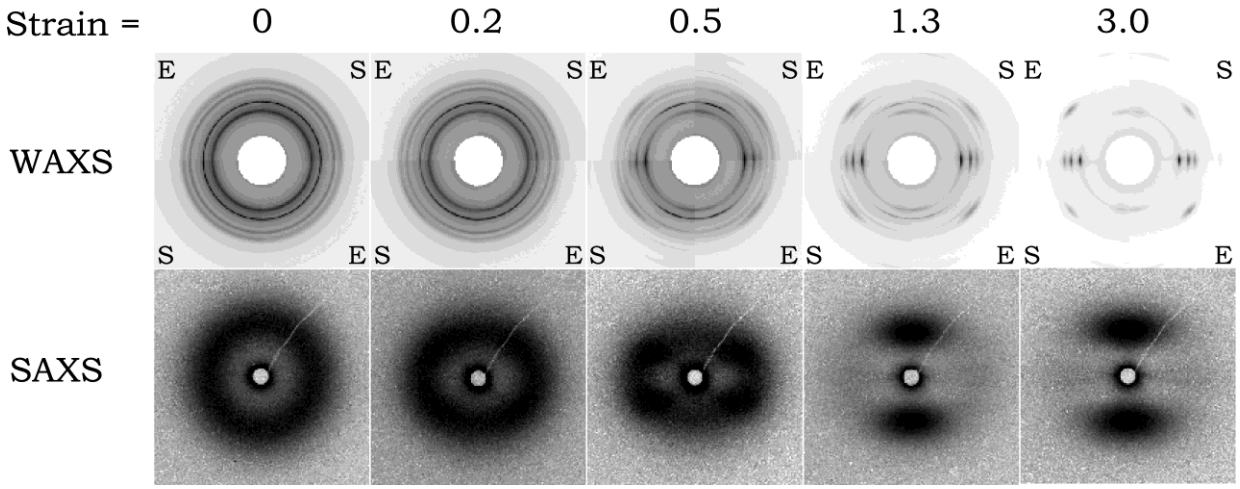

Figure 5-14. WAXS (top row) and SAXS (bottom row) patterns of P-B co-polymer stretched at different strain. Each WAXS pattern shown in the top row is composed of four quarter sections of experimental and simulated patterns, marked with '**E**' and '**S**', respectively in corners.

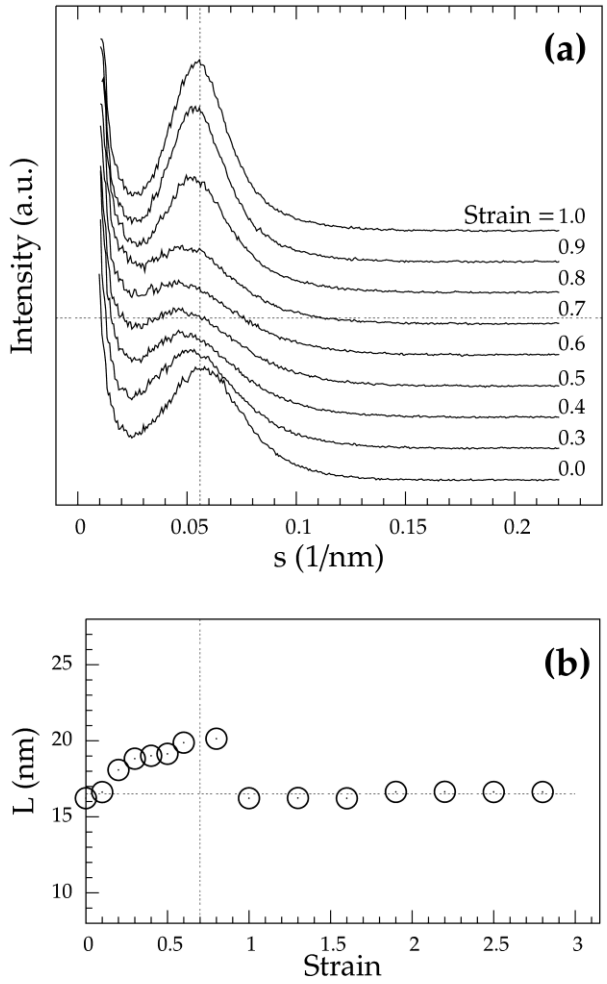

Figure 5-15. 1D SAXS profiles of P-B copolymer being stretched at 100 ^{o}C, at different strain **(a)** and the change of long period derived from **(a)** as a function of strain **(b)**. The 1D profiles are integrated from -20 ^{o} to 20 ^{o}, close to the meridian.

The 1D SAXS profiles were obtained by integrating 2D intensity within $\phi = \pm 20^{o}$ in which meridian intensity is included. Selected 1D profiles at different strains are shown in **Figure 5-15a**. A maximum caused by the interference between lamellae is found in these profiles. When strain < 0.6, the maximum moves toward the lower angle, and the intensity keeps decreasing in the meantime. This is understandable since pre-existed spherulites are destructed by the tensile force, and lamellae are forced to fall apart. The destructed lamellae, together with polymer chains in the neighborhood tend to form microfibril under stretching.[125, 126] Because the temperature is high and polymer chains are mobile enough, these well-oriented fibrils further serve as nucleation sites to induce secondary crystallization. It is this recrystallization process makes the meridian intensity keeps increasing again, and the maximum resumes to the previous

position. The position of the maximum defines the long period. The change of long period as a function of strain is shown in **Figure 5-15b**. In the early stage stretching, long period increases because lamellae are getting more and more separated. The recrystallization makes lamellae become densely packed again (newly grown lamellae); and the long period decreases to the original value.

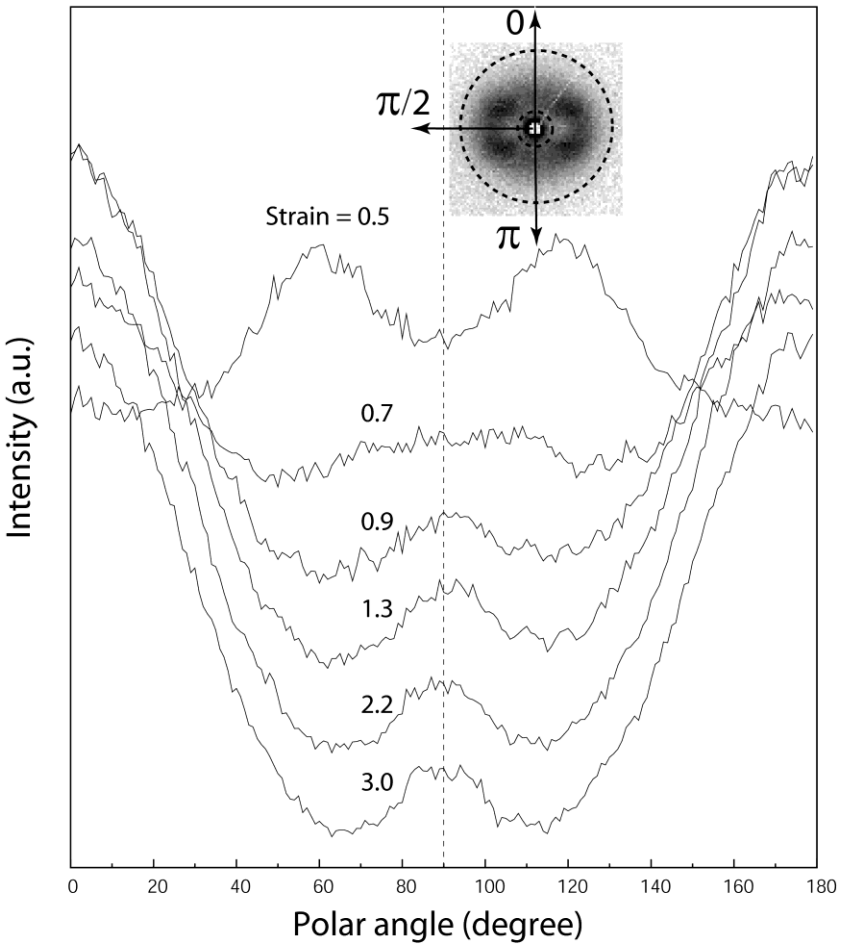

Figure 5-16. 1D SAXS profiles of P-B copolymer being stretched at 100 ^{o}C, at different strain **(a)** and the change of long period derived from **(a)** as a function of strain **(b)**. The 1D profiles are integrated from -20 ^{o} to 20 ^{o}, close to the meridian.

Besides strong intensity in the meridian, additional features can be distinguished in the two-point patterns. That is, two tilted streaks, although very weak, can still be distinguished near the equator. Equator streaks are usually interpreted as rod-like structure oriented along the fiber axis. Intensity distribution in SAXS patterns at different strains over polar angles from 0 to π is shown in **Figure 5-16**; the average scheme is shown in the in-set. Two maxima close to 90 ^{o} when strain = 0.5 are caused by the lobes in the four-point pattern. After that, four-point changes

to the two-point, and the intensity close to the equator begin to increase again. The streaks must have different origin as that of lobes in the four-point pattern. This is because that the former is attributed to the alignment of the γ-phase lamellae with respect to the fiber axis, and ϕ_{008} is eventually fixed at about 20°. While the tilting angle of streaks with respect to the equator is below 10°. Therefore, for stretching experiment, a reasonable explanation is the existence of microfibrils as mentioned before. The streaks become more and more discernible when strain exceeds 0.6. This indicates that the formation of microfibrils starts almost right after the accomplishment of yielding (strain = 0.5). These fibrils may play an important role in the stress hardening in the late stage of stretching.

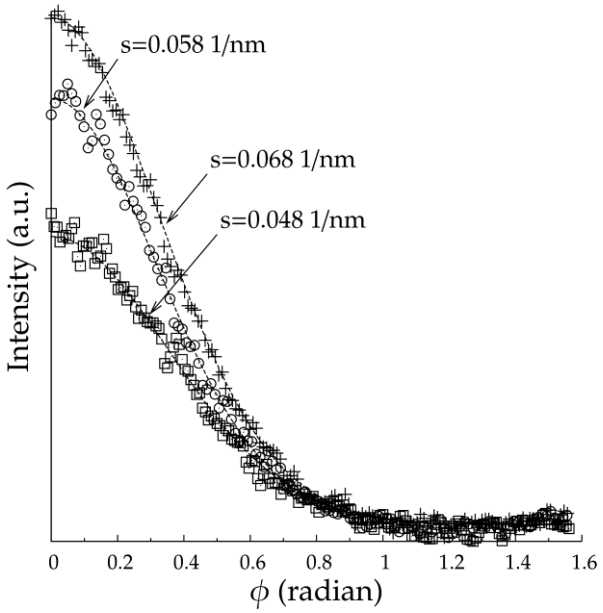

Figure 5-17. An example of polar distributions of intensity at three different *s* positions and corresponding fitting curves obtained using Legendre expansion approach. The strain is equal to 1.0.

In principle one can also calculate lamellar thickness based on 1D profile (see chapter 2). But this step demands for higher order interference peaks. The lattice factor determines the positions of the interference peaks. For stacking layers that are rigorously periodic, the ratio of positions of interference peaks is 1:2:3⋯. The intensity of each peak is determined by the structure factor, or more specifically, by the thickness of one phase. Furthermore, the intensities of higher order peaks are also influenced by disorder effects[127]. That is to say, without higher order peaks, the fitting of 1D profile will not be significant. Therefore, long period is the only

parameter that can be confidently decided through the 1D profiles for current system. This is due to the nature of random copolymer crystallization: the lamellar thickness distribution is broad, and the disorder effect plays an important role in lamellar arrangement[52, 53]. Nevertheless, one can utilize the two-point to examine the orientation and the lateral size of the lamellae. Legendre expansion approach as introduced in chapter 2 can be used to separate these two effects. A fitting example of polar angle dependence of intensity at different s values crossing the bar-like region in the meridian is shown in **Figure 5-17**.

Figure 5-18 and **5-19** exhibit the change of $\langle P_2 \rangle$ and lateral width during stretching; the corresponding values obtained from WAXS measurement are also shown for comparison purpose. In **Figure 5-18**, lateral width derived from SAXS method ranges from around 25 *nm* to 45 *nm*. It increases as stretching proceeds, which is reasonable since recrystallization is going on in the meantime. WAXS line profile analysis can also be used to estimate crystal's size. We use Loritzian distribution to fit diffraction peaks and the reciprocal integral width produces the size in the normal of a given (*hkl*) plane. In principle, one is free to choose any (*hkl*) plane to estimate sizes in different directions. But in reality, special planes with one or two Miller indices being equal to zero are more useful. For α-phase crystal of iPP, we choose (040) plane for calculation since its normal represents the crystal growth direction. It is fairly interesting to find out that during stretching there is no noticeable size change as derived through WAXS method, and the size obtained is around 9 *nm*—much smaller as compared to the lateral widths derived through SAXS method. A plausible explanation to this fact is that a lamella must not be a bulky piece but consists of several mosaic block crystals[128-130]. The boundaries of these blocks define the crystal size in the length scale of WAXS technique; while in SAXS measurement, entire lamella contributes to the intensity distribution in s_{12} direction. There is a lot of controversy as to whether crystallization of semi-crystalline polymer is a one-step nucleation-growth, or a multi-stage process with small, less-ordered mosaic-like crystal block as one of the intermediate state[121, 122, 131]. The discussion of general crystallization mechanism goes beyond the scope of this thesis, but the pattern of lamellae composed of mosaic-like crystal blocks is very reasonable in the stretching experiment, since strong tensile force is applied to the polymer network, and it is likely that intra-lamella slip can be induced.[128-130]

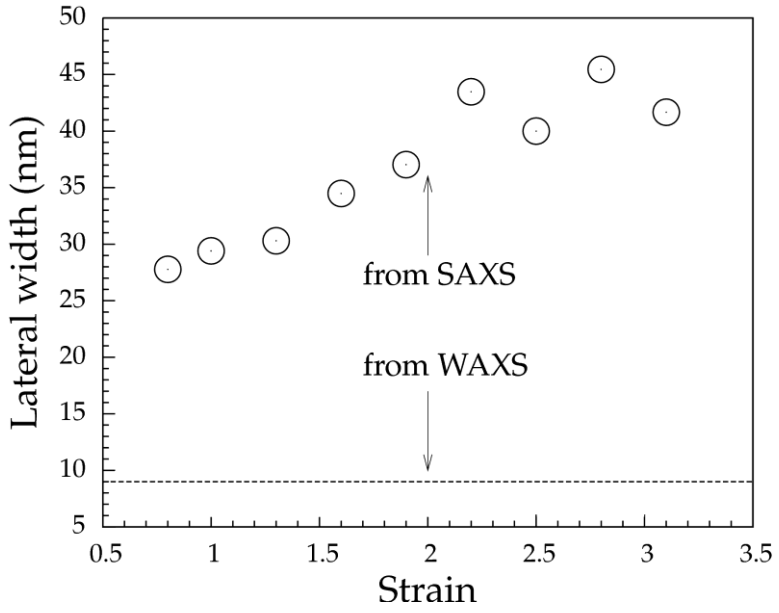

Figure 5-18. Lamellar lateral width change as a function of strain. Hollow circles represent values derived from polar angle distribution of SAXS intensity, as described in the context. The dashed line indicates the estimated value obtained through WAXS line profile analysis.

Figure 5-19 gives a further support to this argument. In **Figure 5-19**, WAXS-generated $\langle P_2 \rangle$ was derived by fitting polar distribution of diffraction intensity using Onsager function.[73, 75] The increase trend is obvious since one can even judge by eyes that the diffraction arcs become more and more narrow during stretching. Eventually, $\langle P_2 \rangle$ is close to 1 in the late stage, indicating polymer chains are almost perfectly aligned along stretching direction. In contrast, $\langle P_2 \rangle$ values derived through SAXS method are systematically smaller than that derived through WAXS method. Polymer chains, or loosely speaking, small crystal blocks are fundamental units that bear the tensile force. Consequently, it is not strange to observe very high degree of orientation in WAXS measurement. However, SAXS only 'sees' the orientation of lamellae; and a lamella can orient not only with respect to the fiber axis, but also can flip around its normal. This decreases the observed value of $\langle P_2 \rangle$. If intra-lamella slip occurs, this effect may be further magnified. Keep this argument in mind, it is also reasonable to observe in **Figure 5-19** that SAXS-generated $\langle P_2 \rangle$ even has a slight decrease as strain increases, as force being applied to the network become stronger and stronger as stretching proceeds, and the intra-lamellar slip (and other disorder effects as describe above) become severe.

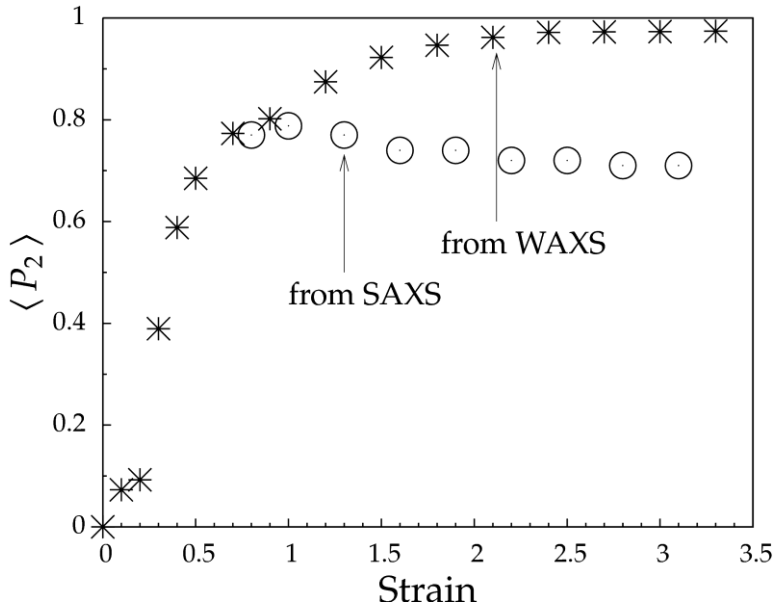

Figure 5-19. The change of Hermans' orientation function as a function of strain. Both values obtained from SAXS and WAXS methods are exhibited.

Considering all these experimental factors, a pattern of the morphology of the stretching-induced texture can be depicted. First of all, the tilted streaks near the equator in SAXS pattern should be coupled with the two-point near on the equator. A simple model for this SAXS pattern is shown in **Figure 5-20b**, the shish-kebab-like structure. In this case, shish-kebabs are not fully aligned to the stretching direction, and the tilted shish which is essentially composed of stretched and entangled polymer chains and possibly some defragmented lamellar crystals accounts for the tilted equatorial streaks. Kebabs are epitaxially grown along shishes, and they contribute to the meridian points. However, if a shish is tilted, kebabs must also tilt accordingly. Given the equal probability of titling at both directions (left and right), the meridian two-point is actually a superposition of four-point, as shown in **Figure 5-20a**. Further evidences support this superposition picture. If the sample is heated to a higher temperature after stretching (partially melted) and then cooled down to the crystallization temperature again (100 ^{o}C), it is found that the two-point becomes more broad. This is because the shish-kebab-like structure is relaxed during heating and the meridian points begin to split. The same experiment can be performed to sample stretched at lower temperatures (e.g., 60 ^{o}C, as will be discussed in detail in chapter 7). In this case, two-point pattern can be relaxed to four-point pattern.

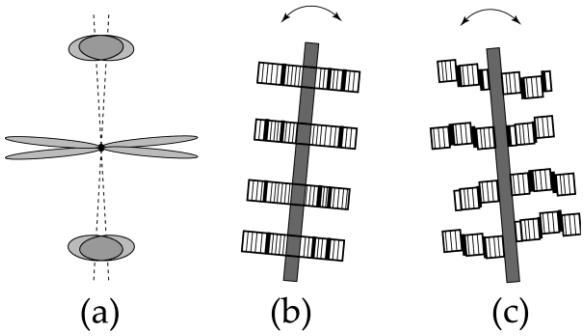

Figure 5-20. An illustration of stretching-induced SAXS pattern **(a)** and possible structures corresponding to it **(b, c)**. Meridian intensity is possible to be a superposition of split points in **(a)**. Each lamella is composed of several small block crystals, as shown in **(b)** and **(c)**. Intra-lamellar slip is also demonstrated in **(c)**.

A further improvement of this model is illustrated in **Figure 5-20c**. In this pattern, intra-lamellar slip of mosaic crystal blocks is also included. Thus, crystal blocks are connected with each other in a flexible way, so that they themselves possess some degree of freedom to orient. This explains why orientation degree derived by SAXS method is smaller. Because that these blocks are basic units (in crystalline portion) to bear the force, and that they are not rigidly connected to their neighbor, each block has a higher degree of orientation as revealed by WAXS.

5.6 The structure-property relationship

With the full sequence of WAXS/SAXS data, the ultimate goal is to correlate the structure development with the stress-strain curve. So far as evolution of scattering pattern is concerned, the early stage, i.e., from the beginning of stretching till the end of yielding, generates the most dramatic change. For semi-crystalline polymer, yielding is closely related to destruction of preexisting spherulites, which is accomplished by inter-lamellar and intra-lamellar chain slip.[123, 132] The former leads to the dissociation of lamellar aggregates in which lamellae are connected by inter-lamellar chains. While the latter accounts for the deformation of a single lamella. Inter-lamellar chain slip is believed to be easier to achieve as compared with the intra-lamellar slip, since it mainly deals with separation of chains in intermediate amorphous layers between lamellae. Therefore a successive occurrence of these two processes is expected.[133] G. Strobl[123] argued that for inter-lamellar slip, polymer chains intend to be aligned in parallel to the equator, whereas chains will be in parallel to the meridian for intra-chain slip. Based on the fact that WAXS patterns in which (*hk0*) arcs were always located near equator, they concluded that

intra-lamellar slip took place in the very beginning of deformation. In our experiment for P-B copolymer, we observed simultaneous occurrence of inter- and intra-lamellar slip processes in the early stage. On the one hand, the (008) arc from the γ-phase moved toward the meridian, indicating that chains become more and more parallel to equator. On the other hand, all (*hk0*) arcs from the α-phase were localized in the equator in the same time. Four-point pattern is the main character in SAXS measurement during this period, with four lobes gradually moving toward the equator. All these facts point to the co-existence of inter- and intra-lamellar slip, with the former mainly undergone by the γ-phase and the latter by the α-phase.

The yield point is an important critical point before which slip takes place individually. After that point, a collective slip process occurs, resulting in a complete destruction of spherulites.[123, 134] This process proceeds all the way through the intermediate stage (the plateau region) by the end of which the system is transformed to a network cross-linked by destructed crystals as well as entanglement in amorphous matrix. Further deformation of this network leads to the final stress-hardening, which can be described using rubber elasticity.[123, 134, 135] The transformation to network can be indirectly evidenced by the facts that the change of parameters related to orientation (P_0, $\langle P_2 \rangle$) slow down after point 1 (see **Figure 5-13**), since after that stress was mainly dispersed in the network rather than crystal skeleton. Another piece of evidence was that the dimensions of the unit cells of the γ-phase crystals were subjected to change in the early stage. **Figure 5-21** shows the change of the *c*-axis length of the unit cells of the γ-phase. It is obvious that most significant change of unit cells' dimension occurs in the early stage. After that, it fixes to a constant value. The elongation of the *c*-axis of the unit cells is expected since for tilted cross-β configuration, stress is applied mostly along the *c*-axis which is the packing direction of polymer chains. We did not observe dimension change of the unit cells of the α-phase crystals. The reason might lie in the fact that polymer chains in this case are parallel to stretching direction, before the deformation of the unit cells, intra-lamella chain slip took place, resulting in a shear angle in α-lamellae.

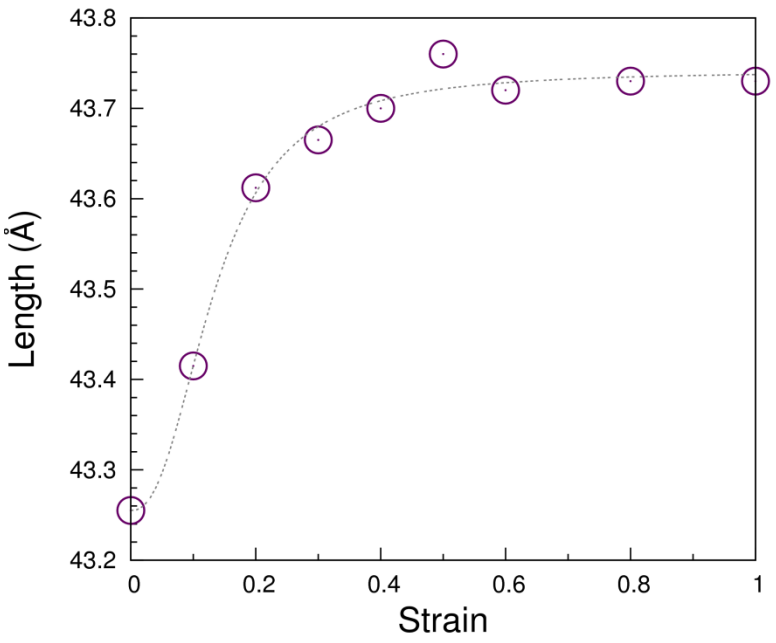

Figure 5-21. Change of dimension of *c*-axis of γ-phase crystal unit cell during stretching.

Another important feature of structure formation during stretching is the fibrillation process which might also contribute to the final stress-hardening. As discussed before, the process takes place in the beginning of the intermediate stage. Also, it can only be evidenced from the SAXS patterns, from two weak streaks near the equator. However, at this point, it is hard to give the details of its nature. The composition of the fibril bundle, as well as molecular mechanism of its relationship to lamellae is not clear at this moment. Melting experiment as will be discussed in chapter 6 offers an opportunity to probe its nature.

5.7 Summary

P-B random copolymer subjected to uniaxial stretching at 100 ^{o}C was studied using time-resolved synchrotron WAXS/SAXS techniques. Two crystal modifications, γ- and α-phase, with three distinctive orientation modes of unit cells were identified during stretching. The γ-phase unit cell adopted a tilted cross-β configuration in which the *c*-axis had a tilting angle with respect to the fiber axis. Polymer chains are piled layer by layer in a cross-hatched way in the *c*-axis direction. The α-phase unit cells had two orientation modes depending on the type of lamella. Unit cells in the mother lamellae had a *c*-axis orientation; polymer chains are in parallel

to the fiber axis. For the daughter lamellae of the α-phase, an *a*-axis orientation in which the *c*-axis had an 80 ^{o} angle with respect to the fiber axis was favored.

The γ-phase was not stable under stretching; its content kept decreasing till the end of experiment. While the α-phase gradually became dominant because of the parallel packing of polymer chains. Structure development can be correlated with mechanical property characterized by the stress-strain curve. It was found that polymer exhibited most dramatic change in WAXS/SAXS pattern near the region of yielding. Inter- and intra-lamella slip processes were observed in the early stage, in a simultaneous manner. SAXS pattern revealed a fibrillation process after the accomplishment of yielding. The fibril bundles, as well as the network as a consequence of continuous application of tensile force, might be responsible for the stress-hardening in the late stage.

6 Melting and Recrystallization

It has been shown that uniaxial stretching is able to drive the crystalline structure of P-B copolymer far from its native state, resulting in completely different polymorphism and morphology. This chapter will focus on the relaxation behavior of this texture. This will be tested by two experiments. First, melting behavior of the pre-oriented sample (as described in chapter 5) will be investigated. Second, the memory effect will be tested by relaxing the pre-oriented sample at higher temperatures, followed by an examination of recrystallization behavior when cooling down. Detailed experimental protocols will be described as follows. The same P-B copolymer was used for this study.

6.1 Experimental procedure

6.1.1 Melting experiment

The P-B copolymer was stretched under 100 ^{o}C with a speed of 6 *mm*/*min* by an INSTROON stretching machine, as described in chapter 5. The final strain was 3.7. After reaching this strain, the machine was stopped and the temperature was lowered down to the room temperature. The spacemen was then unmounted, and its central part was cut and sealed between two Kapton films. The new sealed sample was then mounted back to the INSTRON machine, and the melting process was monitored with a heating speed of 4 ^{o}C/*min* until completely melted. In this case, INSTRON machine only served as the sample holder and the temperature controller; no force was applied to the sample.

6.1.2 Melting and recrystallization

In the late stage of heating, SAXS/WAXS pattern become weak. WAXS pattern disappear at around 130 ^{o}C, and SAXS pattern at around 136 ^{o}C. These evidences will be used to design the up limit of temperature for sample relaxation experiment. The mechanism as to why WAXS and SAXS pattern disappear at different temperatures will be discussed in detail in the relevant parts of the following context.

Experiments are grouped into two sets. In one set, three temperatures that are close to the melting temperature, namely, 128 ^{o}C, 130 ^{o}C and 132 ^{o}C are chosen to largely iron out the preexisting structure. The other experiment is performed by annealing the sample at a lower temperature, namely, 122 ^{o}C to partially melt the sample. The procedure can be found in **Figure 6-1**. The pre-oriented sample was first heated to 122 ^{o}C, with a heating rate of 4 ^{o}C /*min*. It was kept at this temperature for 1 *min* and then cooled down to 100 ^{o}C again. The isothermal crystallization at 100 ^{o}C is the main goal for this study (although scattering patterns were recorded for both heating and cooling process, as will be shown later). The cooling rate was 6 ^{o}C/*min*, and was determined by the limit of air-cooling system. The sample was heated again to the next higher temperature after a 20 *min*'s annealing at 100 ^{o}C when isothermal crystallization was fully accomplished, and the same process will be performed for all remaining temperatures as illustrated in **Figure 6-1**.

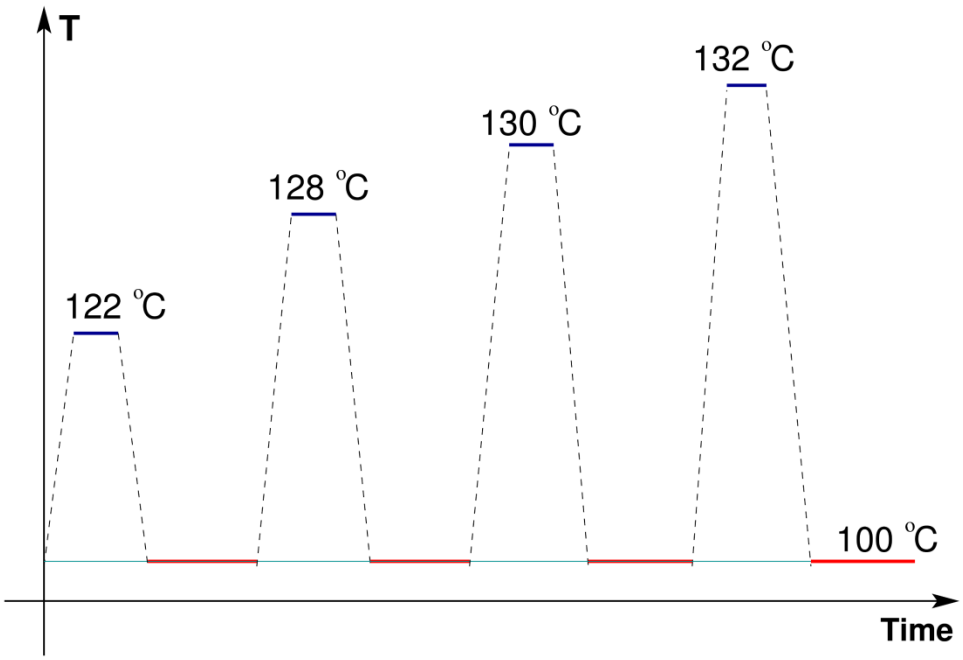

Figure 6-1. A schematic of procedures of relaxation-recrystallization experiment.

6.2 Structure development during melting

An overview of the entire melting process can be found in **Figure 6-2** where a spectrum of WAXS and SAXS patterns at different temperatures during heating are shown. The change of WAXS patterns is as expected: diffraction arcs become weaker and broader and the amorphous

halo gradually becomes visible, because crystals are being melted away. The development of SAXS patterns is more interesting. The main features are as follows. First of all, it is observed that two meridian points move toward lower scattering angle during heating. This can be understood since accompanying with the melting away of smaller lamellar crystals, the average distance (long period) between existing lamellae is expected to be larger. Second, it seems that two tilted streaks close to the equator become more and more visible (actually there is a certain period during which the intensity of two meridian points also increases, but this is not easy to judge by eyes). This is somehow counterintuitive, since melting process means less scatterers can survive and, in general, a decrease of the scattering intensity is expected. We will go back to this paradox later. Finally, it is found out that SAXS pattern can survive at higher temperature. At 130 ^{o}C, diffraction peaks in WAXS has already been very weak, but the SAXS intensity is still considerably strong. When the temperature arrives 134 ^{o}C, only amorphous halo is visible in the WAXS pattern, while the main features, i.e., the two points and tilted streaks still exist, although weaker, in the SAXS pattern.

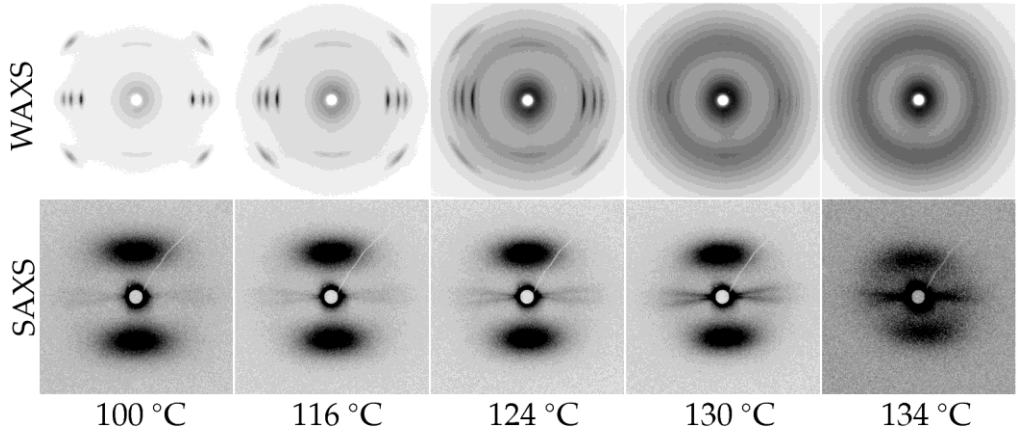

Figure 6-2. Selected WAXS and SAXS patterns at different temperatures during heating.

We tried to quantify the melting process, and the result is shown in **Figure 6-3**. The dependent variables in **Figure 6-3a** and **6-3b** are closely related to the concept of invariant in the scattering theory. For cylindrical system (fiber symmetric), an invariant, Q, no matter it is in WAXS or SAXS measurement, is defined as

$$Q = \int_0^{\pi} \int_0^{\infty} I(s, \phi) \sin\phi \, s^2 \, \mathrm{d}\phi \, \mathrm{d}s \qquad \textbf{(6.1)}$$

Crystallinity is obtained by dividing the invariant from all diffraction peaks by the overall invariant (i.e., invariant contributed by amorphous and crystalline portion).

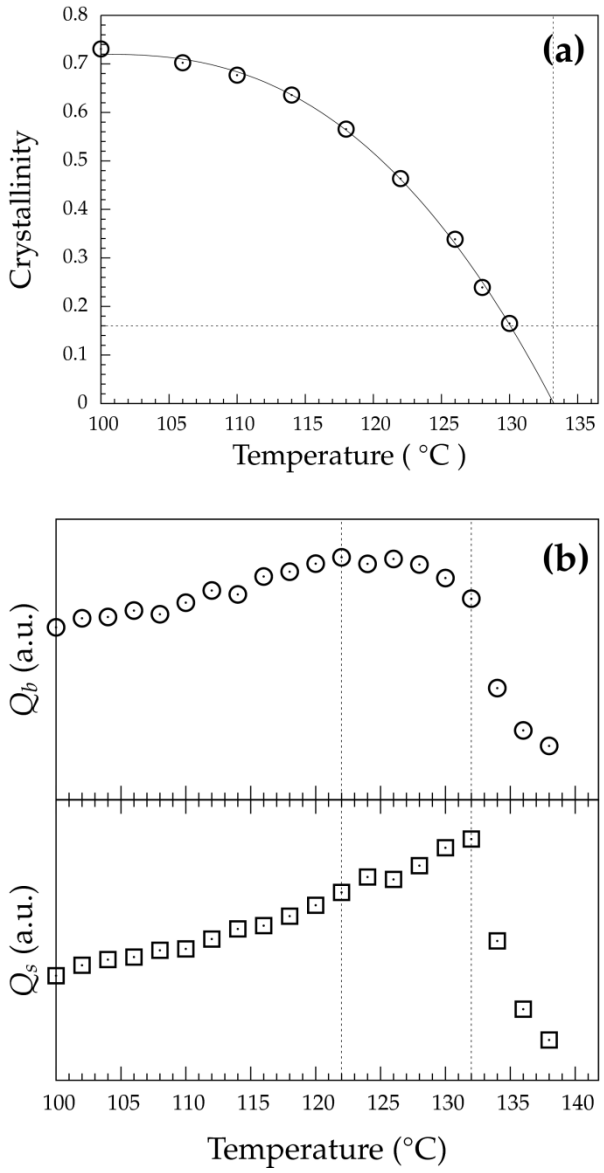

Figure 6-3. Change of crystallinity (calculated from WAXS data) **(a)** and scattering invariant **(b)** as a function of temperature during heating. Plot **(b)** shows invariant integrated within regions of the meridian point (Q_b) and the streak that is slightly tilted from the equator (Q_s).

The maximum *s* value in crystallinity calculation shown in **Figure 6-3a** is 0.41 $Å^{-1}$ below which all significant reflections can be included. Q_s and Q_b in **Figure 6-3b** refer to invariants from equatorial streaks and meridian points, respectively. They are not the invariant in the true sense because of the integration limits, but simply represent the scattering power in the given regions. In **Figure 6-3a**, following the trend of the crystallinity change, we can extrapolate the data points

to zero crystallinity where the temperature is about 133 ^{o}C. Seen from **Figure 6-3b**, there are still some scattering contributed by meridian points and tilted equatorial streaks in the SAXS pattern, although they have been decreased significantly. Since WAXS only 'sees' structures in the chain segment's level and SAXS in the lamellar length scale, the longer lifetime of SAXS pattern indicates that melting of lamellae is not a continuous process, i.e., polymer chains are not melted and diffused into the amorphous matrix in the same time. Heating first destroys the coherence of crystal lattice, but these polymer chains are still restricted within the original boundary, or more specifically, in lamellar layers. This causes the disappearance of the diffraction peaks in WAXS but some visibility of scattering intensity in SAXS, since regions composed of these 'molten' chains still have some density contrast as compared with the amorphous matrix. However, this state cannot last long, the whole region will collapse in the equilibrium state where the system becomes homogeneous; and even SAXS scattering will completely disappear.

Figure 6-3b can give us some insights of the morphology of stretching-induced structure. It turns out that both Q_s and Q_b first increase and then decrease during heating. To explain this, we should first interpret the origin of the meridian points and the tilted equatorial streaks in SAXS patterns. The former is generally assigned to layered structure with the normal be in parallel to the stretching direction. In our case, it is the alternation of lamellar crystal and amorphous matrix that produce the density variation, and hence generates the meridian intensity. According to Babinet's principle, two complementary structures generate the same scattering pattern, and the SAXS pattern alone cannot distinguish lamellae and amorphous matrix. The invariant for two-phase system is related to the density contrast, $\Delta\rho$, as well as volume fraction of one phase φ_1, by[136]

$$Q \propto \Delta\rho\, \varphi_1 (1-\varphi_1) \qquad \textbf{(6.2)}$$

It is the $\varphi_1 (1-\varphi_1)$ term that explains the parabolic behavior of meridian intensity, since during heating the fraction of crystal phase decreases monotonically. The origin of the streaks needs more consideration. The question is two-fold: what produces the streaks and why they are tilted. An SAXS equatorial streak can be generated by any long and thin entities, including void, fibril bundle, sharp edge, etc., with their long axes vertically aligned. Possibility of void should be seriously considered in material stretching experiment, as stress-induced whitening frequently

occurs. We did observe this phenomenon in lower temperature stretching, but not at the high temperature. The sample was still transparent in the very late stage of stretching. Furthermore, voids usually produce very large density contrast, as its density is almost negligible. Therefore it usually leads to very strong streak, which is not true for our case. Also, void-induced streak can explain neither the increase nor the decrease of the scattering intensity. Inappropriate sample mounting may cause X-ray beam incident on the sample's edge, producing very strong equatorial streak. This can also be excluded based on the same argument. We therefore believe that the streaks in our SAXS patterns originate from the 'real structure', the microfibrils. And these fibrils must be coupled with lamellae. Oriented fibrils provide ideal nucleation sites for chains to attach to. In the late stage of stretching (the crystallinity is around 70% as indicated by **Figure 6-3a**), each fibril is surrounded by densely packed lamellae, making it not visible to SAXS. As the melting away of lamellae proceeds, fibrils become more and more 'naked'—the very reason that streak intensity keeps increasing. Careful examination of **Figure 6-3b** also tells us that the turning point of Q_b comes early as compared with that of Q_s. Q_b starts to decrease at around 122 ^oC while Q_s has been increasing till 132 ^oC. This further suggests that the strengthening of meridian points and streaks stems from different mechanisms. The increase of meridian intensity is due the nature of two-phase model, it begins to decrease once the fractions of the two phases fulfill an inversion. But it has no influence on the change trend of Q_s. As long as surrounded lamellae are being melted away and the bundles can still maintain their shapes, Q_s will continue to increase. 132 ^oC is the temperature where both Q_s and Q_b suffice a dramatic drop. For Q_b, this is corresponding to the collapse of lamellae (remember WAXS pattern almost has no visible diffraction peaks at this temperature). In the same way, microfibrils cannot maintain their shape and begin to diffuse into the matrix.

What are those microfibrils made of? Are they extended crystals? Not likely. On one hand, diffraction peaks disappear earlier, indicating the vanishing of crystals, whereas extended chain crystals should be much more thermodynamically stable. On the other hand, as discussed above, microfibrils begin to diffuse into the matrix almost in the same time with the collapse of lamellae. This gives us a hint that surrounding of lamellae might be crucial to microfibrils' topological property. They might play a role of 'clamps', restricting bundles in a confined space. That said, we intend to consider microfibrils as tightly aggregated polymer chain bundles,

extended, but twisted and entangled as well, and hence is not crystallizable because of those defects and geometrical confinement.

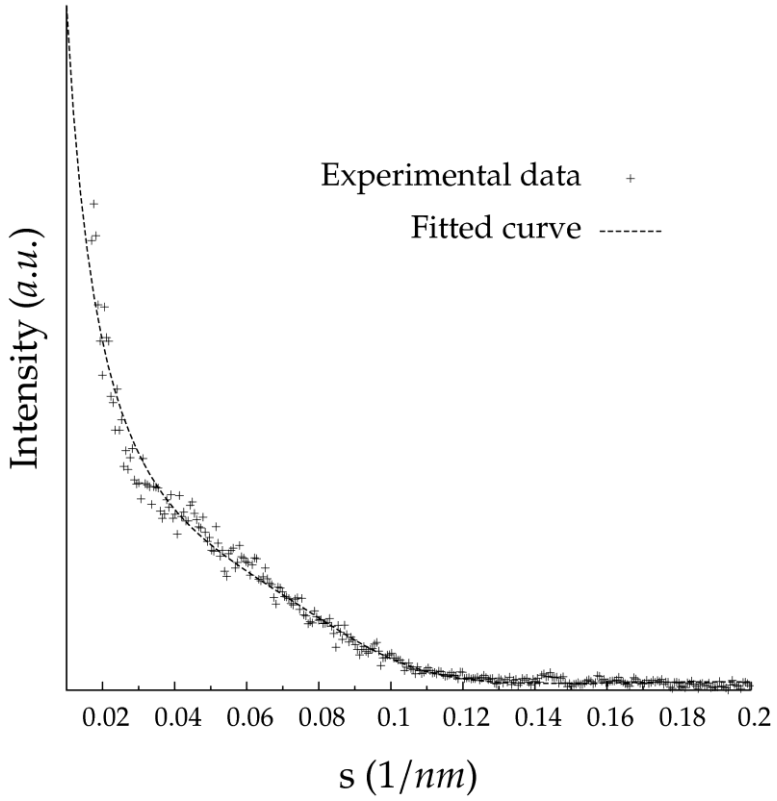

Figure 6-4. An example of fitting the tilted equatorial streak profile using 2D hard-disk model.

Since the streaks are strengthened during heating, this gives us a chance to do further analysis. The average diameter of microfibrils can be calculated using the 1D profile of the streak. Since microfibrils are well oriented, the 1D profile can be modeled using 2D hard-disk model. In this case, the form factor is related to Hankel transformation which is essentially the 2D Fourier transformation for system with circular symmetry[137]. For perfectly oriented long cylinder with radius of R, the form factor is

$$|F(s)|^2 = [RJ_1(2\pi Rs)/s]^2 \qquad \textbf{(6.3)}$$

where J_1 is the Bessel function of the first kind. Considering the asymptotic behavior due to orientation, another s should be divided in **Eq.(6.3)**. The final expression of 1D intensity profile reads

$$I_{1D} = S(s) \cdot [RJ_1(2\pi Rs)]^2 / s^3 \qquad \textbf{(6.4)}$$

where *S(s)* is the structure factor due to inter-fibril interference. We use 2D Percus-Yevick hard-disk model to calculate the structure factor and the details can be found elsewhere.[138, 139] **Figure 6-4** demonstrates a fitting of experimental 1D SAXS profile from a tilted streak using the model just described. The calculated diameter is about 8 *nm*. Since there are only three frames of images that have quality good enough for such fitting, we cannot have the change trend of diameter of microfibrils during heating. Nevertheless, the calculation gives us an estimation that the diameter of the microfibrils are in the same order of magnitude as the size of block crystals.

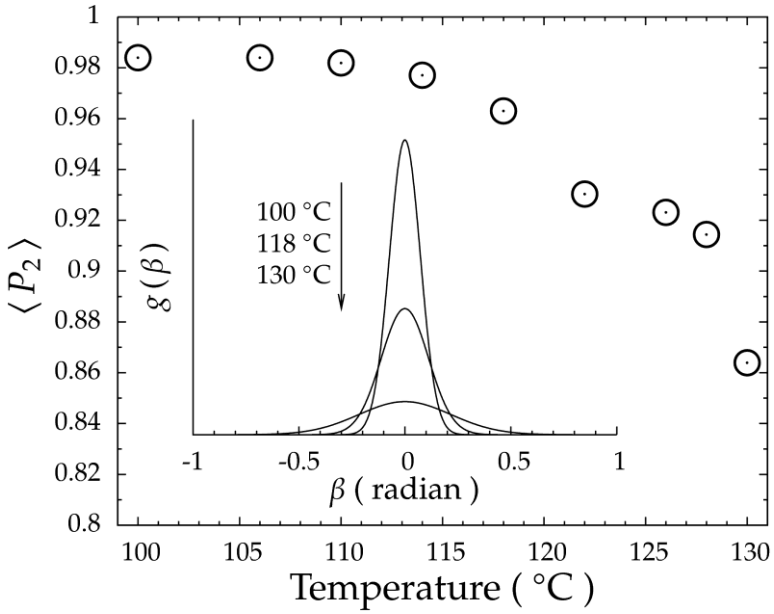

Figure 6-5. Hermans' orientation function (derived from WAXS data) change as a function of temperature during heating. The in-set shows orientation distributions function in real space at three typical temperatures.

The melting process as discussed so far provides us a chance to look back at the morphology induced by stretching at high temperature. After the destruction of original texture (spherulites in amorphous matrix), some chains are stretched into bundles that can serve as nucleation sites for further crystallization, forming the shish-kebab-like structure, featured with central fibrils and epitaxially grown lamellar crystals. What's unique for this structure that is different from conventional pattern of shish-kebab generated by step-shear of polymer melt or stirring of polymer solution is that lamellae may be dislocated due to intra-lamellar slip. Thermodynamically speaking, melting is a first-order phase transition, one expects to observe a

discontinuous change of parameters such as density. In polymer crystallization, very often lamellae have a broad spectrum of size distribution, that's the reason we observe gradual change of SAXS/WAXS pattern in **Figure 6-2** and **6-3** that lasts to the very late stage of melting. The fact that SAXS patterns can survive longer suggests a two-step melting: vanishing of lattice coherence followed by a collapse of entire lamellar boundary. This can be further evidenced in **Figure 6-5** and **6-6**. **Figure 6-5** is the change of Hermans' orientation function derived by WAXS method as a function of temperature. The in-set shows the orientation distribution functions in real space at several typical temperatures. The key point in this plot is that even at the very late stage, the remaining lamellae still maintain very high degree of orientation, which again suggests that crystal melting and chain diffusion into amorphous matrix is not a simultaneous process: chains are melted within the envelope of lamellar boundary as the first step.

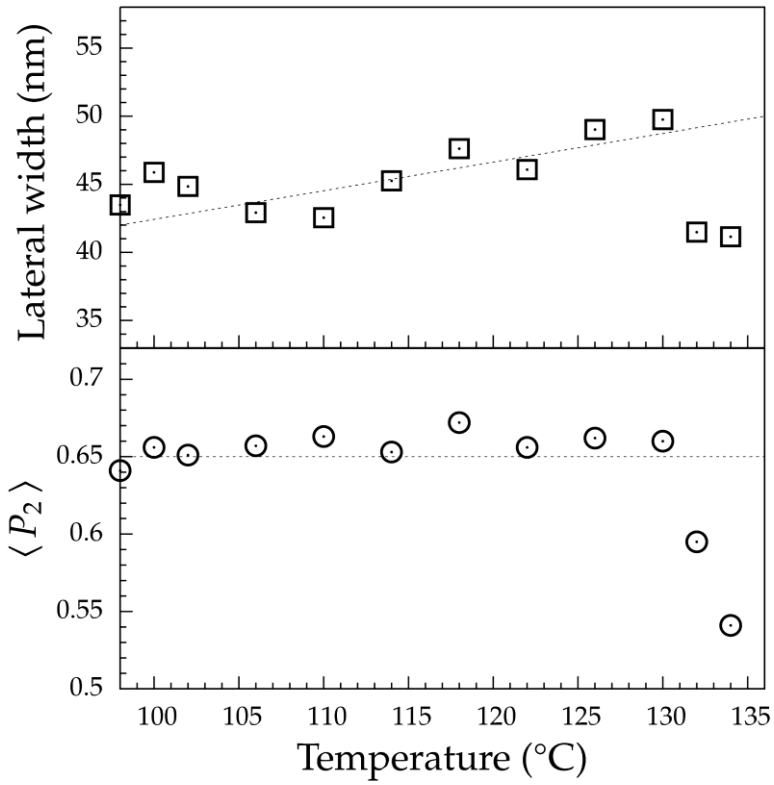

Figure 6-6. Change of lamellar lateral width and Hermans' orientation as a function of time during heating. Lateral width and Hermans' orientation function shown are derived from polar distribution of intensity in SAXS data.

Parameters in **Figure 6-6** are derived in the same way as described in stretching experiment section, i.e., fitting polar distribution of SAXS intensity using Lengendre expansion

approach. The behavior of Hermans' orientation function of lamellae is different from that of polymer chains as seen from WAXS data. It keeps unchanged at a certain level until the very late stage of melting (around 130 ^{o}C) and then suffices an abrupt drop. Besides the sudden drop, the change of lateral size of lamellae is also slightly different. It increases a little before dropping. This increase is not caused by increase of crystal size, but because of melting away of small crystals, making the apparent average size larger. Above discussion convinces us the usefulness of detailed analysis of the melting process. Advanced analysis of combined WAXS/SAXS data not only can reveal melting behavior itself, but can provide additional structural information at hierarchical length scales.

6.3 Testing the memory effect

The pre-oriented sample (stretching terminated at strain = 3.71) is mainly composed of the α-phase crystals (90%, relatively, see **Figure 5.12**), with almost perfect orientation as revealed by WAXS (see **Figure 5.13**). If the oriented crystals are not completely melted away, the survived ones can serve as seeds for heterogeneous crystallization if the temperature is lowered. This effect can be clearly seen from **Figure 6.7**. The first row in **Figure 6.7** shows WAXS patterns of pre-oriented sample annealed at higher temperatures. As temperature increases, diffraction arcs become weaker and broader. γ-phase is thermodynamically less stable, and it is completely melted, as no (117) arc is noticeable in all these patterns. The second row shows WAXS patterns obtained after the sample is cooled down to 100 ^{o}C, and the recrystallization is finished. Melting at lower temperature favors higher orientation degree of newly grown crystals. For the sample melted at 132 ^{o}C, newly grown crystals are almost randomly oriented, as can be seen from the almost isotropic WAXS pattern.

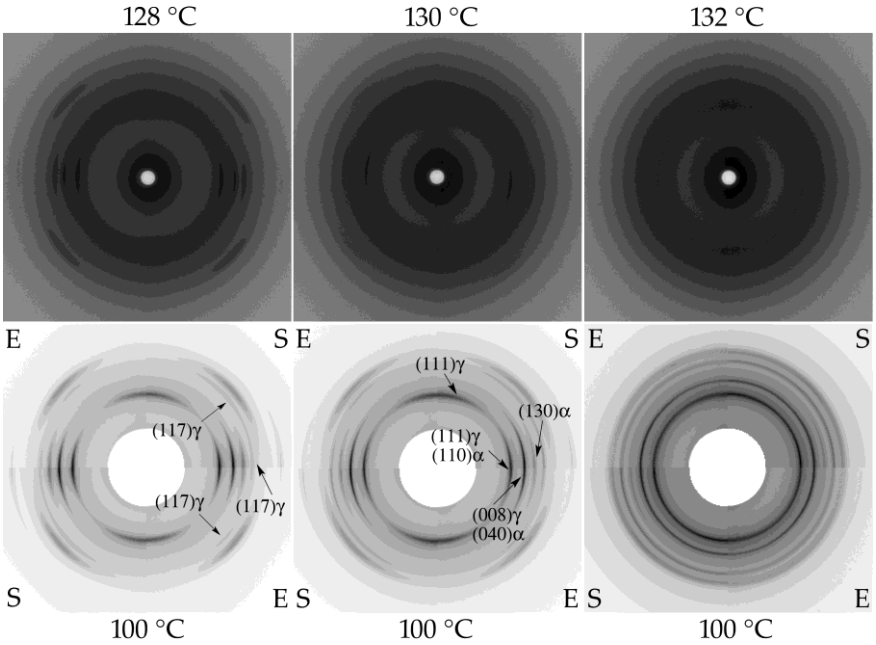

Figure 6-7. WAXS patterns of pre-oriented P-B copolymer melted at different temperatures (the first row) and crystallized at 100 ^{o}C for 20 *min* after cooled down from higher temperatures (the second row). Patterns in the second rows are a recombination of experimental and simulated data (see similar figures in previous chapters for detail).

Newly grown crystals are mainly γ-form (quantitative analysis will be shown later), as evidenced from the appearance of (117) arcs. Furthermore, the off-axis (008) arcs disappear, and the γ-phase adopts a diagonal orientation. It has been discussed in chapter 4 (**Figure 4-5**) that a characteristics of diagonal is the split of (11l) into three arcs, with one of them locating on the equator. This is true for γ-phase crystals grown from partially melted matrix. This can be seen more clearly in the ϕ-dependence of scattering intensity of the (117) arc, as shown in **Figure 6-8**. The formation of the diagonal orientation is due to a compromise. On one hand, existing oriented crystals provide facets for heterogeneous nucleation, and the new crystals prefer to show the same type of orientation. For the relaxation-recrystallization experiment, α-phase crystals with the *c*-axis orientation serves as nuclei. In this case, new chain segments tend to parallel packed to the existing segments in crystals (vertically oriented). Since chain arrangement in the γ-phase unit cell adopts a non-parallel packing style (four layers cross-hatched), a compromise is fulfilled so that two layers are aligned to the existing facets, and the other two has an about 80 ^{o} angle with respect to it. Be sure that 80 ^{o} is the angle between two cross-hatched chains/layers (diagonals of the *ab*-plane).

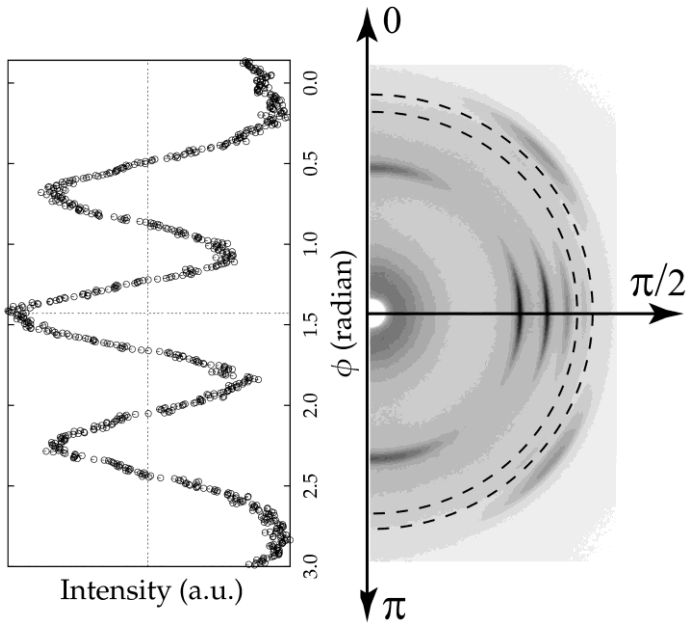

Figure 6-8. Polar scan of (117) arc in the WAXS pattern crystallized from the sample melted at 128 ^{o}C.

So far three orientation modes of γ-phase have been identified for crystallization of P-B copolymer induced by external force field, stemmed from different origin. Cross-β configuration with the fiber axis being perpendicular to the shear flow was observed in shear-induced crystallization, owing to the rotational component of shear flow. Tilted cross-β configuration with the PA being in parallel to the fiber axis (parallel orientation) was observed for stretching-induced crystallization at high temperature, caused by the deformation of polymer network. This diagonal orientation is due to the heterogeneous nucleation of γ-phase on the oriented α-phase substrates. The nature of heterogeneous nucleation determines that crystallization kinetics will also be enhanced.[115-117, 120] This can be seen from **Figure 6-9**. Even for the sample melted at 132 ^{o}C where orientation is very low, the crystallization speed, as well as crystallinity is greatly increased, as compared with the static crystallization process. Lower temperature melting makes the recrystallization even more fast, so that crystallinity has already accumulated to a certain amount (12% for sample melted at 130 ^{o}C and 18% for that at 128 ^{o}C) when reaching 100 ^{o}C, which means crystallization has already taken place during cooling.

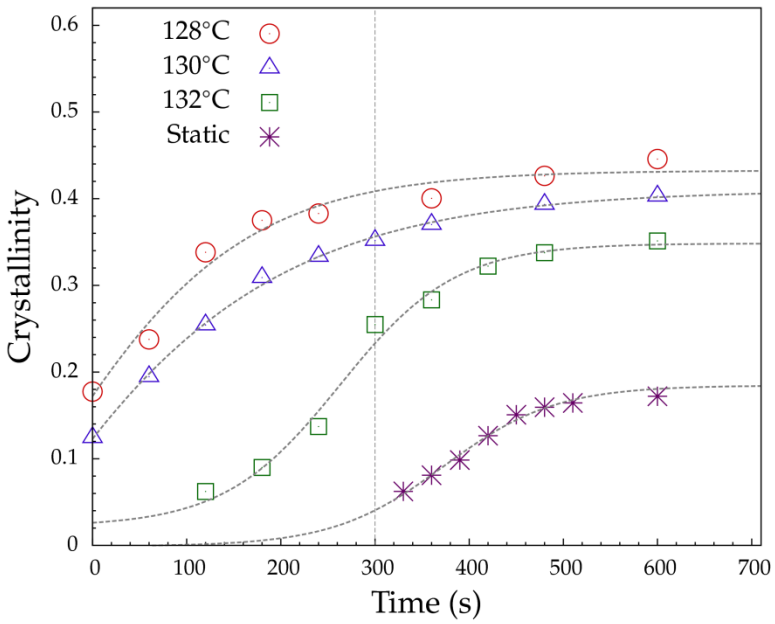

Figure 6-9. Crystallinity change as a function of time during the crystallization of P-B at 100 °C, after being melted at different temperatures (128 °C, 130 °C and 132 °C). Data from quiescent crystallization is also shown for comparison purpose.

Without the presence of strong tensile force, γ-phase will become the dominant modification again. α-form crystals only offer surface to enhance the crystallization kinetics, but cannot change the habit of chain packing in unit cell. The preference of forming γ-phase is determined by the nature of chain defects. α-phase is thermodynamically most stable among all crystal forms of iPP. It follows the classic picture of chain folding to grow into lamellae, with the *b*-axis being the direction of crystal growth (see **Figure 3-1** in chapter 3). The existence of chain defects, crystallization via continuous chain folding becomes difficult, as the newly entered (into a lamella) segments may not match the crystal growth front. Comonomer in random copolymer is an obvious type of defect, as it belongs to a complete different species. Other type of defects, such as disorder in stereo-regularity and region-regularity formed during polymerization by using different catalysis mechanism may generate the same phenomenon.[140-145] The packing energy between α- and γ-phase is close, but the γ-form crystal is less relied on chain-folding mechanism, as can be seen from its chain packing style, the cross-hatching.

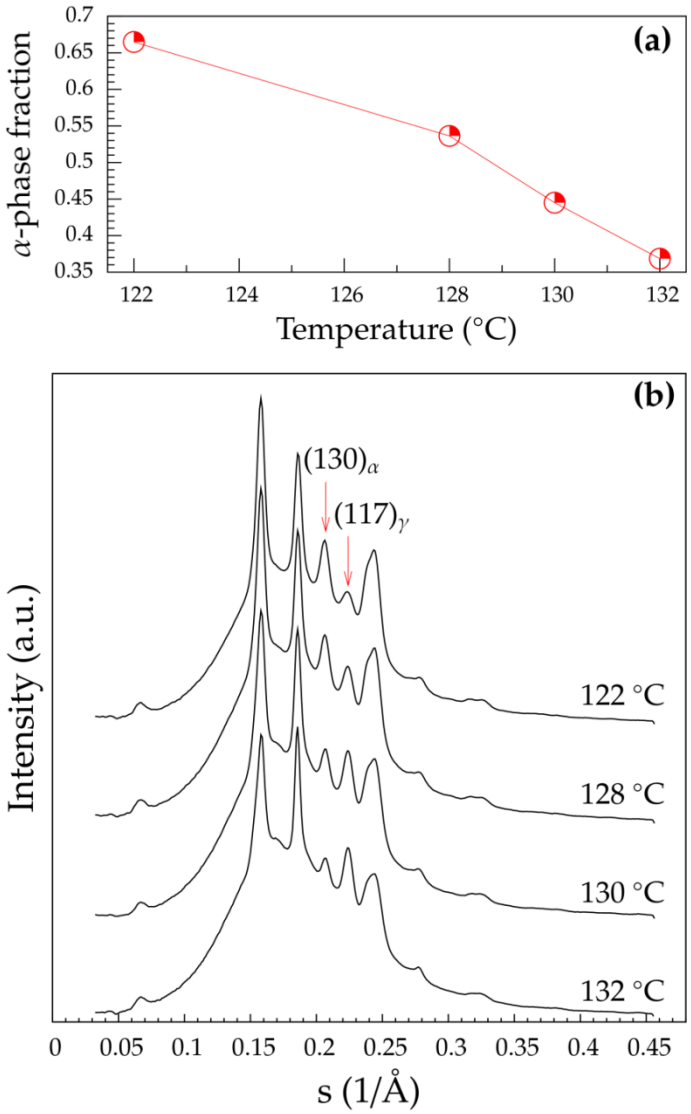

Figure 6-10. Relative fraction of the α-phase in P-B copolymer crystalline after melting at different temperatures and then crystallized at 100 oC **(a)**; Corresponding 1D diffraction profiles are shown in **(b)**.

Figure 6-10b shows final 1D diffraction profiles of P-B copolymer after being melted at different temperatures and then crystallized at 100 ^{o}C for 20 *min*. The ratio between α- and γ can be clearly judged from the strength of $(130)_{\alpha}$ and $(117)_{\gamma}$, respectively. The more pre-oriented α-phase is melted away, the more γ-phase is newly generated. As shown above, at 132 ^{o}C, preexisting α-phase is almost completely erased. In this case, the final content of the γ-phase is about 35% (**Figure 6-10b**) which is very close to the value when P-B copolymer is crystallized quiescently (see the in-set in **Figure 5-12**).

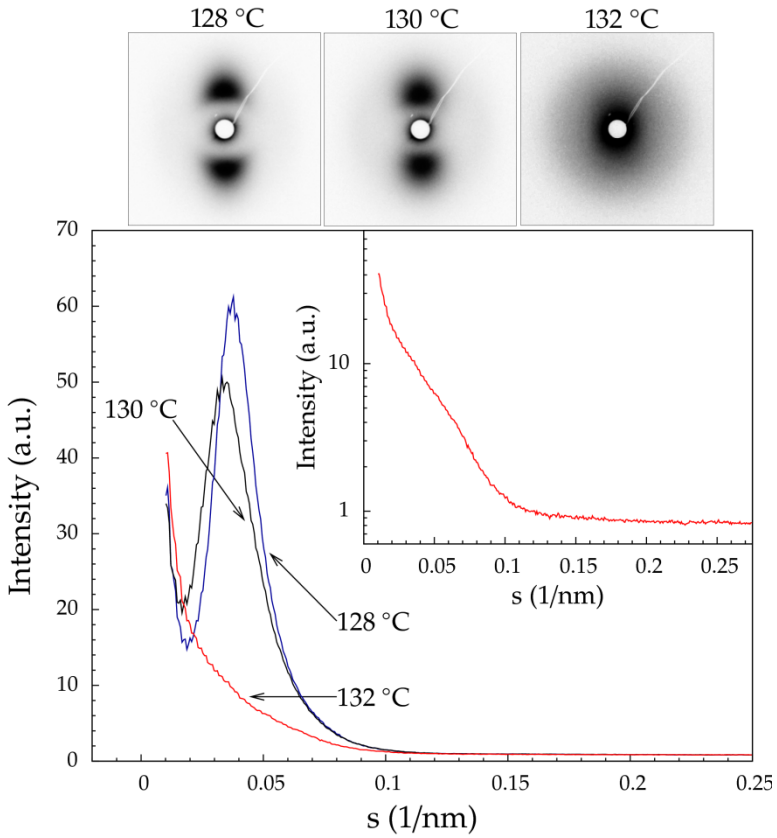

Figure 6-11. 1D SAXS profiles of P-B copolymer melted at different temperatures and then crystallized 100 °C for 20 *min*. The in-set shows the 132 °C curve, in a logarithmic scale. Corresponding SAXS patterns are shown on the top.

The morphology of newly grown crystalline is also controlled by the temperature for melting. **Figure 6-11** shows the final SAXS patterns when crystallization is finished after melting at 128 °C, 130 °C and 132 °C and then cooled down 100 °C. The 1D scattering profiles integrated from the meridian region is also shown. Sample melted at 128 °C and 130 °C show similar patterns, but the interference maximum of the latter is located at smaller scattering angle, corresponding to larger long period (inter-lamellar distance). This is because less oriented nuclei are survived at higher temperatures, and hence the nucleation density is smaller, resulting in a larger distance of separation of two lamellae. The long periods obtained at 128 °C and 130 °C are about 25 *nm* and 30 *nm*, respectively. Compared to **Figure 5-15** in chapter 5, these values are about two times larger than that obtained in the late stage of stretching. Considering that in this case, the crystallinity is only about a half as that induced by stretching (see **Figure 5-11** and **Figure 6-9**), the larger long period becomes understandable. This further confirmed that crystallization mechanism in this case is dominated by heterogeneous nucleation (as compared

with the homogeneous crystallization from the amorphous matrix).[146, 147] As the temperature for melting goes even higher, preexisting structure has been largely erased, the newly grown lamellae show very weak correlation. This can be seen from the 1D profile and the SAXS pattern of the sample melted at 132 ^{o}C.

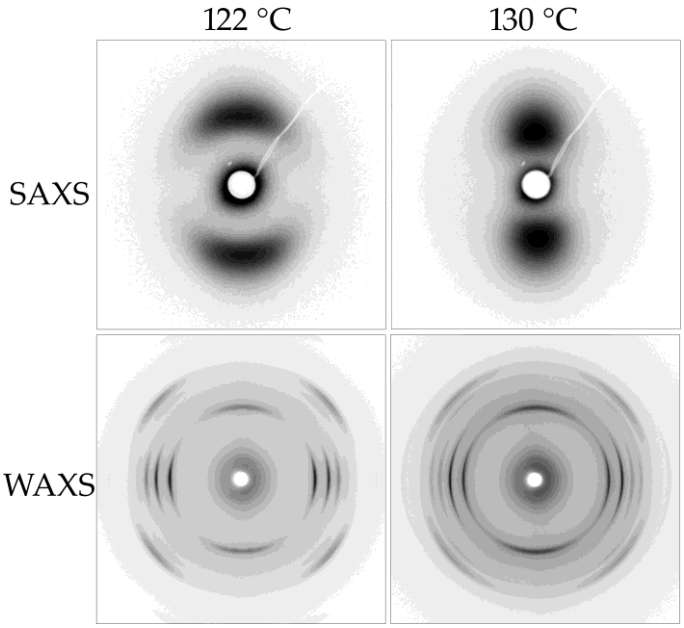

Figure 6-12. SAXS(top) and WAXS(bottom) patterns of P-B copolymer melted at 122 ^{o}C and 130 ^{o}C and then crystallized at 100 ^{o}C for 20 *min*.

Above results are from the sample melted at high temperatures that are close to the melting point where preexisting texture is largely erased. For partially melted sample (melted at lower temperature, 122 ^{o}C), the general trends of changes of polymorphism, preferred orientation, long period are the same, and hence will not be repeated here. However, an interesting point is found when comparing SAXS/WAXS patterns of samples crystallized from partially melted matrix (melted at 122 ^{o}C) and largely melted matrix (say, 130 ^{o}C for example), which is shown in **Figure 6-12**. The WAXS patterns are as expected. Partially melted sample shows higher degree of orientation, as preexisting oriented crystals are less relaxed. However, it seems that the SAXS patterns are counterintuitive, as the pattern obtained from the sample melted at 122 ^{o}C shows a broader intensity distribution over the polar angle; while that from the sample melted at 130 ^{o}C exhibits a typical narrow two-point pattern.

This apparent discrepancy can be reconciled by quantitative analysis of ϕ-dependence of scattering intensity (the $I(\phi) \sim \phi$ plot) in both SAXS and WAXS patterns, as shown in **Figure 6-13**. For SAXS pattern, the $I(\phi) \sim \phi$ is obtained at s = 0.0483 nm^{-1} and s = 0.0345 nm^{-1} for samples melted at 122 °C and at 130 °C, respectively, corresponding to maximum positions in the $I(s) \sim s$ plots (see **Figure 6-13a**). For WAXS patterns, $I(\phi) \sim \phi$ plots represent the distribution of the (008) γ (or (040) α) where s =0.19 Å^{-1} (see **Figure 6-13b**). Intensities for all curves are normalized to the same reference so that their breadth can be compared conveniently. In **Figure 6-13b**, profile of sample melted at 130 °C shows a broader distribution; and the reason has been explained before. Both curves can be fitted by using integral kernel derived from a single Onsager distribution (**Eq.(2.18)**), and the generated $\langle P_2 \rangle$ values are 0.92 for sample melted at 122 °C and 0.84 for that melted at 130 °C.

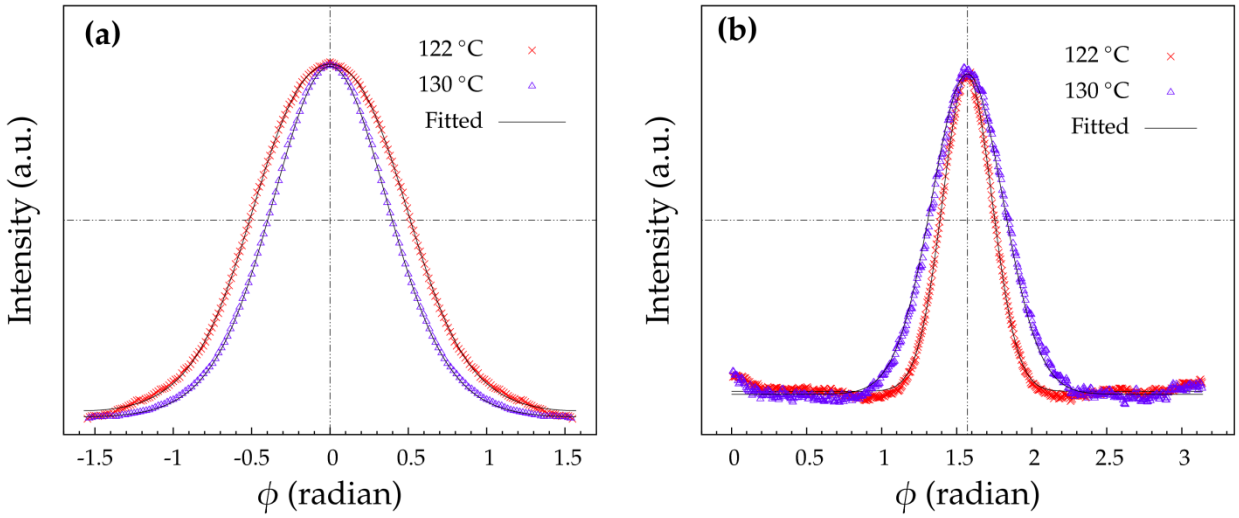

Figure 6-13. ϕ-dependence of SAXS **(a)** and WAXS **(b)** intensity obtained from patterns shown in **Figure 16-12**. Detailed description can be found in the context.

The situation of SAXS profiles needs more careful analysis. As a general approach, oblique orientation is considered with an additional fitting parameter, the oblique angle β_0 (the detail of fitting can be found in chapter 2). It is equivalent to parallel orientation when β_0 = 0. The nonlinear fitting generate a $\langle P_2 \rangle$ of 0.83 for sample melted at 122 °C and 0.74 for that melted at 130 °C. β_0 =18.9 ° and zero for both cases, respectively. Therefore the apparent broader distribution of the sample at lower temperature is due to the superposition of two sharper

distributions, with an oblique angle of about 20 ^{o}. With this consideration, the trend of change of orientation degree is consistent for both SAXS and WAXS pattern. That is, lower temperature for melting preserves more oriented texture and induces higher orientation for newly grown crystals.

The reason for the fact that the orientation degree that is derived from WAXS is systematically higher than that derived from SAXS has been explained before (see chapter 5). A reasonable question about the fitting process is that since the peak breadth is determined by size effect as well as the orientation (see chapter 2), would it be possible that the broader profile in **Figure 6-13a** is because of smaller lateral size of lamellae and a broader ODF? Since we choose oblique orientation as a general approach of fitting, this point can be easily tested by fixing β_0 = 0 and let lateral size and orientation degree be the only two effective fitting parameters. It turned out that the nonlinear fitting will not converge if β_0 is fixed at zero. It has been discussed that in the stretching process, equatorial tilted streaks are related to the superposition of meridian bars. In that case, the tilting angle is only about 5 ^{o}; with or without fixing β_0 does not affect the result. However, for this large oblique angle of about 20 ^{o} due to the relaxation during melting, simple parallel orientation approximation does not work.

A follow-up question which is more critical is as follows. Why parallel orientation fails in SAXS pattern fitting but still works for WAXS pattern? An easy way of thinking is that $I(\phi) \sim \phi$ profile obtained from WAXS pattern is more sharp (the $\langle P_2 \rangle$ exceeds 0.9 for one peak fitting), which makes it not too different if using a superposition of two distributions. In fact, splitting an equatorial peak is a more complicated operation, as the fiber average will further smear the tilting.[73] The deeper origin of this phenomenon is rooted in the fact that mosaic crystal blocks in a lamella are not rigidly connected, even though a lamella is tilted, crystal blocks are possible to be more aligned due to the strong tensile force. Since 122 ^{o}C is not high enough to erase preexisting textures (tilted microfibrils, tilted lamellae), this effect can still be observed. In contrast, after melting at temperatures that are close to the melting temperature where most of preexisting structures are ironed out, and only sporadic oriented nuclei survive, the oblique angle disappear.

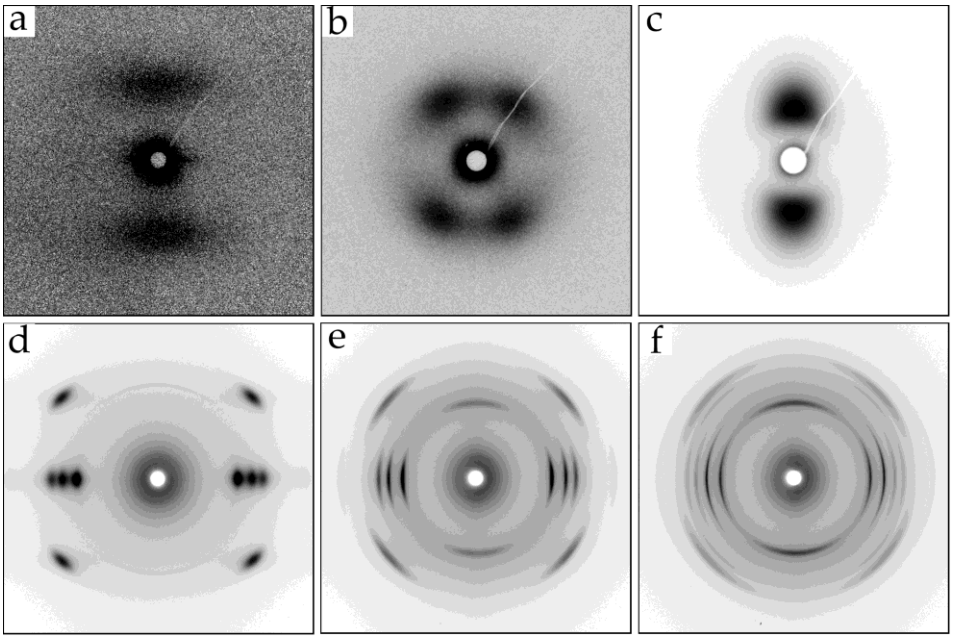

Figure 6-14. Final scattering patterns of P-B copolymer stretched at 60 ^{o}C with strain =3.71 **(a)** and **(d)**; Scattering patterns of the pre-oriented sample (after being stretched to strain =3.71 at 60 ^{o}C) after melted at 122 ^{o}C and then crystallized at 100 ^{o}C for 20 min **(b)** and **(e)**; and the patterns of the same sample after melted at 130 ^{o}C **(c)** and **(f)**.

To further verify this idea, the same experiment was performed for sample pre-oriented at 60 ^{o}C. As will be shown in chapter 7, the stress during stretching is much higher at 60 ^{o}C. When drawing to the same strain, the oriented structure is less stable. **Figure 6-14** shows SAXS (the first row) and WAXS (the second row) patterns for these experiments. **Figure 6-14a** and **6-14c** are SAXS and WAXS patterns when P-B copolymer was stretched at 60 ^{o}C, with strain =3.71. The crystal orientation is almost perfect as can be seen from the WAXS pattern (quantitative analysis will be given in chapter 7, at this moment qualitative discussion is good enough to demonstrate the idea of relaxation). After melting at 122 ^{o}C and then cooled down to 100 ^{o}C, namely, crystallizing from partially melted sample, SAXS pattern splits into four-point (**Figure 6-14b**). In this case, the oblique angle is obvious. In the same time WAXS pattern shows continuous diffraction arcs (**Figure 6-14e**). Melting at 128 ^{o}C erase most of preexisting structures; and the two-point pattern is formed (**Figure 6-14c**).

6.4 Summary

Relaxation behavior of pre-oriented P-B random copolymer was tested by melting and recrystallization experiments. The main conclusions in this chapter are as follows.

1. There is a time lag in SAXS pattern development as compared with WAXS patterns during continuous heating. SAXS patterns can survive at higher temperature where no diffraction peaks are noticeable in WAXS patterns, which suggests a two-step melting behavior, namely, a disappearance of lattice coherence of crystal (as revealed by WAXS), followed by diffusion of polymer chains into amorphous surroundings. The latter takes place in a large scale as revealed by SAXS.

2. During melting, the change of WAXS pattern is continuous. While the scattering invariant as derived from SAXS method shows a nonmonotonic behavior due to the change of relative ratio of concentration in two-phase model.

3. The tilted streaks near the equator are correlated to the meridian bars. Streaks are contributed by shish-like structure which is consisted of polymer chain bundles (not crystalline). Meridian bars are originated from lamellar crystals (kebab) epitaxially grown on the surface of microfibrils/shishes. Streaks first become stronger during heating because of melting away of kebab surroundings, followed by a decrease due to the fusion of the bundles.

4. The strengthening of equatorial streaks during heating provides a chance to quantitatively analyze the dimensions of the microfibrils. By using 2D hard-disk model, the diameter of the microfibril was calculated as about 8 *nm*.

5. Crystals can preserve, to some extent, the orientation during recrystallization after melting the pre-oriented sample at higher temperatures, if the temperature for melting is not too high. Newly grown crystals are dominated by the γ-phase with the diagonal orientation mode. When melting at high temperature (132 ^{o}C) where most preexisting structures are erased, newly grown crystals are nearly isotropic, and the content of the γ-phase is close to that in the native crystalline state of P-B copolymer (crystallized in quiescent condition).

6. For sample melted at a lower temperature (122 ^{o}C), preexisting crystalline structure can be largely preserved, but relaxed. SAXS pattern in this case is essentially four-point,

with an oblique angle of about 20 ^{o}. This confirms the model proposed in chapter 5 where shishes are tilted and lamellar crystals are epitaxially grown upon them (and hence are also tilted). Higher temperature destroys these structures; and the survived crystals, although oriented, are sporadically dispersed. In this case, the oblique angle in SAXS pattern vanishes.

7 Stretching-Induced Crystallization: Influence of Temperature

So far the crystallization of P-B copolymer induced by uniaxial stretching has been mainly examined at the high temperature (100 ^{o}C). The influence of temperature on the crystallization behavior of P-B copolymer with low content of butene comonomer will be discussed in this chapter. The sample is the same as that has been used in previous three chapters. Experimental procedure has been described in chapter 5. Two more temperatures, namely, 60 ^{o}C as the mid-temperature and 25 ^{o}C as the room temperature will be selected to perform stretching experiment. Data will be compared with that obtained at the high temperature, 100 ^{o}C, which is reported in chapter 5.

7.1 Stretching at the mid-temperature (60 ^{o}C)

All possible orientation modes for α and γ-phase have been introduced before. The simulated pattern can be found in **Figure 4-5** and **Figure 5-5**, in chapter 4 and 5, respectively. A comparison of fiber diffraction patterns of P-B copolymer stretched at 60 ^{o}C and at 100 ^{o}C with different strains (0.5 for low strain, and 2.5 for high strain) is shown in **Figure 7-1**. Both experimental and simulated patterns are shown in the same style that has been used in previous chapters. The general features of diffraction patterns obtained at 100 ^{o}C are the same as those obtained in 60 ^{o}C. There are two main differences. First, two split arcs near the meridian, in the same ring of $(110)_{\alpha}$ is found throughout the stretching. This arcs may have two origins: (110) plane of daughter lamellae of the α-phase or (111) plane of the parallel oriented γ-phase (see **Figure 4-5** and **Figure 5-5** for detail). After a comprehensive examination of the entire stretching process, we intend to assign these arcs to daughter lamellae of the α-phase, since we observed that the content of the γ-phase keeps decreasing during stretching , while the intensity of these arcs even increases slightly in the process. Therefore, it must be due to the recrystallization of the α-phase crystals. This fact also explains why these arcs are not found in diffraction patterns at 60 ^{o}C, as the temperature is low and strong tensile force tends to destroy the branches. Second, in the late stage (high strain), widths of diffraction arcs in diffraction

patterns obtained at 60 °C is larger than those in the patterns obtained at 100 °C. At lower temperature, chain mobility is low and the system is more viscous. Consequently, the stress borne by the network is higher, and hence lamellae are ready to be destructed into smaller pieces, corresponding to a larger width of diffraction line profile.

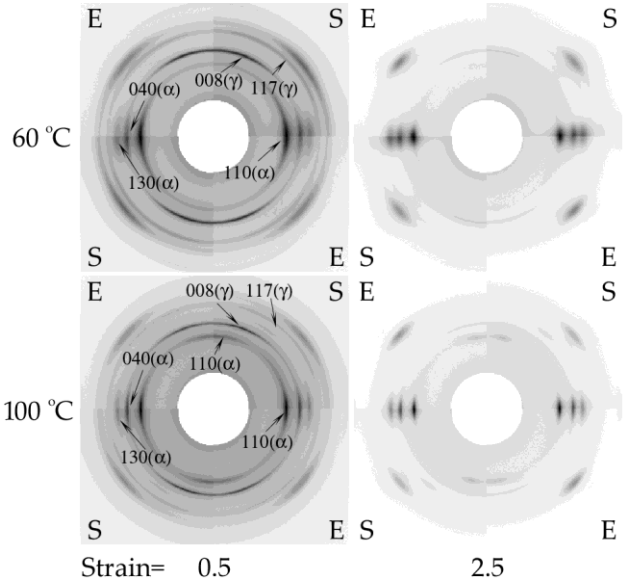

Figure 7-1. Simulated and experimental diffraction patterns at low and high strains (strain=0.5 and 2.5, respectively), at 60 °C and 100 °C. In each image, upper left and lower right quarters are experimental results, denoted as **E**; upper right and lower left quarters are simulated patterns, denoted as S. Main Miller indices are annotated.

In the following context in this section, various parameters showing the structure development of P-B copolymer will be discussed for samples stretched at both 60 °C and at 100 °C. Data obtained at 100 °C has been shown before, but will be plotted for comparison purpose. **Figure 7-2** shows the change of crystallinity as a function of strain when being stretched at 60 °C and at 100 °C, respectively. The initial crystallinity of sample at 100 °C is lower. This is because that the sample was naturally cooled down from molten state (150 °C) to room temperature, and the system contains lamellar crystals with a spectrum of thickness. At high temperature, small crystals are melted first. The significant difference of crystallization curves at high- and mid-temperature appears in the early stage, i.e., during the period of yielding (peak position of yielding is around strain = 0.2, as shown in the dashed line in **Figure 7-2**). Two opposite effects of stretching has been discussed in chapter 5. At 100 °C, the stretching-induced destruction of crystals and the recrystallization almost cancel each other, as chains are more mobile and are easy to form new crystals. Apparently, the first effect dominates the yielding process at 60 °C—

the crystallinity continues to decrease by about 5% during this period. After yielding, both curves exhibit a same trend of increase, and crystallinities are close to each other. From the simple crystallinity point of view, there is no difference between samples stretched at high- and mid-temperature after yielding. However, as will be shown later, they produce completely different morphologies.

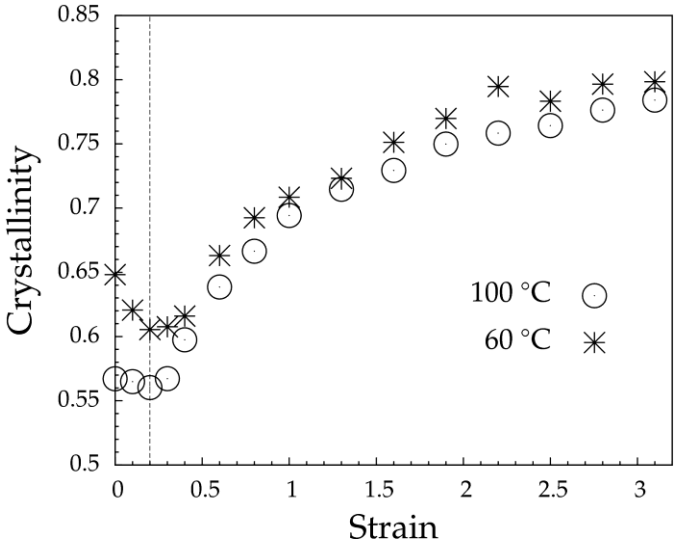

Figure 7-2. Change of crystallinity during stretching at 60 ^{o}C and 100 ^{o}C.

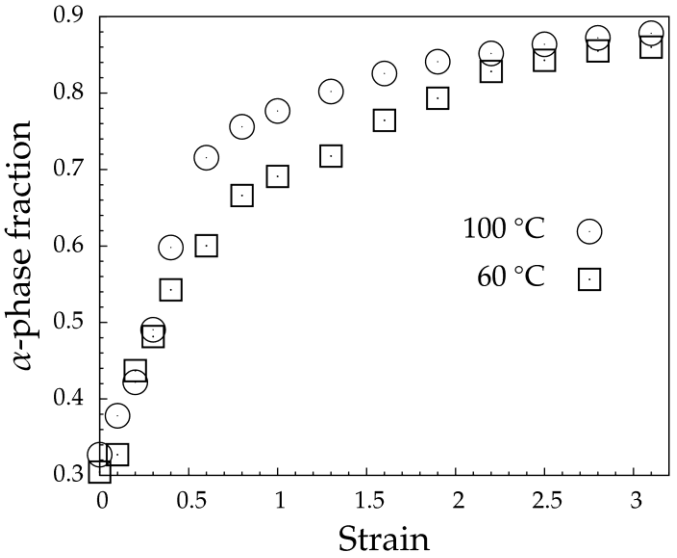

Figure 7-3. Change of α-phase content as a function of strain during stretching at 60 ^{o}C and 100 ^{o}C.

As seen from **Figure 7-1**, diffraction patterns in the late stage are mainly contributed by the α-phase, at both temperatures. 2D analysis conveys the possibility of separating different modifications via polar angle dependence. **Figure 7-3** shows the process of γ-to-α transition. The general trend of the increase of the α-phase at two temperatures are similar, but the α-phase content is higher at 100 ^{o}C. This is due to the nature of α- and γ phase: α-phase is thermodynamically more stable, and hence can survive at higher temperatures.

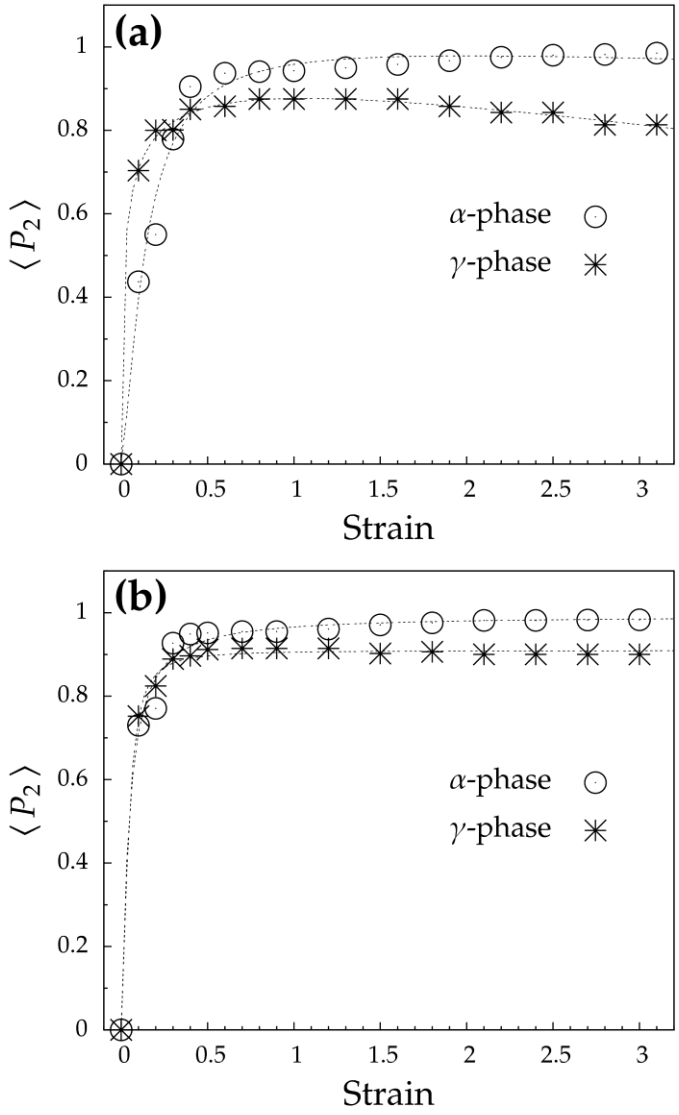

Figure 7-4. Change of Hermans' orientation function during stretching at 60 ^{o}C and 100 ^{o}C.

The change of $\langle P_2 \rangle$ as a function of strain at 60 ^{o}C and 100 ^{o}C is shown in **Figure 7-4a** and 7-**4b**. Again, dramatic change takes place during yielding. After strain = 0.4, the $\langle P_2 \rangle$ values

become stabilized. At both temperatures, the change of $\langle P_2 \rangle$ of the γ-phase is faster than that of the α-phase in the early stage. After that, α-phase has larger degree of orientation. This inversion behavior has been explained in chapter 5, owing to the change of the network dominated by the γ-phase to that dominated the by the α-phase. At 60 ^{o}C, $\langle P_2 \rangle$ of γ-phase even decreases slightly in the late stage, as the force transmitted to the polymer network at lower temperature is significantly higher than that at higher temperature (see the stress-strain curves that will be discussed later). Therefore, compared to the situation of 100 ^{o}C, tensile force destructs the preexisting texture dominated by the γ-phase more severely, making the γ-phase crystals less entangled with their environment network, and hence losing their orientation to some extent.

To investigate the morphology difference, selected SAXS patterns during the stretching process at 60 ^{o}C and 100 ^{o}C are shown in **Figure 7-5** in which the change of the SAXS patterns from four-point patterns to two-point patterns can be clearly seen (isotropic rings as the initial scattering patterns are not shown). We attributed the four-point pattern to the γ-phase lamellae in chapter 5. After yielding, four lobes gradually disappear, as most γ-phase has been transformed to α-phase, and we observe an increase of intensity in the meridian direction in the same time, corresponding to the α-phase lamellae.

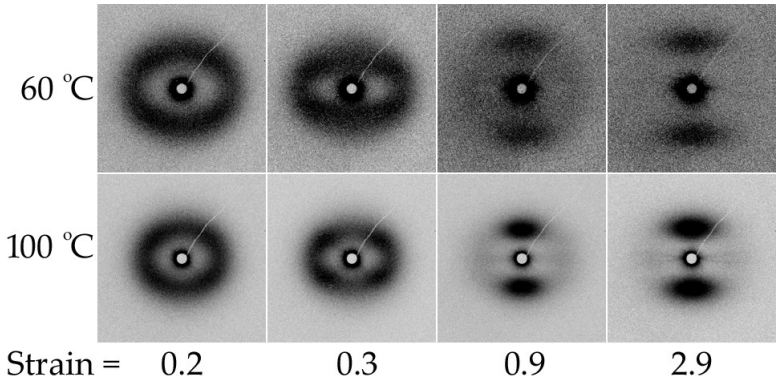

Figure 7-5. Selected SAXS patterns in the stretching process at 60 ^{o}C and 100 ^{o}C.

A change of long period as a function of strain is shown in **Figure 7-6**. Long periods are obtained from 1D curves integrated from the meridian region of the SAXS patterns. A general trend is that long period first increase in the early stage and then drop back to the original level. The increase of long period can be interpreted as falling apart of lamellae due to tensile force, or

equivalently, due to the inter-lamellar slip. The new crystals are grown in the same time during the exfoliation process of preexisting lamellae, and the inter-lamellar distance of newly grown lamellae is about the same as that in the static state. Also, it is found that on a whole, long period at 60 ^{o}C is shorter than that at 100 ^{o}C. Since the crystallinity at 60 ^{o}C is lower, the shorter long period must be due to thinner lamellar thickness. This is reasonable, since thicker lamellae grow at higher temperatures.

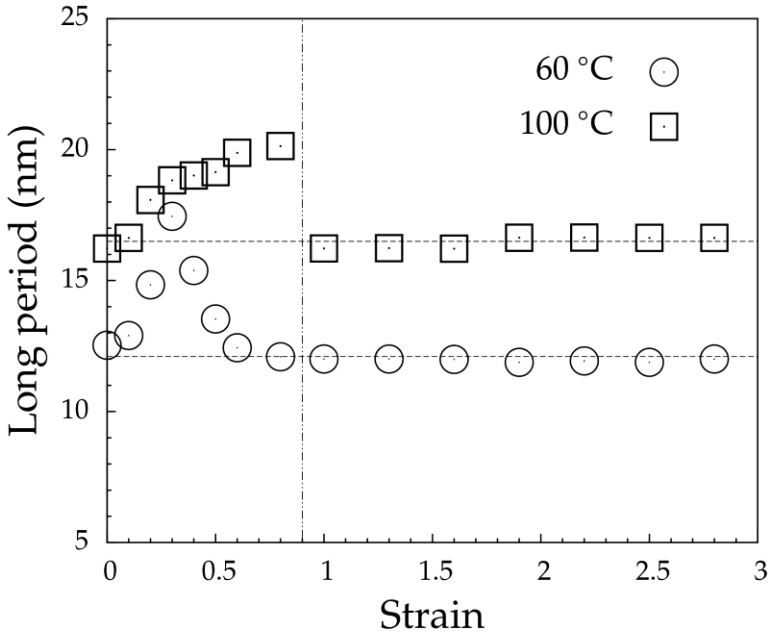

Figure 7-6. Change of long period as obtained from 1D SAXS curve as a function of strain at 60 ^{o}C and 100 ^{o}C.

The intensity distribution in the meridian is influenced by two factors: lateral size and orientation degree of lamellar crystals[79]. These two effects are illustrated in **Figure 7-7a**. For perfectly oriented lamellae, intensity only spreads along s_{12} direction; while orientation generates polar angle dependence of intensity, as shown in the dashed line in **Figure 7-7a**. As discussed in chapter 2, Legendre expansion approach can be used to decouple these two effects, and it has been applied to analysis of SAXS patterns at 100 ^{o}C, since lamellae are neither perfectly oriented nor infinitely large at that temperature. Two-point patterns at 60 ^{o}C are different, as can be seen from **Figure 7-7b**. The meridian intensity is restricted between two horizontal dashed lines. Therefore it can be approximated that lamellae are perfectly oriented. In this case, intensity distribution along s_{12} direction determines the lateral size of a lamella. In **Figure 7-7c**, the s_{12}–

dependent intensity is fitted with a Lorentzian function; and the reciprocal integral width gives an estimate of lateral size.[79]

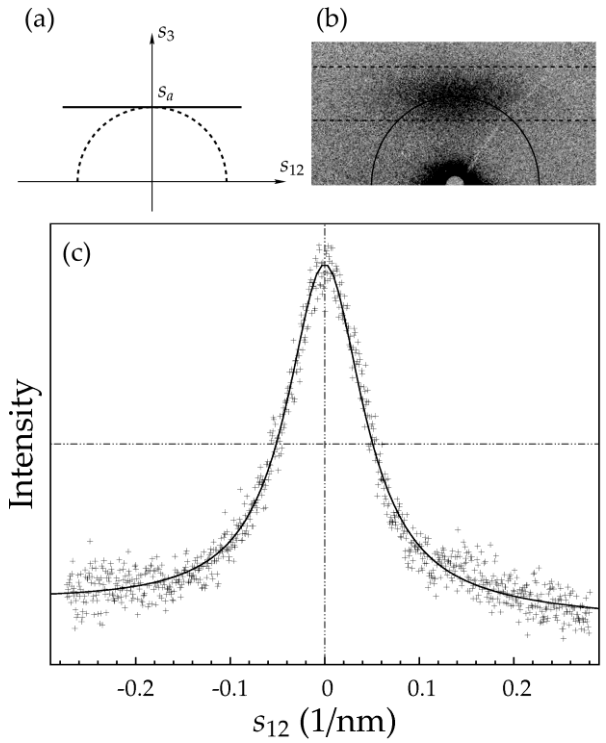

Figure 7-7. Illustration of size and orientation effects on the intensity distribution in SAXS pattern **(a)**, half of SAXS pattern at 60 ^{o}C (strain = 2.2) showing meridian intensity is restricted between two horizontal dashed lines **(b)**, and a fitting of s_{12}-dependence of intensity (dots) with Lorentzian function (solid line) **(c)**.

The result is shown in **Figure 7-8a**. In **Figure 7-8a**, lateral size obtained from the method discussed above is compared with that obtained from WAXS data (by analyzing line profile of diffraction peaks). We have discussed before that during the stretching process, a lamella is not a bulky piece but consists of smaller mosaic blocks. The argument is made based on the fact that lateral width obtained from SAXS method is larger than that obtained from WAXS method, as WAXS only 'sees' the boundaries of given crystallographic planes, while SAXS detects the dimensions of lamellae, in the nanometer length scale. Lateral sizes at both temperatures show this phenomenon, as can be seen from **Figure 7-8a** and **7-8b**. The difference is that at 60 ^{o}C lateral size obtained from SAXS method is only slightly larger than that obtained from WAXS method (about 5 *nm*). In contrast, at 100 ^{o}C, one piece of lamella contains more than three mosaic blocks with a size of about 9 *nm*. This is again due to the fact that high temperature

makes polymer chains more mobile, and the stress carried by the network is smaller. Consequently, lamellae can grow larger and are less likely to be stretched into small pieces.

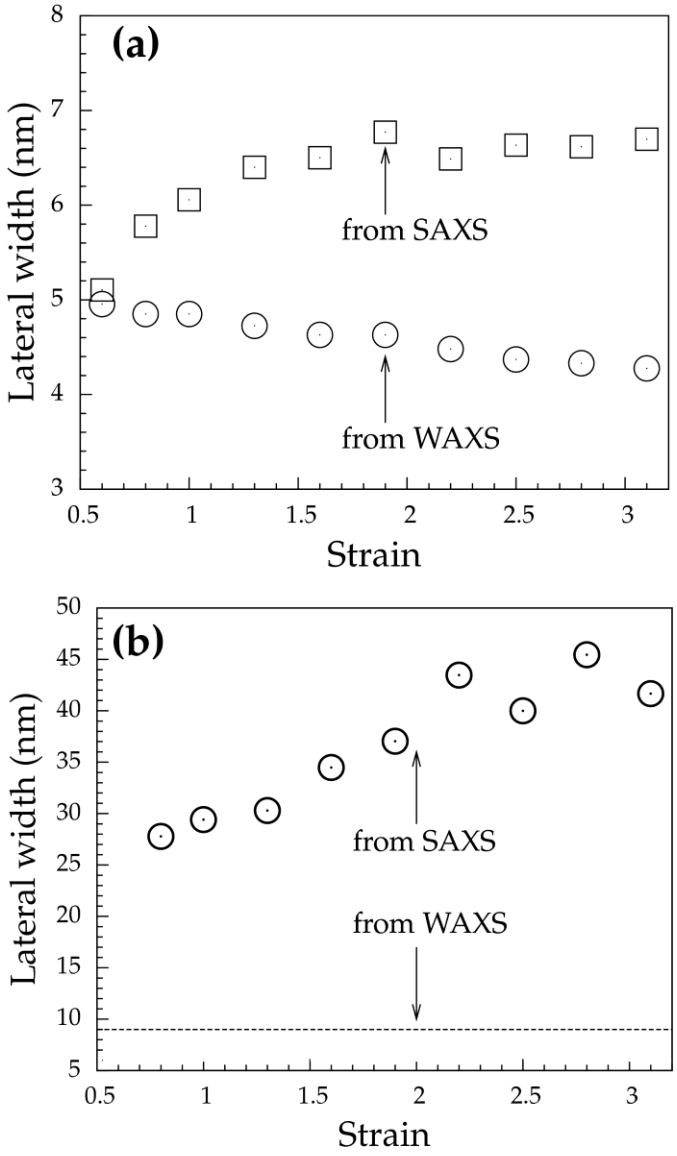

Figure 7-8. Change of lateral size of lamellae as obtained from WAXS and SAXS data as a function of strain at 60 ^{o}C **(a)** and 100 ^{o}C **(b)**.

The increase of lateral size obtained from SAXS data at both temperatures can be attributed to the recrystallization process induced by the tensile force. As for the size obtained from WAXS data, we did not observe noticeable change at 100 ^{o}C. However, a slight decrease of size at 60 ^{o}C was observed (the decrease is obvious since one can judge directly from WAXS pattern that diffraction arcs get broadened as stretching proceeds). The decrease of crystal size at lower temperatures indicates that intra-lamellar slip is severe. This is reasonable as the network

is borne stronger force at this condition. We will see in the following context that the situation becomes even more severe at room temperature.

7.2 Stretching at room temperature

Stretching process of iPP at low temperature is closely connected to the formation of the so-called mesomorphic phase, featured with broad and diffuse scattering in the equator. The diffuse diffraction spots in WAXS patterns were also observed in our P-B copolymer stretched at the room temperature, especially in the late stage. There are still controversies about the origin of the mesomorphic phase, mainly represented by three interpretations[148, 149]. Natta et. al[88]. used 'smectic' phase to describe because that in addition to chain parallelism, there exists certain degree of correlation in the direction of chain alignment. Gailey et. al.[150] proposed that it is composed of small hexagonal crystals. Their argument is based on the fact that two main diffraction peaks of the β-form crystal are close to that shown in the mesomorphic phase diffraction pattern. On the other hand, the diffraction curve of the mesomorphic phase was interpreted based on the α-form crystals, by considering line-broadening and intensity suppression due to disorder effect[148].

We first exclude the 'smectic' phase model. Cohen and Saraf modeled the smectic phase of iPP using direct correlation function approach.[151] Assume the building block is still 3_1 helix which is the same as that of iPP crystals; polymer chains are parallel packed, but are free to rotate; and the inter-chain interaction is described by hard-disk potential. The above model successfully predicts two diffraction peaks at around s= 0.17 $Å^{-1}$ and 0.23$Å^{-1}$, but is unable to explain four off-axis diffraction spots in fiber diffraction pattern. Line-broadening and lattice disorder of the α-phase need careful examination. If this is the case, it is expected that during the stretching process, diffraction arcs of the α-phase gradually get broadened, and will be merged together to form a diffuse scattering spot. However, this is not true as can be seen from **Figure 7-9** in which selected diffraction patterns at early stage are shown. We did not observe an increase of line width of the α-phase diffraction arcs. Instead, intensity between (110) and (040) arcs (as indicated by the arrows in **Figure 7-9**) keeps increasing independently during stretching. This observation strongly suggests that a new phase is forming, which is not due to the destruction of preexisting α-phase.

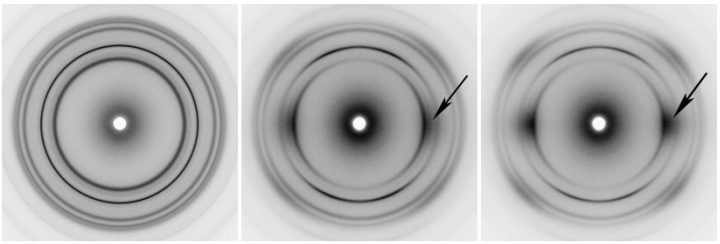

Figure 7-9. Selected WAXS patterns in the early stage of stretching at room temperature. The arrows are pointed to the position where s = 0.167 Å^{-1}.

β-form is the most disordered modification in iPP. Its crystallographic characteristics has been introduced in chapter 3. In the practice of 2D whole-pattern simulation, we first adopt coordinates of asymmetric unit reported by Ferro et. al.[87], and then generate the full set atomic coordinates in a β-form unit cell by performing $P3_121$ symmetry operation. To fit our data, the dimensions of the unit cell has to be modified to a=b=11.96 Å and c=6.49 Å. The calculated powder diffraction profiles of α- and β-phase is shown in **Figure 7-10**. Two strongest peaks of β-phase appear at s =0.167 Å^{-1} and 0.227Å^{-1}, corresponding to diffuse scattering spots at equatorial and off-axis positions in the 2D patterns, respectively. Miller indices are also annotated in **Figure 7-10**. For hexagonal unit cell, the multiplicity is not intuitive.

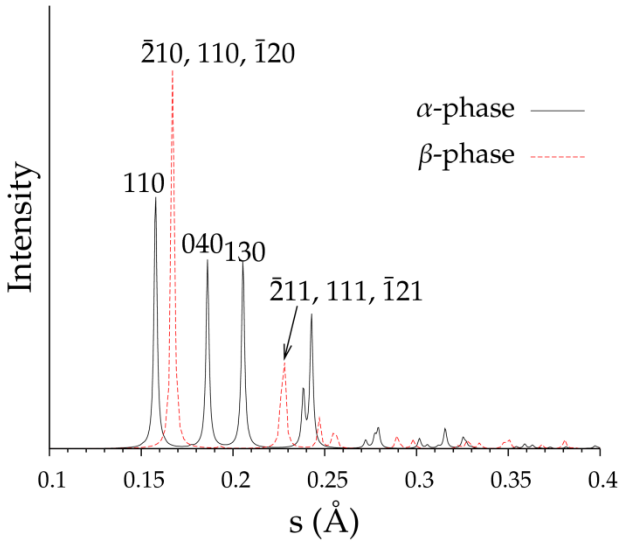

Figure 7-10. Calculated powder diffraction profiles of α- and β-phases.

Our diffraction patterns of P-B copolymer stretched at room temperature can be simulated mainly based on tiny β-phase crystals. The crystal size as approximated from line

profile of is about 16 Å which can only hold one unit cell. Moreover, we found that the β-phase alone cannot generate such strong intensity in the equator as observed in our experiment. A considerable amount (about 50%) of oriented amorphous phase must be added to compensate for it. That is to say, the final 'apparent crystallinity' which is about 70%, is composed of 20% of β-phase and about 50% of oriented amorphous phase. Selected simulated and experimental patterns at low- and high- strain are shown in **Figure 7-11**. Simulated patterns are combined with experimental counterparts in the same way as has been shown in **Figure 7-1**, and in previous chapters. In this case, preexisting α- and γ-phase are transformed to the mesomorphic phase consisting of oriented amorphous bundles mixed with tiny β-phase crystals. Polymer chains in both amorphous bundles and tiny β-phase crystals are aligned along the fiber axis direction.

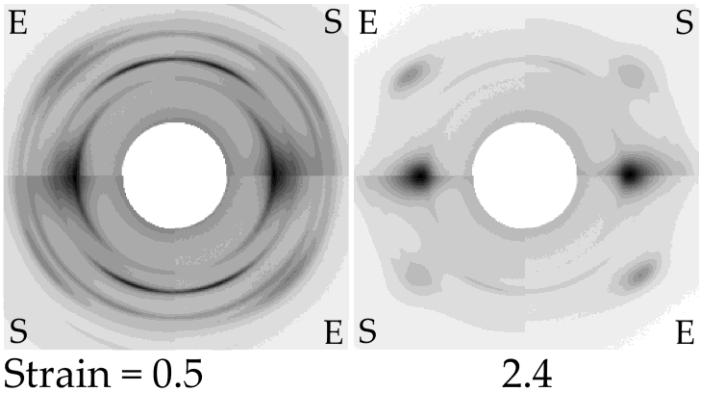

Figure 7-11. Simulated and experimental diffraction pattern of P-B copolymer stretched room temperature, at strain=0.5 and 2.4. In each image, upper left and lower right quarters represent experimental results; upper right and lower left quarters are from simulation result.

The β-phase crystals are so tiny that each of them is composed of only one or two hexagonal unit cells; hence they cannot form lamellae, let alone generating periodicity at nanometer length scale. This argument is supported by SAXS patterns/profiles, as shown in **Figure 7-12**. In the very early stage, γ-phase still dominates, an interference maximum can be found in the 1D profile, similar to the situations of being stretched at mid- and high-temperature. The hump completely disappeared in the late stage where one can only observe a strong equatorial streak. The intensity of the streak is so strong that it must not be contributed entirely by oriented fibril bundles. It has been discussed that fibril bundles is possible to cause streak, as is the case of high temperature stretching. But that streak is weak, as it is not expected that the density contrast between a bundle and its surrounding to be high.[152] In fact, in the room

temperature stretching experiment, we observed significant stress-whitening effect due to micro-voids. Voids' density can be neglected, they are able to generate strong streak, and the interface between voids and their surroundings will even magnify this effect. By combining the WAXS and SAXS data, an illustration of the structure of mesomorphic phase is shown in **Figure 7-13**.

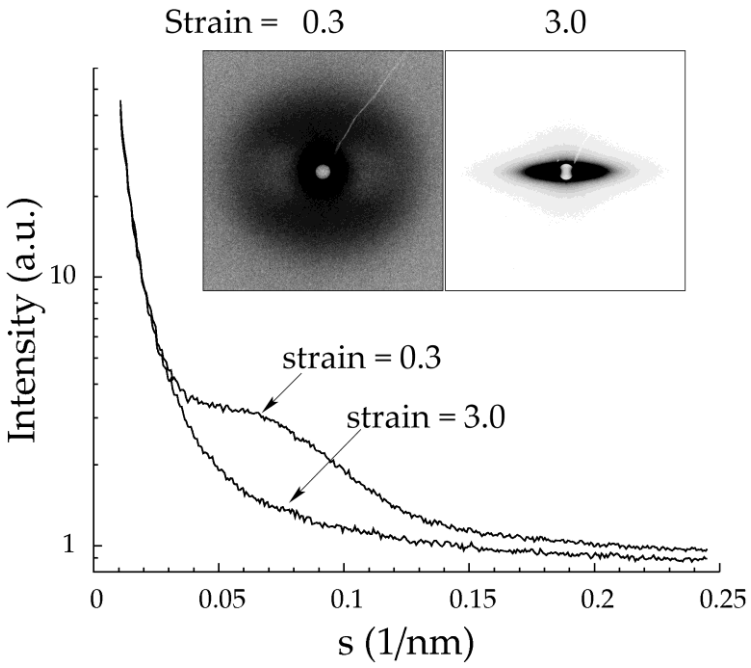

Figure 7-12. 1D SAXS profiles of P-B copolymer stretched at room temperature, at low (strain=0.3) and high (strain=3.0) strains. The curves are integrated from meridian region, corresponding 2D SAXS patterns are shown in the in-set.

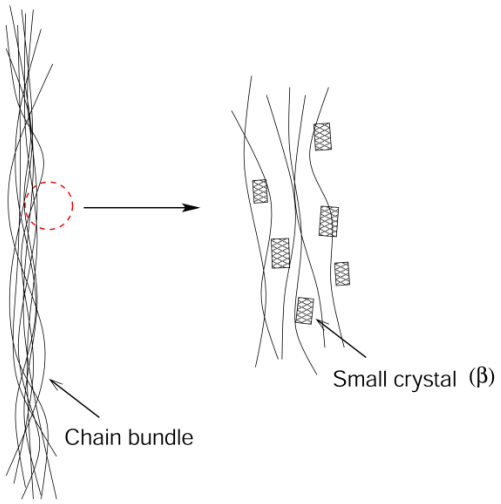

Figure 7-13. A carton illustration of mesomorphic phase which is composed of oriented amorphous phase and small β-phase crystal blocks.

7.3 The structure-property relationship

It has been shown that temperature greatly influences the polymorphism, preferred orientation and morphology of P-B copolymer during stretching. Those observations should be able to be correlated with mechanic properties of the material. A direct measure is to use the plot of tensile stress as a function of strain during stretching. **Figure 7-14** shows the engineering stress-strain curves of P-B copolymer at three temperatures: 25 ^{o}C, 60 ^{o}C and 100 ^{o}C. Regardless of the temperature, all other experimental conditions are the same. The curves possess some general features of deformation of semi-crystalline polymer. It starts with a linear increase of stress at small strain and then shows a yielding behavior, followed by a plateau region. A strain-hardening is observed in the late stage of stretching.

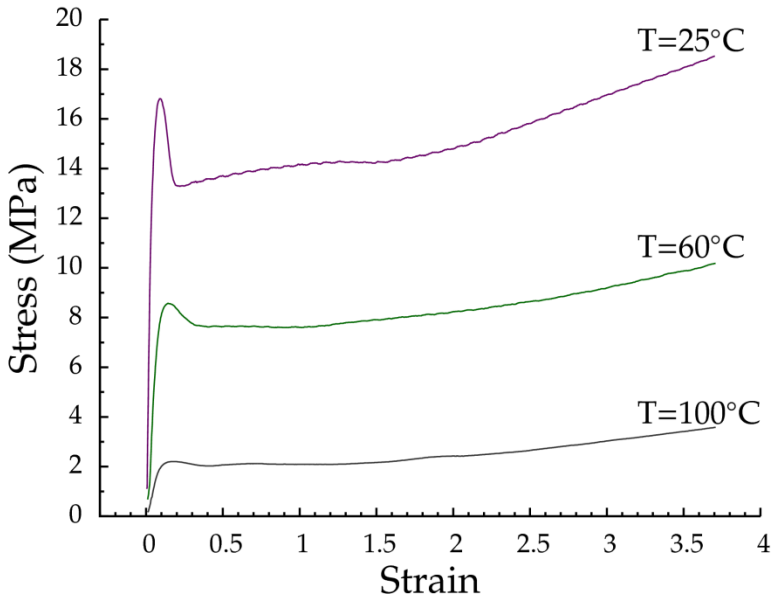

Figure 7-14. Engineering stress-strain curves of P-B copolymer stretched at three temperatures: 25 ^{o}C, 60 ^{o}C and 100 ^{o}C.

The influence of temperature is two-fold. First, initial crystallinity varies with temperature. The initial crystallinity is formed during a non-isothermal crystallization process: the sample was naturally cooled down from 150 ^{o}C to 25 ^{o}C. Before each stretching measurement, the sample was equilibrated at the experimental temperature for 2 *min*, which means that small crystals will be melted at higher temperatures. The initial crystallinities are 76.2%, 64.8% and 56.7%, respectively, as determined from WAXS data. Second, chain mobility increases with temperature. Consequently, at high temperature, chains in amorphous region are

more easily to disentangle with the presence of stretching, or, to change a word, tie-chain is less likely to be formed at high temperatures.[153] As a result, stress cannot be easily accumulated in the network and hence transmitted to crystals at high temperatures. This can be seen clearly from the stress-strain curves that, in general, stress becomes higher as temperature decreases.

From a microscopic point of view, the origin of yielding of semi-crystalline polymer is interpreted as screw dislocation of lamellae and melting-recrystallization process.[6, 154] In either case, it means a transformation from a preexisting texture to another. Keeping in mind the two effects caused by temperature, it can be understood why yielding at lower temperature is sharper and the yield strength is higher: the higher crystallinity and lower chain mobility makes the barrier of changing from the preexisting texture to a new, stretching-induced structure higher. It is generally accepted that yielding involves a transformation from localized disassociation of micro-domains (or more specifically, lamellae for semi-crystalline polymer) to a collective flow behavior in which chain-slip takes place in a break-through manner.[129] High temperature moderates this process of stress accumulation and release.

Inter- and intra-lamellar slips are two fundamental processes during the stretching process. Inter-lamellar slip is about the dissociation of lamellar aggregates within which lamellae are connected by chains lay between two adjacent lamellae. Inter-lamellar slip is related to the dislocation within a crystal lamella. Obviously, the latter is more difficult to occur, since intermolecular force within a crystal lattice is much stronger. The lower the temperature is, the more severe the crystals are destructed in an intra-lamellar level. At 100 ^{o}C, although we did not observe line-broadening in WAXS measurement, lamellar orientation derived from 2D SAXS data decreases after yielding. We have explained that this is due to the intra-lamellar dislocation. A mosaic crystal block has an average size about 9 *nm* as shown in **Figure 7-8b**. As the temperature lowers down to 60 ^{o}C, this size decreases to about 5 *nm*, and it keeps increasing during stretching (**Figure 7-8b**), indicating that more severe intra-lamellar slip takes place. At 25 ^{o}C the force applied to the network and hence transmitted to crystals is so large that lamellae are fragmented into tiny pieces, with each of them only contains less than 2 unit cells of β-phase.

Figure 7-14 also shows that as temperature decreases, the strain-hardening effect becomes more significant. Tensile force tends to destruct the original isotropic texture; network

consisting of microfibrils are generated after yielding.[155-157] Strain-hardening is originated from the deformation of this network. Since these fibrils are well oriented along the stretching direction, further deformation leads to edge dislocation with Burger's vector in parallel to the stretching direction, and the energetic cost is much higher, especially at lower temperature where system is more viscos and chains are less mobile. Microfibrils are formed at all temperatures, but the morphologies are different. At 100 ^{o}C, the oriented fibrils are able induce lamellar growth in perpendicular to its long axis (in accordance with the fiber axis),[152] and the lateral width of the lamellae ranges from 25 *nm* to 45 *nm*, as shown in **Figure 7-8a**. At 60 ^{o}C the morphology is similar, but the width of lamellae is smaller: ranges from 5 *nm* to 7 *nm*. At room temperature, the fibril is consisted with about 50% of oriented amorphous phase and tiny β-phase crystals, as can be seen from the diffuse scattering spots in the equator of the WAXS patterns.

7.4 Summary

We used combined *in-situ* 2D WAXS/SAXS techniques to study the structure development of P-B random copolymer under uniaxial tensile force field. The temperature dependence of structure change is the main focus of this chapter. The main conclusions are summarized as follows.

1. Engineering stress-strain curves show different behavior at different temperatures. As temperature decreases, yielding becomes sharper and the stress becomes higher. Strain-hardening is more significant at low temperature as compared with that at high temperature.

2. P-B random copolymer prefers to form γ-phase in quiescent condition. γ-phase is unstable when tensile force is applied. At mid- and high-temperature (60 ^{o}C and 100 ^{o}C), it was gradually transformed to α-phase as stretching proceeds. At low temperature (25 ^{o}C), mesomorphic phase consisting of tiny β-phase crystals and about 50% of oriented amorphous phase was observed.

3. Under stretching, γ-phase adopted a tilted cross-β configuration at all temperatures. At 100 ^{o}C, two populations of α-phase crystals were observed: main (mother) lamellae with the *c*-axis in parallel to the fiber axis and daughter lamellae with the *c*-axis having

an 80 ^{o} angle with respect to it. At 60 ^{o}C, daughter lamellae disappeared. β-phase was generated at 25 ^{o}C with the *c*-axis in parallel to the fiber axis.

4. Intra-lamellar slip becomes important as temperature decrease. At 100 ^{o}C, lateral width measured by WAXS line profile analysis is about 9 *nm* and it keeps unchanged during stretching. While the width decreases to about 5 *nm* at 60 ^{o}C; and it decreases slightly during stretching. At 25 ^{o}C, preexisting lamellar crystals were fragmented into small pieces due to strong tensile force, with each small crystal containing less than 2 unit cells. Further, considerable amount of oriented amorphous phase was formed at this temperature.

8 Final Remarks

Main conclusions are summarized in the end of each chapter. In this final chapter, a consistent interpretation of major observations regarding to random copolymer crystallization, especially with the presence of external fields, will be given. The purpose of this chapter is to provide a coherent view of preferred orientation, polymorphism and morphology in propylene-based random copolymer under external force fields.

8.1 Polymorphism and preferred orientation

Major experimental observations of polymorphism and preferred orientation during crystallization under static condition and with the presence of shear flow and uniaxial stretching are tabulated as follows.

Table 8-1. A summary of polymorphism and preferred orientation of samples tested in this thesis.

Samples & Experimental conditions		Crystal modifications	Preferred orientation	Interchange between phases
P-H, static		α	--	--
P-B, step-shear (100 °C)		γ	cross-β	constant ratio
		α	*c*-axis orientation	
P-B, stretching	100 °C	γ	tilted cross-β	$\gamma \rightarrow \alpha$
		α	*c*-axis orientation *a*-axis orientation	
	60 °C	γ	tilted cross-β	$\gamma \rightarrow \alpha$
		α	*c*-axis orientation	
	25 °C	γ	tilted cross-β	$\gamma \rightarrow \beta$
		β	*c*-axis orientation	
P-B, Melting-recrystallization		α	*c*-axis orientation	$\alpha \rightarrow \gamma$
		γ	diagonal	

The propylene-based random copolymer exhibits interesting polymorphism during crystallization. It is clear that the factors responsible for this behavior are quite complex, where the contour length of the comonomer, its content and distribution all play a role in an interrelated manner.

Under static conditions, the low content of 1-hexene does not change the polymorphic behavior of iPP, as α-phase is the only modification observed. However, the low content of 1-butene tends to favor the formation of γ-phase.

When subjected to external forces, various orientation modes of orientation have been observed, which are stemmed from different origins. A step-shear can be considered as a weak flow, containing both extensional and rotational components. The former tends to extend polymer chains in the flow direction, which is responsible for the *c*-axis orientation of the α-phase, as chains are packed in parallel to the *c*-axis in the α-phase unit cell; while the rotational component tends to induce the cross-β configuration of the γ-phase. This is due to the nature that chains are packed in a cross-hatched style along the *c*-axis of the unit cell, and they cannot be aligned to one direction simultaneously. In this case, the *c*-axis of the unit cell is in perpendicular to the machine direction of the shear flow. In essence, the cross-β configuration requires that the *c*-axis of the γ-phase unit cell, the principal axis of rotation (PA) and the fiber axis (FA) are all in parallel to each other (**Figure 4-5c**).

The extensional flow also has a profound effect on the orientation of the γ-phase. In this case, the machine direction (vertical) must be the FA (so should be the PA); where one of the diagonals of the *ab*-plane is in parallel to the FA/PA (**Figure 4-5a**). This mode is termed diagonal orientation in this thesis, which is equivalent to the 'parallel orientation' in de Rosa's notation.[145] This configuration is formed due to the following possibility. Since cross-hatched chains cannot be aligned to one direction in the same time, a possible way out is to have half of the chains aligned and the other half with an 80 ^{o} angle against the FA/PA. This orientation mode has a distinctive feature that all $(11l)$ arcs are split into three, with one located on the equator (**Figure 4-5a**), which is not obvious in our step-shear experiment (see **Figure 4-6** for detail). The cross-β configuration illustrated in **Figure 4-5c** is very consistent with our experimental results.

In uniaxial stretching experiments, only extensional flow needs to be considered. At all experimental temperatures, a tilted cross-β configuration of the γ-phase was observed. In this case, the cross-β configuration is induced by the extensional flow, and hence the FA is aligned with the machine direction (i.e., the stretching or vertical direction). The tilt angle of the *c*-axis in

the γ-phase unit cell with respect to the FA changes continuously during stretching, especially in the early stage. In the late stage, this value fixates at about 20 ^{o}. This can be understood when one also considers the observation of the γ-to-α transition. The γ-phase is the dominant modification in the early stage; it forms the skeleton of the polymer network, and bears the main stress load during deformation. As a result, the orientation of the γ-phase changes rapidly in the early stage of deformation. As stretching proceeds, the γ-phase network is gradually changed to the α-phase network, where the γ-phase crystals are not easy to be further oriented.

In the stretching experiments at 60 ^{o}C and 100 ^{o}C, majority of the α-phase adopts the *c*-axis orientation, which means that the polymer chains are aligned along the stretching direction. However, there are some differences between the two temperatures. At 100 ^{o}C, lamellar branching, which yields the *a*-axis orientation of the α-phase, was also observed. In the *a*-axis orientation, the *c*-axis of the unit cell has an 80 ^{o} angle with respect to the FA. This lamellar branching was not observed at 60 ^{o}C, indicating that the daughter lamellae are easy to be destroyed by the tensile force (the tensile force is higher at lower temperatures, as can be seen from the stress-strain curves).

At room temperature, the polymer chains are less mobile, and the stress applied to the system is so high that destruction of preexisting crystals becomes the main feature of the stretching process at this temperature. Preexisting γ-phase (dominant) and α-phase (minor) are destroyed and the mesomorphic phase is generated in the stretching process. The mesomorphic phase can be modeled using tiny β-phase crystals plus a considerable amount of oriented amorphous chain bundles. At this temperature, crystal growth becomes difficult, where the mesomorphic phase presents the largest parallelism of chain packing with respect to the machine direction. The β-phase possesses a hexagonal unit cell, and is the most disordered and loosely packed crystal modification of iPP.

For P-B copolymer with low content of 1-butene content, the γ-phase is favorable in its native state. The α-phase is formed due to the presence of strong tensile force because the cross-hatched chains cannot survive under this environment. Once the stretching-induced α-phase is ironed out by melting, the newly grown crystals will again be dominated by the γ-phase if the

system is cooled down to an appropriate crystallization temperature. If the α-phase is partially melted, the remaining α-crystals can still preserve a certain degree of orientation that is the *c*-axis oriented. These oriented α-phase crystals can serve as seeds to induce growth of the γ-phase crystals with diagonal orientation (**Figure 4-5a**). The more the α-phase is melted away, the less the newly grown γ-crystals become oriented.

8.2 Transitions between different phases

There are several transitions between the different crystal phases induced by stretching, as shown in **Table 8-1**, due to different mechanism. The most important one is the γ-to-α transition, which occurs under the condition when P-B copolymer was stretched at mid- and high-temperatures (i.e., 60 and 100 ^{o}C). The mechanism of the transition has been discussed in **section 5-4**, in Chapter 5. The phenomenon itself, as a consequence of the strong tensile force applied to the polymer network during crystallization is easy to understand. This is because polymer chains in the α-phase are parallel packed, which makes them more stable if strong tensile force is applied. However, there are some fundamental questions not yet address, e.g. how does the transition process proceed. More specifically, is the α-phase directly transformed from the γ-phase by local chain motion within the unit cell, or, the destruction of the α-phase occurs as the first step, and the new γ-crystals are grown due to recrystallization?

The experimental results indicate that the latter mechanism, namely, the destruction and recrystallization is more likely to be true for the following reasons. The inversion of the content of the γ-phase and the α-phase takes place mainly in the early stage. During this period, the γ-phase tends to form the cross-β configuration with the *c*-axis parallel to the machine direction. This is evidenced from the fact that the $(008)_{\gamma}$ arc moves toward the meridian direction. This orientation mode makes the γ-phase unstable when the stress is applied because polymer chains in this case are perpendicular to the direction of the applied stress. From the purely geometric point of view, the local movement of polymer chains within the unit cell that leads to the formation of the α-phase is not possible, since the only degree of freedom comes from the rotation of chains in the *ab*-plane that is quite unlikely when the force is applied perpendicularly.

Furthermore, if the γ-phase can be directly transformed into the α-phase in a one-step manner, it is expected to observe a continuous increase of crystallinity during stretching, as the unit cells of the γ-phase need not to be destroyed in this case. However, this is not what has been observed in the experiments. As can be seen in **Figures 5-11** and **7-2**, a decrease of crystallinity was observed in the early stage, and the decrease was severe at lower temperatures since the stress applied to the system was higher. Therefore, the γ-to-α transition must be a two-step process, starting from the destruction of the γ-phase, followed by the recrystallization of the α-phase.

The reverse process, namely, the α-to-γ transition was observed in melting and recrystallization experiment. This process resembles the heterogeneous nucleation and growth in static state, as the uniaxial tensile force is absent and crystallization takes place quiescently. The preference of forming the γ-phase of P-B copolymer in its native state is determined by the defective nature of the polymer chain. The stability of the α-phase is due to the presence of the tensile force which destroyed the γ-phase. Hence, if the preexisting stretching-induced α-phase is melted, the P-B copolymer tends to recover its original crystallization behavior. In this case, the orientation mode of the newly grown γ-phase crystal is determined by the amount of survived α-phase seeds that would induce the epitaxially growth of the γ-phase with diagonal orientation. This memory effect will disappear if preexisting structures are completely removed.

The γ-to-mesophase transition occurs during stretching of the P-B copolymer at room temperature. From the results of stretching experiment at high temperatures (60 and 100 ^{o}C), it has already been observed that destruction of preexisting structure becomes more severe as the temperature decreases. Thus, at room temperature, the amorphous polymer chains freed from the destruction process are not possible to grow into large crystals (lamellae) due to limited overall mobility. However, room temperature is still well above the glass transition temperature of the P-B copolymer (glass transition temperature for polypropylene is usually a negative value, and it will be even more lower for random copolymer[158]), which means polymer chains can still preserve some degree of freedom to move, although in a much more localized manner. Consequently, the β-phase crystal, which is the most disordered modification of iPP can be formed. The observation of off-axis arcs in diffraction patterns, although broad, suggests the

existence of crystal structure, and these off-axis arcs together with equatorial diffuse scattering match the main diffraction peaks of the β-phase. The newly formed crystals are tiny, as seen from the broad scattering peaks. Considerable amount of oriented amorphous phase (about 50%) has to be added to fit the data. Therefore, the nature of the so-called mesomorphic phase is the combination of tiny β-crystals embedded in orientated amorphous chain bundles.

8.3 Morphology

The texture at nanometer scale can be revealed by the SAXS data. Combined with the WAXS data, hierarchical structures ranging from unit cells to lamellae can be depicted. Advanced data analysis relies highly on high-quality data, with the assumption of simple fiber symmetry, as discussed in chapter 2. In step-shear experiment, the shish-kebab morphology has been well established as discussed in chapters 1 and 4. In this case, the resulting crystal orientation is relatively low, especially in the SAXS data. Thus, the 2D whole pattern analysis was mainly performed for the WAXS data, focusing on polymorphism, preferred orientation and disorder effect. The building block of the stretching-induced texture is the same as that formed in step-shear experiment. The main features of the stretching-induced morphology in the chosen polymer system are the shish-like structure and lamellar crystals. In this case, the crystal orientation is much stronger, allowing us to comprehensively analyze both WAXS and SAXS data on the 2D whole-pattern base. Some fine details of the stretching induced hierarchical can thus be given, which are summarized as follows.

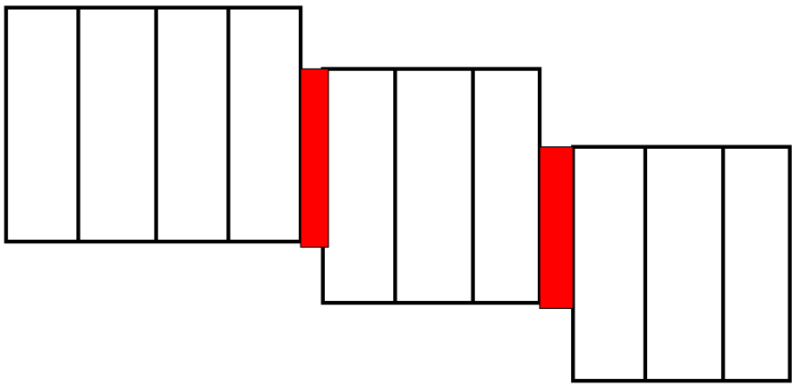

Figure 8-1. A carton illustration of a lamellar crystal.

One of the most interesting findings in the stretching-induced morphology is the fragmentation of lamellar crystals (at high temperatures). This conclusion is deduced from the

observation that the crystal size as derived from the WAXS data is substantially smaller than that derived from the SAXS data. Detailed descriptions of the data analysis are outlined in chapter 5. In WAXS measurement, X-ray 'sees' the objects in the atomic length scale, and the boundaries of crystal blocks determines the line-broadening of the scattering profile ($I(s) \sim s$ plot). Whereas SAXS probes the geometry in the nanometer scale, so that fine details within an object are absent to the X-ray. The fact that WAXS-derived size is smaller as compared to that derived from SAXS data suggests that a lamellar crystal is not a bulky piece, but is composed of smaller units: the crystal blocks.

A follow-up question is that what connects crystal blocks so that their integrity can be probed by SAXS? Although exact detail is unknown, those intermediate regions are possibly composed of chains pulled out from a crystal by tensile force and noncrystallizable segments. This implies that the connection between two crystal blocks is not rigid. It further suggests that those crystal blocks are the smallest units that bear the tensile force applied to the polymer network. This reconcile the discrepancy that WAXS-derived degree of orientation ($\langle P_2 \rangle$) is higher than that derived from SAXS, since the dislocation of crystal blocks, together with some other effects such as lamellar flipping, decreases the orientation of the lamellae. But crystal blocks can still be well oriented because of the flexible connectivity. An illustration of this pattern is illustrated in **Figure 8-1**.

The stretching-induced fragmentation of lamellar crystal, or intra-lamellar slip, becomes important as temperature lowers. At 100 ^{o}C, a lamella is composed of roughly 5 crystal blocks; while this number decreases to 2 at 60 ^{o}C. At room temperature, the γ-phase is directly destructed into mesomorphic phase. This is because the stress transmitted to the polymer network is higher at lower temperatures, which can be seen from the stress-strain curves.

Shish-like structure is observed in stretching experiments. These shishes are surrounded by lamellae (lamellae are epitaxially grown on the surface). This can be seen from the melting experiment. As the lamellae are melted away, the scattering streaks close to the equator become more distinguishable. This structure is not made of extended chain crystals, as the streaks disappear together with the fading away of the meridian bars in SAXS patterns. Extended chain crystals are thermodynamically stable, and are expected to survive at higher temperatures during

melting. That is to say, the shish-like structure is actually composed of entangled, and extended chain bundles (possibly with small crystals embedded). Its diameter is roughly the same as that of crystal blocks, as estimated from the intensity profile of streaks.

Scattering streaks near the equator are closely coupled with the meridian bars in the SAXS pattern. The apparent two-point SAXS pattern is actually due to the superposition of a four-point pattern. This is not straightforward in stretching experiment, but is supported by the results obtained from melting and recrystallization experiments and also by heating experiment of the sample stretched at a lower temperature. When preexisting oriented texture is melted at lower temperatures, they are partially melted and relaxed. The two-point pattern becomes broader. For the sample stretched at lower temperature, namely, 60 ^{o}C, the two-point pattern will fully relaxed into four-point pattern during heating (see **Figure 6-14**).

In summary, 2D whole-pattern analysis of X-ray scattering data is very useful in understanding the structure development during polymer crystallization, especially for the subject of crystallization induced by external force fields. From the WAXS data, polymorphism and preferred orientation at the length scale of crystal unit cell can be derived; while supramolecular structure at the nanometer length scale can be investigated by SAXS. A combination of these two techniques will help to decipher various aspects in polymer crystallization such as local chain arrangements within a unit cell and the secondary structures composed of crystal blocks.

Random copolymers crystallize differently as compared with their homopolymer counterparts, and the crystallization behavior is dependent on the species of the noncrystallizable comonomer, its content and distribution, in a complex manner. In our study, random copolymers with low content of comonomers are selected as model polymers. Low content of 1-hexene will not change the polymorphism of iPP in its native state, but does have influence on other aspects of crystallization such as kinetics and morphology (chapter 3). Small amount of 1-butene shows more interesting influences. In this case, γ-phase becomes the dominant crystal modification in the native state. A step-shear or a uniaxial stretching is able to introduce interesting polymorphic behavior as well as preferred orientation. 2D whole pattern analysis greatly assists the understanding of structure development in such experiments.

Reference

1. Storks, K. H. *J. Am. Chem. Soc.* **1938,** 60, 1753-1761.

2. Keller, A. *Philos. Mag.* **1957,** 2, (21), 1171-1175.

3. Wittmann, J. C.; Lotz, B. *J. Polym. Sci., Part B: Polym. Phys.* **1985,** 23, (1), 205-226.

4. Cheng, S. Z. D.; Chen, J. H. *J. Polym. Sci., Part B: Polym. Phys.* **1991,** 29, (3), 311-327.

5. Cheng, S. Z. D.; Zhang, A.; Chen, J.; Heberer, D. P. *J. Polym. Sci., Part B: Polym. Phys.* **1991,** 29, (3), 287-297.

6. Flory, P. J.; Yoon, D. Y. *Nature* **1978,** 272, (5650), 226-229.

7. Magill, J. H. *J. Mater. Sci.* **2001,** 36, (13), 3143-3164.

8. Yen, K. C.; Woo, E. M.; Tashiro, K. *Polymer* **2010,** 51, (23), 5592-5603.

9. Hoffman, J. D.; Davis, G. T.; Laurizten, J. I., In *Treatise on solid state chemistry, Crystalline and non-crystalline solids*, Hannay, N. B., Ed. Plenum: New York, 1976; Vol. 3.

10. Lotz, B. *J. Macromol. Sci., Phys.* **2002,** B41, (4-6), 685-709.

11. Khoury, F. *J. res. Nat. Bur. Stand. Sect. A: Phys. chem.* **1966,** A 70, (1), 29-61.

12. Padden, F. J.; Keith, H. D. *J. Appl. Phys.* **1959,** 30, (10), 1479-1484.

13. Padden, F. J.; Keith, H. D. *J. Appl. Phys.* **1966,** 37, (11), 4013-4020.

14. Magill, J. H. *J. Polym. Sci., Part A2: Polym. Phys.* **1969,** 7, (1PA2), 123-142.

15. Samuels, R. J. *J. Polym. Sci., Part A2: Polym. Phys.* **1971,** 9, (12), 2165-2246.

16. Keum, J. K.; Burger, C.; Zuo, F.; Hsiao, B. S. *Polymer* **2007,** 48, 4511-4519.

17. Clough, S.; Vanaarts.J; Stein, R. S. *J. Appl. Phys.* **1965,** 36, (10), 3072-3085.

18. Clough, S. B.; Stein, R. S. *J. Appl. Phys.* **1967,** 38, (11), 4446-4450.

19. Pennings, A. J.; Vanderma.Jm; Booij, H. C. *Kolloid-Zeitschrift and Zeitschrift Fur Polymere* **1970,** 236, (2), 99-111.

20. Pennings, A. J.; Vanderma.Jm; Kiel, A. M. *Kolloid-Zeitschrift and Zeitschrift Fur Polymere* **1970,** 237, (2), 336-358.

21. Kalay, G.; Kalay, C. R. *J. Polym. Sci., Part B: Polym. Phys.* **2002,** 40, (17), 1828-1834.

22. Hsiao, B. S.; Yang, L.; Somani, R. H.; Avila-Orta, C. A.; Zhu, L. *Phys. Rev. Lett.* **2005,** 94, (11), 117802-1-4.

23. Binsbergen, F. L. *Nature* **1966,** 211, (5048), 516-517.

24. Varga, J. *J. Mater. Sci.* **1992,** 27, (10), 2557-2579.

25. Varga, J.; KargerKocsis, J. *J. Polym. Sci., Part B: Polym. Phys.* **1996,** 34, (4), 657-670.

26. Li, Z. M.; Li, L. B.; Shen, K. Z.; Yang, W.; Huang, R.; Yang, M. B. *Macromol. Rapid Commun.* **2004,** 25, (4), 553-558.

27. Zhang, S.; Minus, M. L.; Zhu, L. B.; Wong, C. P.; Kumar, S. *Polymer* **2008,** 49, (5), 1356-1364.

28. Na, B.; Guo, M.; Yang, J. H.; Tan, H.; Zhang, Q.; Fu, Q. *Polym. Int.* **2006,** 55, (4), 441-448.

29. Assouline, E.; Fulchiron, R.; Gerard, J. F.; Wachtel, E.; Wagner, H. D.; Marom, G. *J. Polym. Sci., Part B: Polym. Phys.* **1999,** 37, (17), 2534-2538.

30. Assouline, E.; Wachtel, E.; Grigull, S.; Lustiger, A.; Wagner, H. D.; Marom, G. *Macromolecules* **2002,** 35, (2), 403-409.

31. Assouline, E.; Grigull, S.; Marom, G.; Wachtel, E.; Wagner, H. D. *J. Polym. Sci., Part B: Polym. Phys.* **2001,** 39, (17), 2016-2021.

32. Quan, H.; Li, Z. M.; Yang, M. B.; Huang, R. *Compos. Sci. Technol.* **2005,** 65, (7-8), 999-1021.

33. Stern, T.; Wachtel, E.; Marom, G. *J. Polym. Sci., Part B: Polym. Phys.* **1997,** 35, (15), 2429-2433.

34. Assouline, E.; Pohl, S.; Fulchiron, R.; Gerard, J. F.; Lustiger, A.; Wagner, H. D.; Marom, G. *Polymer* **2000,** 41, (21), 7843-7854.

35. Porter, D. A.; Easterling, K. E., *Phase transformations in metals and alloys*. Nelson Thornes: 1992.

36. Muthukumar, M. *Advances in Chemical Physics, Vol 128* **2004,** 128, 1-63.

37. Wunderlich, B., *Macromolecular Physics: Crystal nucleation, growth, annealing*. Academic Press: 1976.

38. Sperling, L. H., *Introduction to physical polymer science*. Wiley-Interscience: 2006.

39. Okui, N.; Umemoto, S.; Kawano, R.; Mamun, A., Temperature and Molecular Weight Dependencies of Polymer Crystallization. In *Progress in Understanding of Polymer Crystallization*, Reiter, G.; Strobl, G., Eds. Springer Berlin / Heidelberg: 2007; Vol. 714, pp 391-425.

40. Hoffman, J. D. *Polymer* **1982,** 23, (5), 656-670.

41. Hoffman, J. D. *Polymer* **1983,** 24, 3-26.

42. Hoffman, J. D.; Miller, R. L. *Macromolecules* **1988,** 21, (10), 3038-3051.

43. de Gennes, P. G. *Macromolecular Symposia* **2003,** 191, 7-9.

44. Fredrickson, G. H.; Milner, S. T.; Leibler, L. *Macromolecules* **1992,** 25, (23), 6341-6354.

45. Semenov, A. N. *Physical Review E* **2006,** 73, (4), 041803-1-19.

46. Semenov, A. N. *European Physical Journal B* **1999,** 10, (3), 497-507.

47. Dobrynin, A. V. *The Journal of Chemical Physics* **1997,** 107, (21), 9234-9238.

48. Nesarikar, A.; Delacruz, M. O.; Crist, B. *J. Chem. Phys.* **1993,** 98, (9), 7385-7397.

49. Flory, P. J. *Transactions of the Faraday Society* **1955,** 51, (6), 848-857.

50. Crist, B.; Finerman, T. M. *Polymer* **2005,** 46, (20), 8745-8751.

51. Crist, B. *Polymer* **2003,** 44, (16), 4563-4572.

52. Crist, B.; Howard, P. R. *Macromolecules* **1999,** 32, (9), 3057-3067.

53. Crist, B.; Mirabella, F. M. *J. Polym. Sci., Part B: Polym. Phys.* **1999,** 37, (21), 3131-3140.

54. De Rosa, C.; Auriemma, F.; de Ballesteros, O. R.; Resconi, L.; Camurati, I. *Macromolecules* **2007,** 40, (18), 6600-6616.

55. Jeon, K.; Palza, H.; Quijada, R.; Alamo, R. G. *Polymer* **2009,** 50, (3), 832-844.

56. Hosier, I. L.; Alamo, R. G.; Esteso, P.; Isasi, J. R.; Mandelkern, L. *Macromolecules* **2003,** 36, (15), 5623-5636.

57. Hosoda, S.; Hori, H.; Yada, K.-i.; Nakahara, S.-y.; Tsuji, M. *Polymer* **2002,** 43, (26), 7451-7460.

58. De Rosa, C.; Dello Iacono, S.; Auriemma, F.; Ciaccia, E.; Resconi, L. *Macromolecules* **2006,** 39, (18), 6098-6109.

59. De Rosa, C.; Auriemma, F.; Vollaro, P.; Resconi, L.; Guidotti, S.; Camurati, I. *Macromolecules* **2011,** 44, (3), 540-549.

60. Lipson, A.; Lipson, S. G.; Lipson, H., *Optical Physics*. Cambridge University Press: 2010.

61. Born, M.; Wolf, E.; Bhatia, A. B.; Clemmow, P. C.; Gabor, D.; Stokes, A. R.; Taylor, A. M.; Wayman, P. A.; Wilcock, W. L., *Principles of Optics: Electromagnetic Theory of Propagation, Interference and Diffraction of Light*. Cambridge University Press: 2000.

62. Milonni, P. W.; Eberly, J. H., *Laser Physics*. John Wiley & Sons: 2009.

63. Guinier, A., *X-ray diffraction in crystals, imperfect crystals, and amorphous bodies*. Dover: 1994.

64. Alexander, L. E., *X-ray diffraction methods in polymer science*. Krieger: 1979.

65. Stribeck, N. *Acta Crystallographica Section A* **2009,** 65, 46-47.

66. Stribeck, N.; Nochel, U. *Journal of Applied Crystallography* **2009,** 42, 295-301.

67. Bracewell, R. N., *The Fourier transform and its applications*. McGraw Hill: 2000.

68. Glatter, O.; Kratky, O., *Small angle x-ray scattering*. Academic Press: 1982.

69. Guinier, A.; Fournet, G., *Small-angle scattering of X-rays*. Wiley: 1955.

70. Arfken, G. B.; Weber, H. J., *Mathematical methods for physicists*. Elsevier: 2005.

71. Ruland, W.; Tompa, H. *Acta Crystallographica Section a-Crystal Physics Diffraction Theoretical and General Crystallography* **1968,** A 24, 93-99.

72. Ruland, W. *Colloid and Polymer Science* **1977,** 255, (9), 833-836.

73. Burger, C.; Hsiao, B. S.; Chu, B. *Polymer Reviews* **2010,** 50, (1), 91-111.

74. Doyle, P. A.; Turner, P. S. *Acta Crystallographica Section a-Crystal Physics Diffraction Theoretical and General Crystallography* **1968,** A 24, 390-397.

75. Burger, C.; Zhou, H. W.; Sics, I.; Hsiao, B. S.; Chu, B.; Graham, L.; Glimcher, M. J. *Journal of Applied Crystallography* **2008,** 41, 252-261.

76. Mao, Y. M.; Burger, C.; Zuo, F.; Hsiao, B. S.; Mehta, A.; Mitchell, C.; Tsou, A. H. *Macromolecules* **2011,** 44, (3), 558-565.

77. Hosemann, R.; Bagchi, S. N., *Direct analysis of diffraction by matter*. North-Holland Pub. Co.: 1962.

78. Ruland, W.; Smarsly, B. *Journal of Applied Crystallography* **2004,** 37, 575-584.

79. Burger, C.; Zhou, H. W.; Wang, H.; Sics, I.; Hsiao, B. S.; Chu, B.; Graham, L.; Glimcher, M. J. *Biophysical Journal* **2008,** 95, (4), 1985-1992.

80. Guentert, O. J.; Cvikevich, S. *Carbon* **1964,** 1, (3), 309-313.

81. Somani, R. H.; Hsiao, B. S.; Nogales, A.; Srinivas, S.; Tsou, A. H.; Sics, I.; Balta-Calleja, F. J.; Ezquerra, T. A. *Macromolecules* **2000,** 33, (25), 9385-9394.

82. Natta, G.; Corradini, P. *Nuovo Cimento Suppl.* **1960,** 15, (40), 40-51.

83. Bruckner, S.; Meille, S. V. *Nature* **1989,** 340, (6233), 455-457.

84. Meille, S. V.; Bruckner, S.; Porzio, W. *Macromolecules* **1990,** 23, (18), 4114-4121.

85. Meille, S. V.; Ferro, D. R.; Bruckner, S.; Lovinger, A. J.; Padden, F. J. *Macromolecules* **1994,** 27, (9), 2615-2622.

86. Lotz, B.; Kopp, S.; Dorset, D. *Comptes Rendus De L Academie Des Sciences Serie Ii* **1994,** 319, (2), 187-192.

87. Ferro, D. R.; Meille, S. V.; Bruckner, S. *Macromolecules* **1998,** 31, (20), 6926-6934.

88. Natta, G. *Makromolekulare Chemie* **1960,** 35, 94-131.

89. Mandelkern, L., *Crystallization of Polymers: Kinetics and mechanisms*. Cambridge University Press: 2004.

90. Wang, Z. G.; Hsiao, B. S.; Sirota, E. B.; Agarwal, P.; Srinivas, S. *Macromolecules* **2000,** 33, (3), 978-989.

91. Okada, T.; Saito, H.; Inoue, T. *Macromolecules* **1992,** 25, (7), 1908-1911.

92. Pogodina, N. V.; Siddiquee, S. K.; van Egmond, J. W.; Winter, H. H. *Macromolecules* **1999,** 32, (4), 1167-1174.

93. Iijima, M.; Strobl, G. *Macromolecules* **2000,** 33, (14), 5204-5214.

94. Sung, B. J.; Yethiraj, A. *Journal of Chemical Physics* **2005,** 122, (23), 234904-1-9.

95. Houdayer, J.; Muller, M. *Europhysics Letters* **2002,** 58, (5), 660-665.

96. Hu, W. B.; Mathot, V. B. F.; Frenkel, D. *Macromolecules* **2003,** 36, (6), 2165-2175.

97. Houdayer, J.; Muller, M. *Macromolecules* **2004,** 37, (11), 4283-4295.

98. Velankar, S.; Cooper, S. L. *Macromolecules* **2000,** 33, (2), 382-394.

99. Wignall, G. D.; Alamo, R. G.; Ritchson, E. J.; Mandelkern, L.; Schwahn, D. *Macromolecules* **2001,** 34, (23), 8160-8165.

100. Cahn, J. W. *Transactions of the Metallurgical Society of Aime* **1968,** 242, (2), 166-180.

101. Hashimoto, T.; Kumaki, J.; Kawai, H. *Macromolecules* **1983,** 16, (4), 641-648.

102. He, M. J.; Liu, Y. M.; Yi, F.; Ming, J.; Han, C. C. *Macromolecules* **1991,** 24, (2), 464-473.

103. Hashimoto, T.; Itakura, M.; Hasegawa, H. *Journal of Chemical Physics* **1986,** 85, (10), 6118-6128.

104. Li, Y.; Akpalu, Y. A. *Macromolecules* **2004,** 37, (19), 7265-7277.

105. Massa, W., *Crystal structure determination*. Springer: 2004.

106. Kumaraswamy, G.; Issaian, A. M.; Kornfield, J. A. *Macromolecules* **1999,** 32, (22), 7537-7547.

107. Kalay, G.; Bevis, M. J. *Journal of Polymer Science Part B-Polymer Physics* **1997,** 35, (2), 241-263.

108. Auriemma, F.; De Rosa, C.; Boscato, T.; Corradini, P. *Macromolecules* **2001,** 34, (14), 4815-4826.

109. Bird, R. B.; Hassager, O., *Dynamics of Polymeric Liquids: Fluid mechanics*. Wiley: 1987.

110. Garcia-Gutierrez, M. C.; Hernandez, J. J.; Nogales, A.; Pantine, P.; Rueda, D. R.; Ezquerra, T. A. *Macromolecules* **2008,** 41, (3), 844-851.

111. Hernandez, J. J.; Garcia-Gutierrez, M. C.; Nogales, A.; Rueda, D. R.; Ezquerra, T. A. *Macromolecules* **2009,** 42, (13), 4374-4376.

112. Doi, M.; Edwards, S. F., *The theory of polymer dynamics*. Clarendon Press: 1986.

113. Kumaraswamy, G.; Verma, R. K.; Kornfield, J. A.; Yeh, F. J.; Hsiao, B. S. *Macromolecules* **2004,** 37, (24), 9005-9017.

114. Balzano, L. G.; Rastogi, S.; Peters, G. W. M. *Macromolecules* **2009,** 42, (6), 2088-2092.

115. Somani, R. H.; Yang, L.; Hsiao, B. S.; Agarwal, P. K.; Fruitwala, H. A.; Tsou, A. H. *Macromolecules* **2002,** 35, (24), 9096-9104.

116. Somani, R. H.; Yang, L.; Hsiao, B. S.; Fruitwala, H. *J. Macromol. Sci., Phys.* **2003,** B42, (3-4), 515-531.

117. Kumaraswamy, G.; Kornfield, J. A.; Yeh, F. J.; Hsiao, B. S. *Macromolecules* **2002,** 35, (5), 1762-1769.

118. Liedauer, S.; Eder, G.; Janeschitzkriegl, H. *Int. Polym. Proc.* **1995,** 10, (3), 243-250.

119. Kumaraswamy, G.; Verma, R. K.; Issaian, A. M.; Wang, P.; Kornfield, J. A.; Yeh, F.; Hsiao, B. S.; Olley, R. H. *Polymer* **2000,** 41, (25), 8931-8940.

120. Janeschitz-Kriegl, H. *Colloid. Polym. Sci.* **2003,** 281, (12), 1157-1171.

121. Hugel, T.; Strobl, G.; Thomann, R. *Acta Polym.* **1999,** 50, (5-6), 214-217.

122. Strobl, G. *European Physical Journal E* **2000,** 3, (2), 165-183.

123. Hong, K.; Rastogi, A.; Strobl, G. *Macromolecules* **2004,** 37, (26), 10174-10179.

124. Gsell, C.; Hiver, J. M.; Dahoun, A.; Souahi, A. *J. Mater. Sci.* **1992,** 27, (18), 5031-5039.

125. Fang, F.; Zhang, M. Z.; Huang, J. F. *J. Polym. Sci., Part B: Polym. Phys.* **2005,** 43, (22), 3255-3260.

126. Koike, Y.; Cakmak, M. *J. Polym. Sci., Part B: Polym. Phys.* **2004,** 42, (12), 2228-2237.

127. Guinier, A., *X-Ray Diffraction: In Crystals, Imperfect Crystals, and Amorphous Bodies*. Dover Publications: 1994.

128. Al-Hussein, M.; Strobl, G. *Macromolecules* **2002,** 35, (22), 8515-8520.

129. Hiss, R.; Hobeika, S.; Lynn, C.; Strobl, G. *Macromolecules* **1999,** 32, (13), 4390-4403.

130. Reck, E. M.; Schenk, H.; Wilke, W. *Progress in Colloid and Polymer Science* **1985,** 71, 154-163.

131. Heck, B.; Hugel, T.; Iijima, M.; Strobl, G. *Polymer* **2000,** 41, (25), 8839-8848.

132. GaucherMiri, V.; Seguela, R. *Macromolecules* **1997,** 30, (4), 1158-1167.

133. Young, R. J.; Bowden, P. B.; Ritchie, J. M.; Rider, J. G. *J. Mater. Sci.* **1973,** 8, (1), 23-36.

134. Hong, K.; Rastogi, A.; Strobl, G. *Macromolecules* **2004,** 37, (26), 10165-10173.

135. Haward, R. N.; Thackray, G. *Proceedings of the Royal Society of London Series a-Mathematical and Physical Sciences* **1968,** 302, (1471), 453-472.

136. Glatter, O., *Small Angle X-Ray Scattering*. Academic Press: 1982; p 525.

137. Bracewell, R., *The Fourier Transform and Its Applications* 3rd ed.; McGraw-Hill: 1999.

138. Murthy, N. S.; Minor, H.; Bednarczyk, C.; Krimm, S. *Macromolecules* **1993,** 26, (7), 1712-1721.

139. Rosenfeld, Y. *Physical Review A* **1990,** 42, (10), 5978-5989.

140. Thomann, R.; Wang, C.; Kressler, J.; Mulhaupt, R. *Macromolecules* **1996,** 29, (26), 8425-8434.

141. Alamo, R. G.; Kim, M. H.; Galante, M. J.; Isasi, J. R.; Mandelkern, L. *Macromolecules* **1999,** 32, (12), 4050-4064.

142. Wiyatno, W.; Pople, J. A.; Gast, A. P.; Waymouth, R. M.; Fuller, G. G. *Macromolecules* **2002,** 35, (22), 8488-8497.

143. Wiyatno, W.; Fuller, G. G.; Pople, J. A.; Gast, A. P.; Chen, Z. R.; Waymouth, R. M.; Myers, C. L. *Macromolecules* **2003,** 36, (4), 1178-1187.

144. Auriemma, F.; De Rosa, C. *Macromolecules* **2002,** 35, (24), 9057-9068.

145. Auriemma, F.; De Rosa, C. *Macromolecules* **2006,** 39, (22), 7635-7647.

146. Eder, G.; Janeschitzkriegl, H.; Liedauer, S. *Prog. Polym. Sci.* **1990,** 15, (4), 629-714.

147. Janeschitz-Kriegl, H.; Eder, G. *Journal of Macromolecular Science Part B-Physics* **2007,** 46, (3), 591-601.

148. Corradini, P.; Petraccone, V.; Derosa, C.; Guerra, G. *Macromolecules* **1986,** 19, (11), 2699-2703.

149. Androsch, R.; Di Lorenzo, M. L.; Schick, C.; Wunderlich, B. *Polymer* **2010,** 51, (21), 4639-4662.

150. Gailey, J. A.; Ralston, R. H. *Spe Transactions* **1964,** 4, (1), 29-33.

151. Cohen, Y.; Saraf, R. F. *Polymer* **2001,** 42, (13), 5865-5870.

152. Mao, Y. M.; Burger, C.; Li, X. W.; Hsiao, B. S.; Mehta, A.; Mitchell, C.; Tsou, A. H. *Macromolecules* **2011,** 44, 558-565.

153. Zuo, F.; Keum, J. K.; Chen, X. M.; Hsiao, B. S.; Chen, H. Y.; Lai, S. Y.; Wevers, R.; Li, J. *Polymer* **2007,** 48, 6867-6880.

154. Lin, L.; Argon, A. S. *Journal of Materials Science* **1994,** 29, (2), 294-323.

155. Dias, P.; Kazmierczak, T.; Chang, A.; Ansems, P.; Van Dun, J.; Hiltner, A.; Baer, E. *Journal of Applied Polymer Science* **2009,** 112, (6), 3736-3747.

156. Peterlin, A. *Journal of Materials Science* **1971,** 6, (6), 490-508.

157. Koike, Y.; Cakmak, M. *Macromolecules* **2004,** 37, (6), 2171-2181.

158. Brandrup, J.; Immergut, E. H.; Grulke, E. A., *Polymer handbook*. Wiley: 1999.